Rational Synthesis of Monodisperse Nanoparticles for Catalytic Applications

By

Huiyuan Zhu

B.Sc., University of Science and Technology of China, 2009

M.A., Brown University, 2012

A Dissertation Submitted in Partial Fulfillment of the

Requirements for the Degree of Doctor of Philosophy

in the Department of Chemistry at Brown University

Providence, Rhode Island

May 2015

This dissertation by Huiyuan Zhu is accepted in its present form

by the Department of Chemistry as satisfying the dissertation requirement

for the degree of Doctor of Philosophy.

Date _____ _____

Shouheng Sun, Advisor

Recommended to the Graduate Council by

Date _____ _____

Eunsuk Kim, Reader

Date _____ _____

Lai-Sheng Wang, Reader

Approved by the Graduate Council

Date _____ _____

Peter Weber, Dean of the Graduate School

Curriculum Vita

Huiyuan Zhu was born on January 24, 1987, in Quanjiao, Anhui, China. She attended University of Science and Technology of China (Hefei, China) from 2005 to 2009, graduating with her B.Sc. in Chemistry. In 2010, she was accepted with a fellowship in the graduate program of the Department of Chemistry at Brown University to pursue the degree of Doctor of Philosophy in Chemistry. During this period, she held positions as research and teaching assistants. Since January 2011, she has been focused on the rational synthesis of monodisperse nanoparticles for catalytic applications under the supervision of Professor Shouheng Sun. She has 12 papers published in peer-reviewed journals, 1 book chapter, 1 patent in pending and another 2 papers under review or in preparation. During her study at Brown, she won multiple awards, including International Precious Metal Institute Gemini Graudate Student Award and Chinese Government Award for Outstanding Self-Financed Students Abroad (2013). In August 2014, she was selected as one of the first class Liane Russell Fellows in Oak Ridge National Laboratory.

Publications

15. Guangming Jiang[+], **Huiyuan Zhu**[+] ([+]equal contribution), Bo Shen and Shouheng Sun, "Face-centered Tetragonal FePd Nanoparticles: A New Class of Non-Pt Catalysts for Oxygen Reduction Reaction". *In preparation.*

14. Adriana Mendoza-Garcia, **Huiyuan Zhu**, Yongsheng Yu, Qing Li, Lin Zhou, Jing Li, Dong Su, Matthew J. Kramer and Shouheng Sun, "Sea Urchin-like Cobalt-Iron Phosphide Nanostructures as an Efficient Catalyst for the Oxygen Evolution Reaction", *J. Am. Chem. Soc. Submitted*.

13. **Huiyuan Zhu**, Sen Zhang, Dong Su, Guangming Jiang and Shouheng Sun, "Surface Profile Control of FeNiPt/Pt Core/Shell Nanowires for Oxygen Reduction Reaction", *SMALL* **2015**, DOI: 10.1002/smll.201500330.

12. Qing Li, Liheng Wu, Gang Wu, Dong Su, Haifeng Lv, Sen Zhang, Wenlei Zhu, Anix Casimir, **Huiyuan Zhu**, Adriana Mendoza-Garcia and Shouheng Sun, "A New Approach to Fully-Ordered fct-FePt Nanoparticles for Much Enhanced Electrocatalysis in Acid", *Nano Lett.* **2015**, DOI: 10.1021/acs.nanolett.5b00320.11.

11. Hanfeng Lu, Pengfei Zhang, Zhen-an Qiao, Jinshui Zhang, Jihua Chen, **Huiyuan Zhu** and Sheng Dai, "Ionic liquid–mediated synthesis of meso-scale porous lanthanum-transition- metal perovskites with high CO oxidation performance", *Chem. Commun*. **2015**, DOI: 10.1039/C5CC00534E.

10. **Huiyuan Zhu**, Aruna Sigdel, Sen Zhang, Dong Su, Zheng Xi, Qing Li, Shouheng Sun, "Core/Shell Au/MnO Nanoparticles Prepared from Controlled Oxidation of AuMn as a New Form of Electrocatalyst for Sensitive H2O2 Detection", *Angew. Chem. Int. Ed.* **2014**, *53*, 12508-12512. (VIP Article)

9. Liheng Wu, Pierre-Olivier Jubert, David Berman, Wayne Imaino, Alshakim Nelson, **Huiyuan Zhu**, Sen Zhang, and Shouheng Sun, "Monolayer Assembly of Ferrimagnetic $Co_xFe_xO_4$ Nanocubes to Support Magnetization Transitions", *Nano Lett.* **2014**, *14*, 3395-3399.

8. Sen Zhang, Xu Zhang, Guangming Jiang, **Huiyuan Zhu**, Shaojun Guo, Dong Su, Gang Lu and Shouheng Sun, "Tuning Nanoparticle Structure and Surface Strain for Catalysis Optimization", *J. Am. Chem. Soc*. **2014**, *136*, 7734-7739.

7. Sen Zhang, Guangming Jiang, Gabriel T. Filsinger, Liheng Wu, **Huiyuan Zhu**, Jonghun Lee, Zhongbiao Wu, Shouheng Sun, "Halide Ion-Mediated Growth of Single Crystalline Fe Nanoparticles", *Nanoscale* **2014**, *6*, 4852-4856.

6. **Huiyuan Zhu**, Yu-Xi Huang, Sen Zhang, Shouheng Sun, "Tailoring Nanoparticle Electrocatalysts for Proton Exchange Membrane Fuel Cells", *Catalysis by Materials with Well-defined Structures*, ed. Zili Wu, Steve Overbury, Elsevier, **2014**.

5. **Huiyuan Zhu**, Sen Zhang, Yu-Xi Huang, Liheng Wu, Shouheng Sun, "Monodisperse $M_xFe_{3-x}O_4$ (M=Fe, Cu, Co, Mn) Nanoparticles and Their

Electrocatalysis for Oxygen Reduction Reaction", *Nano Lett*. **2013**, *13*, 2947-2951.

4. **Huiyuan Zhu**, Sen Zhang, Shaojun Guo, Dong Su, Shouheng Sun, "Synthetic Control of FePtM Nanorods (M=Cu, Ni) to Enhance the Oxygen Reduction Reaction", *J. Am. Chem. Soc*. **2013**, *135*, 7130-7133.
3. Shaojun Guo, Dongguo Li, **Huiyuan Zhu**, Sen Zhang, Nenad M. Markovic, Vojislav R. Stamenkovic*, Shouheng Sun,"FePt and CoPt Nanowires as Efficient Catalysts for Oxygen Reduction Reaction", *Angew. Chem. Int. Ed*. **2013**, *52*, 3465-3468. (VIP Article)
2. Sen Zhang, Shaojun Guo, **Huiyuan Zhu**, Dong Su, Shouheng Sun, "Structure-Induced Enhancement in Electrooxidation of Trimetallic FePtAu Nanoparticles", *J. Am. Soc. Chem.* **2012**, *134*, 5060-5063. (Highlighted in C&EN news and Brown University Media Relations)
1. Sen Zhang, **Huiyuan Zhu**, Zhi-Bin Hu, Lu Liu, Shaofeng Chen, Shu-Hong Yu, "Magnetite-Nanoparticles-Attached Necklace-like Cu@Cross-Linked Poly(vinyl alcohol) Microcables: Synthesis, Individual Magnetic Manipulation and Fluorescent Property", *Chem. Commun*. **2009**, 2326-2328.

Acknowledgements

I never knew one day I would become a doctor of philosophy. I never knew I would take chemistry as my career. It just happened, naturally. I still remember back to the winter of 2009, I was stucked in the dilemma: to transfer to Brown or stay in Stony Brook University. I could stay in SBU, try to get a Master degree out of Chemistry and get a non-research job either in US or in China. Or I could go to Brown and stay in the chemistry PhD program. I chose the latter, not only because my boyfriend was at Brown at that time, but also, deep in my heart, I still have some fantasy in science. This might date back to my childhood. At that time, I was curious about the universe and obsessed with science fiction, such as Hitchikker's Guide to Galaxy. I would say thanks to Douglas Adams and my boyfriend. Without them, I would never make this choice which turned out to be one of the best decisions in my life.

The day I met Prof. Shouheng Sun is a warm day in Sept. 2010, just as warm as today when I'm writing down those words. Ever since then, I feel fortunate and honored to have him not only as my research advisor but also the lifetime-long mentor. If I said the curiocity led me to the science field, he guided me through the research path. During the past four years, he has always been supportive and inspiring. His attitude in the way of doing research, his philosophy of logic thinking and his enthusiasm in science make him the perfect model for me to learn from. He has always been patient, understanding and encouraging when I am experiencing

difficulties during my research and my life, just like a father and a friend. I would express my deepest and endless thanks to him. He is the best mentor I could ever imagine.

I am also grateful to have so many great professors here at Brown. Prof. Eunsuk Kim and Prof. Lai-Sheng Wang, they have shared their valuable time on my RPD, ORP and defense and have always been helpful to give me valuble suggestions and discussions. I would specially thank Prof. Eunsuk Kim for her kind support and useful suggestion during my job search. Thanks go to Prof. Matthew Zimmt, for his encouragement during my research life at Brown. I appreciate Prof. Paul Williard, Prof. Dwight Sweigart and Prof. Chi-Wang Shu (Applied Math. Dept.) for their exellent teaching for me to build up foundations for chemistry and mathematics.

I feel fortunate to have the greatest collaborators and group members to work with. Without their help, I couldn't accomplish my research. Thank Dr. Dong Su at Brookhaven National Laboratory for his great work on STEM analysis of my samples. My appreciations extend to Dr. Anthony McCormick in the Department of Engineering at Brown for the help on HRTEM operation and Dr. Joseph Orchardo in the Department of Geological Science at Brown for the help with ICP measurement. Thanks go to my wonderful group members. Dr. Shaojun Guo and Dr. Qing Li helped me a lot in electrochemistry. Dr. Sally Ho taught me about nanoparticle synthesis. A special acknowledgement goes to Adriana Mendoza-Garcia, Aruna Sigdel, Liheng Wu and Guangming Jiang for their assistance in experiment and a lot

of precious time we had together. Thank Dr. Dongguo Li for the collaboration and the help in electrochemistry. I would like to thank Dr. Jonghun Lee, Dr. Don Ho, Bo Ning, Hongyi Zhang, Yu-Xi Huang, Wenlei Zhu, Sheng Liu, Xi Zheng, Bo Shen, Caoyuan Ma, Haifeng Lv and Christopher Wright and Gabriel Filsinger, and all other Sun group members. Thank you for your help in research and all the enjoyable time in life.

Words can not express my thanks to my dear friends both here at Brown and elsewhere all over the world. Especially, Yuanyuan Zhang, Jin Dong, Xiaoshu Lv, Xinjun Guo, Yinsui Zheng, Hongwei Xu, we had great time together here at Brown. Thank you for always being with me in the past four years.

Finally, I would thank my parents and my husband for their endless love and support in my life voyage. They are always there for me no matter ups and downs. Especially, Sen, we have been together for almost ten years, just like we grew up together. We explore the world and life together. I cherish every moment we spent and I feel blessed to have you as my other half. Without you and my parents, I could be a complete different person and I would never achieve this.

To my family

Abstract of “Rational Synthesis of Monodisperse Nanoparticles for Catalytic Applications” by HUIYUAN ZHU, Ph. D., Brown University, July 2014.

Controlled synthesis of nanoparticles (NPs) is the key to developing highly efficient and stable catalysts for various reactions, including those involved in energy conversion systems, such as the proton exchange membrane fuel cell, and those used for catalytic bio-detections. The organic-solution based chemical synthesis provides a robust approach to obtaining well-defined NPs with monodisperse morphologies and assuring precise control over NP physicochemical parameters (size, shape, composition and crystal structure). It thus allows for a better understanding of the parameter-property correlation and the optimization rules of advanced NP catalysts. This dissertation covers the synthesis of 1-dimensional (1-D) binary FePt, CoPt and ternary FePtCu, FePtNi nanowires (NWs), face centered tetragonal (fct) FePt nanoparticles (NPs), Au-MnO nanocomposites and *etc.*, as well as their applications in energy conversion and bio-detection systems.

One-dimensional FePt, CoPt and FePtM (M = Cu, Ni) nanowires (NWs) are synthesized and converted to FePtM/Pt core/shell structure. These FePtM/Pt NWs show superior performance in catalyzing oxygen reduction reaction (ORR) in acidic solution. Furthermore, seed-mediated approach is applied to produce FeNiPt/Pt core/shell NWs. Tailoring the NW thickness and the surface structure (Pt-skeleton and Pt-skin) leads to an optimized catalytic performance towards ORR.

Monodisperse FePt NPs are synthetically controlled from chemically disordered face centered cubic (fcc) structure to ordered face centered tetragonal (fct) structure. The NP's electrocatalytic efficiency in oxygen reduction reaction (ORR) can be drastically increased by the fcc-fct structural transition. The relevant theoretical calculations of the structure-induced catalytic enhancement will also be discussed to provide a predictable model for future design and optimization of ORR nanocatalysts.

My thesis also includes some other NPs, such as Au-MnO nanocomposites used for the electrochemical detection of H_2O_2, sub-10 nm M (II)-substituted magnetite $M_xFe_{3-x}O_4$ (M=Fe, Cu, Co, Mn) NPs as the alternatives for Pt to catalyze ORR in alkaline solution and structure-controlled NPs FePtAu as electrocatalysts for formic acid oxidation reaction (FAOR).

Table of Contents

List of Figures and Tables

Figure 9.3 CVs of the *fct*-$Fe_{43}Pt_{37}Au_{20}$, *fcc*-$Fe_{43}Pt_{37}Au_{20}$, *fct*-$Fe_{55}Pt_{45}$ and commercial Pt NPs in the N_2-saturated 0.5 M H_2SO_4 and 0.5 M methanol solution. In the methanol oxidation reaction, two oxidation peaks are usually observed. The stronger peak in the forward scan is related to the direct methanol oxidation. The smaller peak in the backward scan is likely associated the oxidation of the carbonaceous species formed on the catalyst surface in the forward scan. The ratio of the forward peak current (I_f) to the backward peak current (I_b), I_f/I_b, is often used as an index to measure the catalyst tolerance to the poisoning species (like CO). A higher ratio indicates more effective removal of the poisoning species on the catalyst surface. The CV from the *fct*-$Fe_{43}Pt_{37}Au_{20}$ NPs has an I_f/I_b value of 2.8, while for the *fcc*-$Fe_{43}Pt_{37}Au_{20}$, *fct*-$Fe_{55}Pt_{45}$ and commercial Pt NP catalysts, the values drop to 1.62, 1.20, and 0.71 respectively. 185

Chapter 1

Introduction to Nanoparticles: Synthesis and Catalytic Applications

1.1 General Introduction to Nanoparticles

The prefix "nano" means one billionth (10^{-9}) in the International System of Units, so one nanometer (nm) is a billionth of a meter. Nanomaterials are usually referred to a class of materials with at least one dimension between 1 – 100 nm. Due to the structure confinement, their physical and chemical properties can be dramatically changed from their bulk counterparts. According to the degree of confinement in the structure, nanomaterials are categorized into zero-dimensional (0-D) (nanoparticles), one-dimensional (1-D) (nanowires and nanorods) and two-dimensional (2-D) (nanoplates). The interest and importance of nanomaterial was emerged from the visionary lecture of "*There's Plenty of Room at the Bottom*" given by Richard Feynman at the American Physical Society meeting at 1959.[1] Since then, increasing research efforts have been put in the field of nanomaterials, where unique properties enable novel applications.

Nanomaterials present unique properties dramatically distinct from their bulky counterparts.[2-3] The most popular example is the fluorescent emission of semiconductor nanoparticles.[4-5] When semiconductor materials (CdSe, GaN,*et al.*) go down to nanoscale, the spatial confinement of electrons is comparable to the length scale of nucleus restriction for electrons (Bohr radius, typically a few nanometers). The electronic structure is changed from the continuous energy bands to discrete and quantized electronic levels, and thus called quantum dot (QD). The fluorescence is originated from the absorption and emission of photons and the electron excitation

and transition among the quantized energy levels. Moreover, the fluorescent emission can be readily controlled to cover the entire visible range by varying the QD's physical size.[5]

Another typical example is the localized surface plasma resonance (SPR) displayed in some noble metallic nanoparticles (NPs) (Ag, Au, Cu etc.).[6-8] For instance, the color of Au NPs are not yellow as bulk gold; instead, they appear to be red. This is because the collective oscillation of electrons in the conduction band of Au NPs can be driven by the visible light. Furthermore, the SPR peak disappears when Au NPs' size is less than 2 nm due to quantum size effects and absence of collective oscillation.

Owing to these unique properties, NPs can be rational controlled to be applied in a wide range of fields, including optical devices, biomedical applications, magnetic devices and catalysis.[9-13] For example, QDs' size-tuned emission, broad excitation spectra and high resistance to degradation, [14-15] make them suitable for optoelectronics and biological probes. The SPR of Au has been used in biosensing and imaging.[16-17]

1.2 Synthesis of Monodisperse Nanoparticles

Due to the appealing properties of nanomaterials introduced above, to obtain nanomaterials in desired physical and chemical parameters with uniformity in size, shape, composition and structure (monodispersity) is of great interest. To date, there

are two general approaches to prepare nanomaterials: one is top-down method (lithography and mechanical milling), and the other is bottom-up (building blocks from atomic level) method. For mass production, top-down method which is physcial breaking of bulk materials into nanomaterials has been widly used. However, this method is lack of fine tuning of nanomaterials in size and structure. In contrast, bottom-up method manipulates nucleation and growth of atoms to control the size, shape and morphology of nanostructures. In the past decades, a variety of bottom-up approaches have been developed for synthesizing NPs with great quality. These include co-precipitation of metal salts in basic solutions, chemical vapor deposition (CVD), template growth, sol-gel method, hydrothermal/solvothermal synthesis and *etc.*[18-19] Among all these methods, the organic solution phase solvothermal synthesis has been demonstrated to be a reliable way for producing the desired nanostructures with fine control. The organic solution phase synthesis follows generally the La Mer model. Figure 1.1 demonstrates the principle for synthesizing monodisperse NPs. The chemical reaction between reactants should first induce a burst nucleation (nucleation in a short period of time) by raising the precursor concentration above the critical supersaturation level. Then the nucleation event happens and lowers the precursor concentration to be below the supersaturation level. The rest of the precursors are deposited on the existing nuclei to grow into NPs. The following high temparture and longer time aging promotes Ostwald Ripening, a thermodynamically-driven spontaneous process in which small NPs with high surface energy tend to be

dissolved and redeposited on the larger NPs, producing NPs with narrow size distribution. This organic solution phase synthesis is powerful to control NPs' size, shape, composition and structure by varying reaction conditions, such as different kind of metal precursors, reducing agents, surfactants and reaction temperatures, producing NPs with desired parameters.

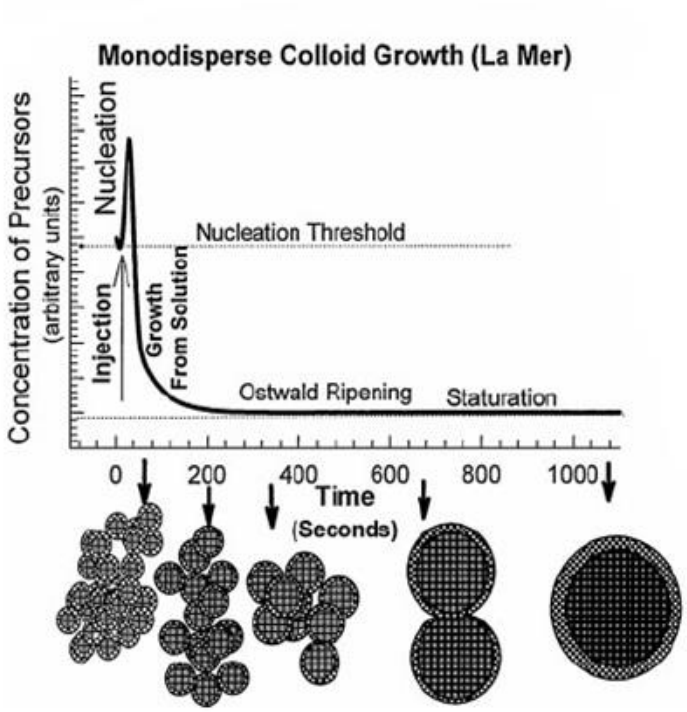

Figure 1.1 Schematic illustration of La Mer model to show NPs' nucleation and growth process.[20]

1.3 Nanoparticles for Catalytic Applications

Among different applications nanomaterials can be used in, catalytic application of nanomaterial is the most exciting subfield. The large surface-to-volume ratio

presented in nanostructure brings in the large surface area for catalytic reaction to happen. Figure 1.2 shows that a single cube with length of 1 cm has a total surface area of 6 cm^2. When this cube (1 x 1 cm) is separated into 1 x 1 mm cubes, the total surface area is increased to 60 cm^2. If this cube is consisted of 10^{21} 1 x 1 nm cubes, the total surface area can reach up to 6000 m^2 ! This largely increased surface area of NPs can provide abundant active sites for catalytic reactions. Additonally, The surface energetics for catalytic adsorption and desorption can be readily tuned by the precise control of the nanostructure, making nanomaterials to be the ideal platform for catalysis.

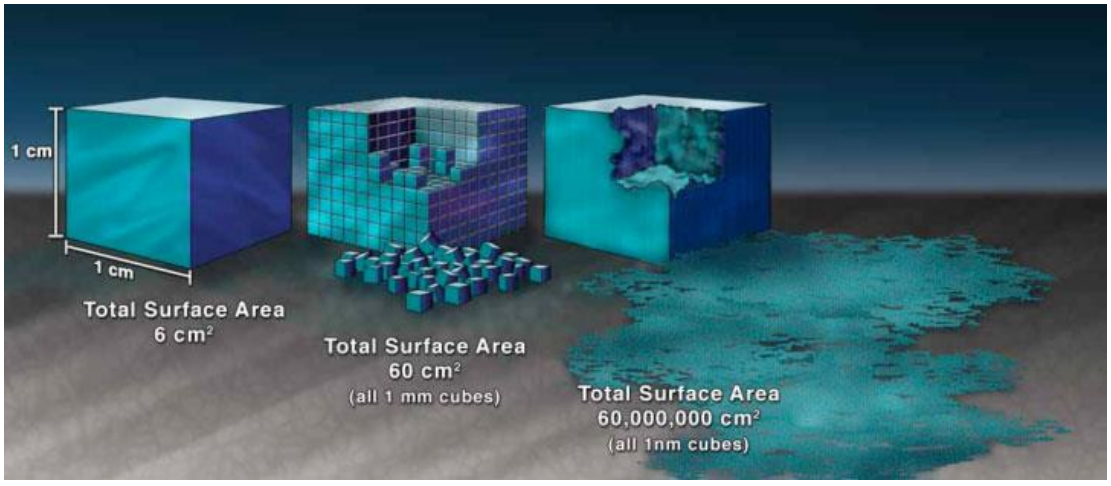

Figure 1.2 Illustration demonstrating the effect of the increased surface area provided by nanostructured materials.[21]

1.3.1 Fuel Cell and Fuel Cell Catalysts

A fuel cell is an energy conversion device to convert chemical energy into electric energy. It contains two electrodes, anode and cathode, and an electrolyte

separator that is sandwiched by these two electrodes. Fuel is oxidized at anode, releasing electrons and cations. Electrons travel along an external circuit to power an electronic device. Cations penetrate the separator which is an electron insulator and an excellent cation conductor to arrive at cathode. Depending on the fuel used, various forms of fuel cells have been designed, among which a proton exchange membrane fuel cell (PEMFC) is featured by low operation temperature, high energy density, high conversion efficiency, and low environmental impact.[22-23] Figure 1.3 illustrates the schematics of the PEMFC with hydrogen (H_2) as the fuel and O_2 as an oxidizer. When H_2 is oxidized, electrons and protons, H^+ are produced. While electrons are drawn to the external circuit by the electronegative O_2 at the cathode in a process known as oxygen reduction reaction (ORR), the H^+ migrates from anode to cathode from inside through the separator to neutralize the reduced O_2 to form water, H_2O. To facilitate H^+ conduction, an acidic polymer-membrane, Nafion, a copolymer of tetrafluoroethylene and perfluoro-2-(fluorosulfonylethoxy) propylvinylether was used as a separator.[24] Therefore, the H_2-based PEMFC is the device to convert the energy stored in H_2 into electric energy via chemical reaction, $2H_2 + O_2 \rightarrow 2H_2O$, with H_2O as the only product. To avoid the problematic issues associated with H_2 production, transportation and storage, other organic fuels, such as formic acid, methanol or even ethanol, have been explored as alternative fuels to be used in PEMFCs.

Despite the promising perspectives shown as an alternative energy source and the

great efforts devoted to the device developments, the PEMFC technology is still considered too expensive for large scale commercial applications. A major limitation is in its dependence on platinum (Pt), an expensive, yet not easily available, noble metal, for normal fuel cell operations. For fuel to release electrons at anode and O_2 reduction at cathode, Pt catalysts must be present at both electrodes to lower the reaction overpotentials and to maximize voltage output. However, Pt is neither cost-efficient nor highly durable (prone to be oxidized, dissolved, agglomerated or poisoned by CO) to use in the fuel cell reaction conditions.[25-27] Consequently, recent research and development efforts have been dedicated to minimize the use of Pt by controlling Pt NP size and shape, by alloying Pt with other early transition metals, and/or by creating core/shell morphologies to obtain the optimal catalysis. Ideally, Pt catalysts can be replaced totally by those based on earth-abundant non-noble elements.

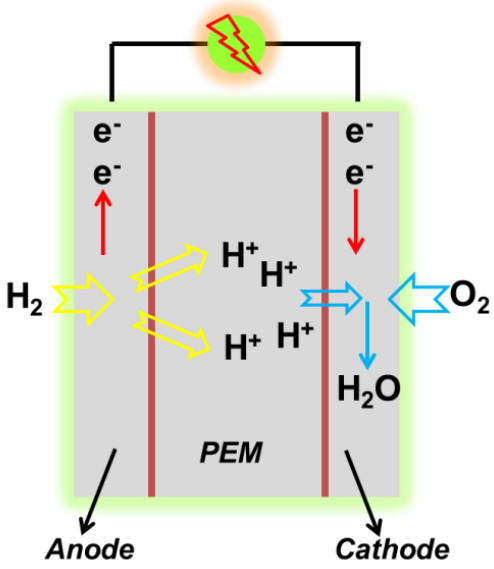

Figure 1.3 Schematic illustration of a typical PEM fuel cell with H_2 as fuel.

ORR is a common chemical reaction at cathode to accept electrons in a PEMFC and many other types of fuel cell devices. For O_2 to be reduced completely, 4 electrons are required to break the O=O double bond with additional energy needed to reverse the triplet spin in O_2 to singlet in H_2O. This makes the ORR process kinetically more sluggish than the H_2 oxidation one at the anode. As a result, ORR contributes in large part to electrochemical over-potentials observed in the PEMFC. ORR in an acid electrolyte can undergo via either a direct 4-electron pathway to form H_2O (1) or two 2-electron pathways with H_2O_2 produced as an intermediate (2a &b). In alkaline electrolyte, the process is similar. But instead of generating H_2O_2, HO_2^- is generated as intermediate. The two-electron pathways should be avoided because in the presence of a trace amount of metal ions, H_2O_2 can be decomposed, generating hydroxyl and hydroperoxyl radicals (OH• & OOH•) that is strongly oxidative and can cause severe degradation of proton exchange membrane.[28] ORR on the Pt catalyst surface is mainly a 4-electron process; however its exact mechanism is still elusive with both associative (proton attacks O_2 first) and dissociative (O_2 dissociates first) pathways been proposed.[29-30] Although the whole ORR process is very complicated and elusive, it can be summarized as the adsorption and desorption of oxygenated intermediate species (O*, OH*, OOH* etc.). Consequently, ORR dynamics can be determined by the surface oxygen adsorption energy (E_o) of a catalyst. Recently, some theoretical calculations have concluded that the E_o should be in a proper level

to support the favorable dynamics of ORR on the electrochemical interface, where the bonding of oxygenated species is neither too strong nor too weak. The pure Pt have too strong bonding with oxygenated species (high E_o), indicates the ORR on Pt surface is limited by desorption.[31] To improve the ORR kinetics on Pt NPs, the strong adsorption of oxygenated species should be eased. In my PhD research, I was focused on the sysnthesis of 1-dimensional (1-D) Pt-based NWs (Chapter 3-5), structure-controlled FePt NPs (Chapter 6) and non-noble metal metal oxides for ORR (Chapter 7).

$$O_2 + 4\,H^+ + 4e^- \rightarrow 2\,H_2O \qquad (1)$$

$$O_2 + 2H^+ + 2e^- \rightarrow H_2O_2 \qquad (2a)$$

$$H_2O_2 + 2H^+ + 2e^- \rightarrow 2H_2O \qquad (2b)$$

Formic acid, HCOOH, is a promising alternative fuels due to easy transportation, storage comparing with H_2 and low cross-over flux which is referred to as the fuel (CH_3OH) migration through proton exchange membrane to the cathode, interfering with the ORR. When HCOOH is used, its cross-over problem can be minimized due to electrostatic repulsion of $HCOO^-$ and $-SO^{3-}$ in Nafion. The complete anode reaction for the FAOR is as follows (3):

$$HCOOH \rightarrow CO_2 + 2H^+ + 2e^- \qquad (3)$$

This is commonly called dehydrogenation pathway. But on the Pt catalyst, HCOOH tends to undergo non-faradaic dehydration first (Figure 1.4 I_1), generating CO (4) that

poisons the Pt surface by forming Pt-CO, and needs more energy input to oxidize CO (5) (Figure 1.4 I_2) and to regenerate active Pt surface.[32-33]

$$HCOOH \rightarrow CO_{ads} + H_2O \quad (4)$$

$$\rightarrow CO_2 + H^+ + 2e^- \quad (5)$$

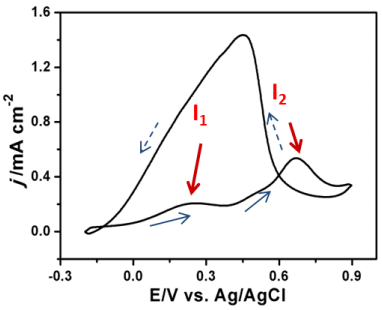

Figure 1.4 CVs of FAOR on commercial Pt NPs.

An ideal catalyst for FAOR should be able to efficiently catalyze the FAOR in dehydrogenation pathway without generating CO. Pt's activity for FAOR is strongly suppressed by the CO-poisoning associated with the undesired non-faradic dehydration pathway. Alloying Pt with other metals such as Pb and Bi, is effective in improving FAOR efficiency by eliminating the CO-poisoning on Pt.[34-35] During my PhD research, I developed advanced structure controlled FePtAu NPs as high active and durable catalysts for formic acid oxidation (FAOR) (Chapter 9).

1.3.2 Nanoparticles for Biodetection Application

Ultrasentive bioprobes are of great importance for pathological, physiological and

biomedical purpose. Biocompatible NPs can potentially serve as active alternatives to traditional enzyme-based biosensors due to the ease of preparation and much better stabilities. These NPs based biopobes can in-vivo or in-vitro catalyze some chemical reactions, linking the small molecules of interest to easily detectable signals. The large surface area of nanomaterials, plus their artificially tunable surface electronic structures, makes them ideal platforms for optimized biodetection. Thus far, very few study based on NPs biodetection has been reported with high sensitivity and selectivity. I studied the synthesis of AuMn alloy NPs. Through controlled oxidation, these NPs can be converted into Au-MnO nanocomposites and were found to be high sensitive in catalyzing H_2O_2 reduction (Chapter 8).

Reference:

1. R. P. Feynman, *Eng. Sci*. **1960**, *23*, 22-27.
2. P. Buffat, J. P. Borel, *Phys. Rev. A* **197**6, *13*, 2287-2298
3. S. C. Tjong, *in Nanocrystalline Materials*, Elsevier Science Ltd, Oxford, **2006**, pp. ix.
4. C. B. Murray, D. J. Norris, M. G. Bawendi, *J. Am. Chem. Soc.* **1993**, *115*, 8706-8715.
5. I. L. Medintz, H. T. Uyeda, E. R. Goldman, H. Mattoussi, *Nat. Mater.* **2005**, *4*, 435-446.
6. M. B. Cortie, A. M. McDonagh, *Chem. Rev.* **2011**, *111*, 3717-3735.
7. Y. Xia, Y. Xiong, B. Lim, S. E. Skrabalak, *Angew. Chem. Int. Ed.* **2009**, *48*, 60-103.
8. K. M. Mayer, J. H. Hafner, *Chem. Rev.* **2011**, *111*, 3828-3857.
9. V. Talapin, J.-S. Lee, M. V. Kovalenko, E. V. Shevchenko, *Chem. Rev.* **2010**, *110*, 389-458.
10. N. A. Frey, S. Peng, K. Cheng, S. Sun, *Chem. Soc. Rev*. **2009**, *38*, 2532-2542.
11. W. C. W. Chan, S. Nie, *Science* **1998**, *281*, 2016-2018.
12. S. Zhang, J. Lee, S. Sun, *The Open Sur. Sci. J.* **2012**, *4*, 26-34.

13. P. Alivisatos, *Nat. Biotech.* **2004**, *22*, 47-52.

14. J. P. Wolfgang, et al., *Nanotechnology* **2003**, *14*, R15-R27.

15. C. M. Niemeyer, *Angew. Chem. Int. Ed.* **2001**, *40*, 4128-4158.

16. L. He, M. D. Musick, S. R. Nicewarner, F. G. Salinas, S. J. Benkovic, M. J. Natan, C. D. Keating, *J. Am. Chem. Soc.* **2000**, *122*, 9071-9077.

17. L. A. Lyon, M. D. Musick, M. J. Natan, *Anal. Chem.* **1998,** *70*, 5177-5183.

18. Cushing, B. L.; Kolesnichenko, V. L., O'Connor, C. *J. Chem. Rev.* **2004**, *104*, 3893-3946.

19. Burda, C.; Chen, X.; Narayanan, R.; EI-Sayer, M. E. *Chem. Rev.* **2005**, *105*, 1025-1102.

20. C. B. Murray, C. R. Kagan, M. G. Bawendi, *Annu. Rev. Mater. Sci.* **2000**, *30*, 545-610.

21. *What's so special about the nanoscale?* Vol. 2011, The United States National Nanotechnology Initiative, **2011**.

22. G. Lota, K. Fic, E. Frackowiak, *Energy Environ. Sci.* **2011**, *4*, 1592-1605.

23. B. Seger, P. V. J. Kamat, *J. Phys. Chem. C.* **2009**, *113*, 7990-7995.

24. S. Guo, S. Zhang, S. Sun, *Angew. Chem. Int. Ed.* **2013**, *52*, 8526-8544.

25. Y.-J. Wang, D. P. Wilkinson, J. Zhang, *J. Chem. Rev.***2011**, *111*, 7625-7651.

26. Z. Chen, M. Waje, W. Li, Y. Yan, *Angew. Chem. Int. Ed.* **2007**, *46*, 4060-4063.

27. C. Koenigsmann, E. Sutter, T. A. Chiesa, R. R. Adzic, *Nano Lett.* **2012**, *12*, 2013-2020.

28. V. A. Sethuraman, J. W. Weidner, A. T. Haung, S. Motupally, L. V. Protsailo, *J. Electrochem. Soc.* **2008**, *155*, B50-B57.

29. Y. Zheng, Y. Jiao, M. Jaroniec, Y. Jin, S. Z. Qiao, *Small* **2012**, *8*, 3550-3566.

30. D.-H. Lim, J. Wilcox, *J. Phys. Chem. C* **2012**, *116*, 3653-3660.

31. J. K. Nørskov, J. Rossmeisl, A. Logadottir, L. Lindqvist, J. R. Kitchin, T. Bligaard, H. Jonsson, *J. Phys. Chem. B* **2004**, *108*, 17886-17892.

32. A. Chen, P. Holt-Hindle, *Chem. Rev.* **2010**, *110*, 3767-3804.

33. X. Yu, P. G. Pickup, *J. Power Sources* **2008**, *182*, 124−132.

34. Y. Kang, L. Qi, M. Li, R. E. Diaz, D. Su, R. R. Adzic, E. Stach, J. Li, C. B. Murray, *ACS Nano* **2012**, *6*, 2818-2825.

35. X. Ji, K. T. Lee, R. Holden, L. Zhang, J. Zhang, G. A. Botton, M. Couillard, L. F. Nazar, *Nat. Chem.* **2010**, *2*, 286-293.

Chapter 2

General Experimental Setup

2.1 General Synthesis Set Up

Figure 2.1 shows a typical experiment set up for the high temperature organic solution phase synthesis. The chemical reaction is carried out in a four neck flask (50 mL) under the protection of inert gas (N_2 or Ar) integrated into a standard Schlenk line. A self-washing rotary evaporator is mounted in the middle neck of the flask as the gas inlet, a rotary trap on the right as the gas outlet for collecting low boiling point impurities and by-products. A thermal sensor (platinum RTD temperature sensor) is fitted in the flask to monitor the reaction temperature and a rubber septum is mounted on the left to seal the system. The reaction temperature is controlled by a hemispherical mantle (80 W-115 V, Ace Glass, Inc) coupled with a digital temperature controller (Dyna-Sense®, VWR) and a variable transformer with a voltage output range 0-140 V (Ace Glass, Inc.). The reaction solution is stirred by a Teflon coated magnetic bar driven by a magnetic stirrer (VWR®, 620-HPS).

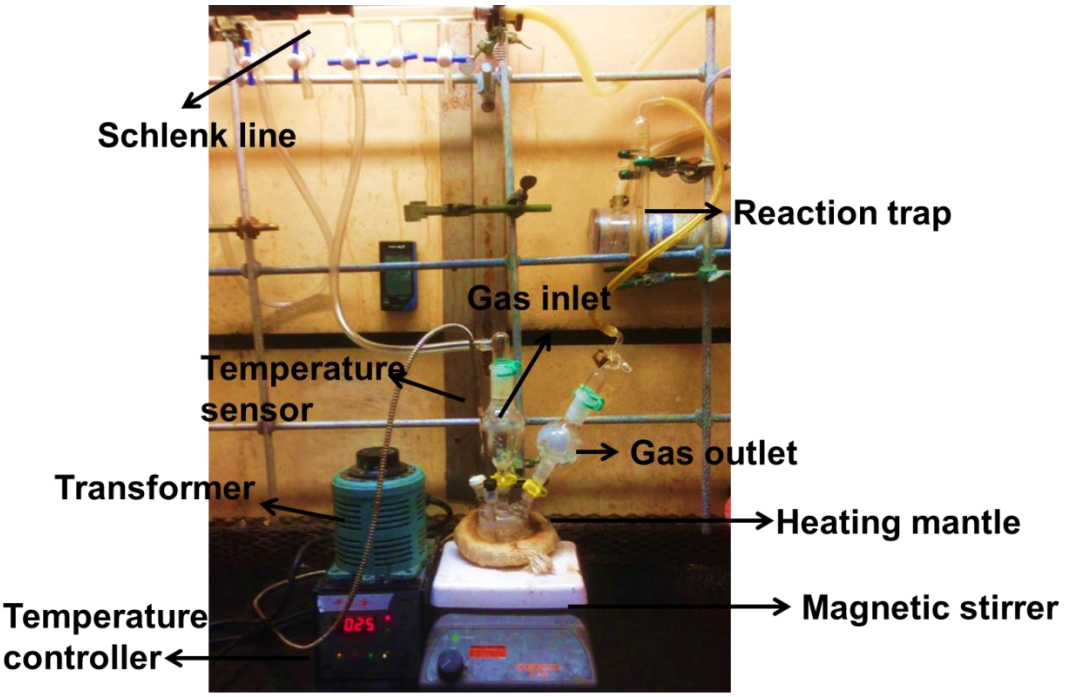

Figure 2.1 A typical experimental set up for high temperature organic phase NP synthesis.

2.2 Chemicals

Typical chemicals used in the experiments were ordered from Sigma-Aldrich or Strem Chemicals. They are used as received without any further purification. Details of the chemicals are provided in the experimental section of each chapter.

2.3 Product Collection and Purification

After the synthesis, the reaction solution is air-cooled down to room temperature. The as-synthesized NPs are stabilized by non-polar hydrocarbon surfactants to prevent agglomeration. In order to collect the NPs from the reaction mixture, polar solvents such as isopropanol, ethonal or acetone are added into the solution. The

polar solvent is carefully chosen to be miscible with the non-polar hydrocarbon solvents used in the reaction. For example, isopropanol is usually used to precipitate NPs in 1-octadecene. Ethanol is used to precipitate NPs in oleylamine and aceton is used to precipitate NPs in tetralin. The NPs are then collected by centrifugation (Beckman Coulter Allegra® 64R Centrifuge, C0650 rotor) with 8000-10000 rpm and varied time 5-8 min. The supernatant is removed and the precipitated NPs are redispersed into a non-polar solvent such as hexane or toluene. An appropriate amount of ethanol (15-35 mL) is added for another wash. The ethanol washing is repeated for 2-3 times to remove excess surfactants. At the end, the NPs are redispersed and stored in hexane or toluene for following usage.

2.4 Nanoparticles Characterization

2.4.1 Transmission Electron Microscopy (TEM)

The sample for TEM image is prepared by adding one drop of the dilute NPs in hexane on a Formvar/carbon coated copper grid (Ted Pella, Inc., 01754-F) and dried at ambient condition. TEM images are collected on a Philips FEI CM 20 (200 kV).

2.4.2 High Resoution Transmission Electron Microscopy (HRTEM)

The sample preparation of HRTEM is same as in the TEM. Most of the HRTEM images are obtained with JEOL 2100F (200 kV) or JEOL 2010 (200 kV) at Brown University. Some HRTEM images are obtained with a JEOL 2100F (200 kV) with a field-emission electron source and a FEI Titan 80-300 (300 kV) with an aberration (image) corrector in the Center for Functional Nanomaterials at Brookhaven National

Lab.

2.4.3 High-Angle Annular Dark-Field Scanning TEM (HAADF-STEM) and STEM-Electron Energy Loss Spectroscopy (STEM-EELS)

High Resolution Aberration-Corrected High-Angle Annular Dark-Field Scanning TEM (HAADF-STEM) images, elemental map images and STEM-EELS are obtained on a Hitachi HD2700C (200kV) with a probe aberration-corrector, in the Center for Functional Nanomaterials at Brookhaven National Lab. Samples are prepared by adding a drop of diluted NP hexane dispersion on an ultrathin carbon (<3nm)/holey support film coated copper grid (Ted Pella, Inc., 01824).

2.4.4 X-ray Diffraction (XRD) Pattern

The XRD patterns are recorded by a Bruker AXS D8-Advanced diffractometer with Cu Kα radiation (λ = 1.5418 Å). The XRD sample is prepared by dropping and drying NP hexane dispersion or depositing powders on the glass slide.

2.4.5 Inductive Coupled Plasma Atomic Emission Spectroscopy (ICP-AES)

The ICP-AES measurement was performed on a JY2000 Ultrace ICP Atomic Emission Spectrometer equipped with a JY AS 421 autosampler and 2400 g/mm holographic grating. The ICP samples were prepared by dissolving NPs in 5-6 drops of fresh aqua regia, followed by adding 5-6 mL 2% HNO_3 to form a clear solution.

2.4.6 Electrochemistry Setup

Electrochemistry measurements are performed on a Fuel Cell Electrocatalyst Bundle from Pine Potentiostat (AFCBP1) or Autolab 302 Potentiostat. A typical three

electrode system is used, including a glass carbon rotating disk (5 mm in diameter) as the working electrode, a Pt wire as the counter electrode and an Ag/AgCl (Autolab, double junction with outer tube filled with 4 M KCl) as the reference electrode. The sample is prepared by depositing 20 μL NPs/C dispersion on glassy carbon electrode and drying at ambient condition.

2.4.7 UV/Vis Measurements

UV/Vis spectra is recorded on a Perkin Elmer Lambda 35 spectrometer. Hexane is used as the blank. The absorbance of the diluted NPs' hexane dispersion is then recored.

2.4.8 Magnetic Measurements

The magnetic hysteresis loops are collected on a Vibrating Sample Magnetometer (VSM) (LakeShore, 7404) with a field up to 1.5 kOe. The NPs are washed with ethanol and then dried at room temperature to form powder. Several mg of the powder is transferred to a gelatin capsule (0.3 ml, Electron Microscopy Science) with a cotton ball being pressed on the powder in the capsule.

Chapter 3

MPt (M=Fe, Co) Nanowires as Efficient Catalyts for Oxygen Reduction Reaction

3.1 Background and Introduction

Previous efforts in developing high efficient catalysts for oxygen reduction reaction (ORR) were centered on tuning of Pt d-band center to get an optimal Pt-O binding energy (E_o). This can be achieved either through electronic (ligand) effect in alloy structure or through strain effect in core/shell structure. For example, alloying Pt with 3d transition metals can downshift the Pt d-band center and decreases E_o.[1] This alloy-induced electronic effect is strongly dependent on the alloy composition. In the study of single crystalline thin film of Pt_3M alloys (M=Ti, V, Fe, Co, Ni) as shown in Figure 3.1.1, the proper downshift of the d-band center leads to the balance between strong adsorption and strong desorption.[2] As a result, Pt_3Co reaches the best energy level and the highest ORR activity. On the other hand, alloying Pt with Ti or V, the down-shift of the Pt d-band is away from the optimal value. Consequently, the ORR process is limited by slow adsorption and activation. The similar trend has also been observed in nanoparticles' (NPs') system with CoPt, NiPt and FePt being reported to be more active than pure Pt NPs.[3]

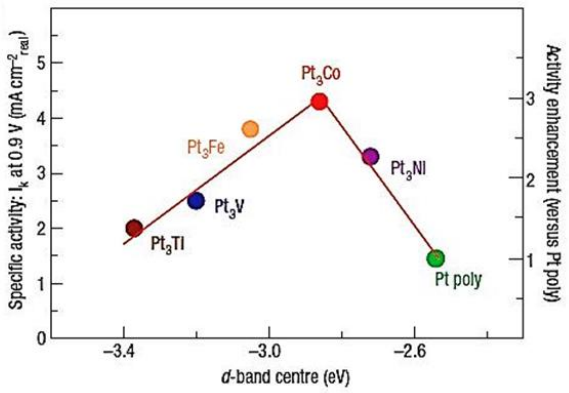

Figure 3.1.1 Relationships between experimentally measured specific activities for the ORR on Pt_3M single crystalline surfaces in 0.1 M $HClO_4$ versus the d-band center position.[2]

Core/shell structure with Pt as a shell and other components as a core is an appealing motif in the design of highly efficient catalyst for ORR. It has a maximal Pt effective utilization ratio comparing to conventional Pt NPs. Furthermore, the activity and durability of the Pt shell can be strongly influenced by the core component due to the electronic and strain effects. This core/shell effect can be easily realized by dealloying MPt NPs to form MPt/Pt core/shell NPs. For example, in the electro-anodizaion, the redox potential difference of M and Pt results in a preferential oxidation and dissolution of M at the surface, generating a Pt-rich surface around the NPs. This strategy has been demonstrated in the preparation of CuPt/Pt NPs by dealloying Cu from the Pt surface. These core/shell NPs exhibit the higher ORR activity than the Pt NPs, correlating with the strain effect in the CuPt/Pt structure.

This arises from lattice mismatch between the CuPt core (with a smaller crystalline lattice) and the Pt shell (with a larger crystalline lattice) (Figure 3.1.2A), inducing a compression strain on Pt shell and the downshift of Pt d-band center. Moverover, this strain is tunable by different CuPt compositions (Figure 3.1.2B).[4]

(A) (B)

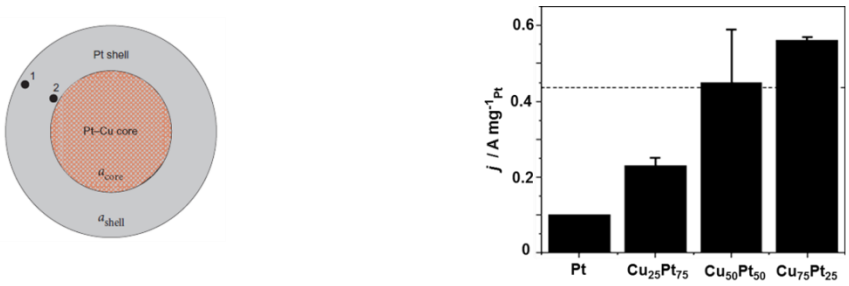

Figure 3.1.2 (A) The schematic illustration of Pt-Cu/Pt core/shell structure; (B) composition dependent of the ORR specific activity of CuPt NPs.[4]

However, till now most of the efforts in developing Pt-based ORR catalysts is still focused on 0-dimensional (0-D) NPs.[5-9] 1-D nanomaterial is more appealing due to the less defects presented on the surface, more resistance to dissolution and Ostwarld ripening.[10-11] They may be more robust than their 0-D counterparts in catalyzing ORR. Figure 3.1.3 shows a schematic illustration of the electron transfer process on both NPs and 1-D naowires (NWs) and nanorods (NRs). Here, we want to study the 1-D nanomaterials (NWs and NRs) which have a stronger interaction between the

nanomaterial and the carbon support than NPs and thus can potentially bring in an enhanced durability of the catalysts due to this strong interaction. Furthermore, the interface is maximized in these 1-D nanostructure, thus electrons can be transferred from the support to the catalyst then to the O_2 through multi-channel path comparing with NPs which could result in an improved activity. It worth mention that the 1-D nanostructure we want to develop needs to be ultrathin with their diameter to be less than 5 nm in order to get a balance between the 1-D effect and the mass activity of the catalyst.

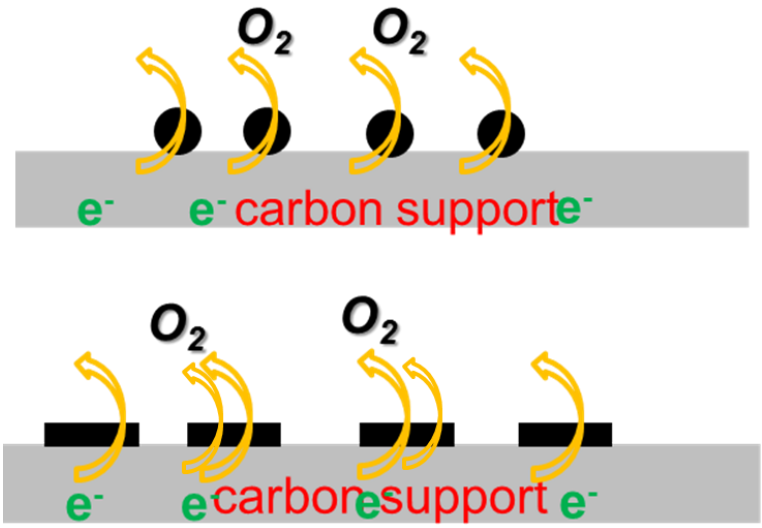

Figure 3.1.3 Schematic illustration of the electron transfer process on nanoparticles and on 1-D nanomaterials.

3.2 Experimental

Chemicals and Materials

Oleylamine (OAm, >70%), oleic acid (OA, 90%), 1-octadecene (ODE, 90%), $Fe(CO)_5$ (99.9+% trace metals basis), hexane (98.5%), ethanol (100%), acetic acid (AA, 99%) and 1,2-dichlorobenzene (DCB) were purchased from Sigma-Aldrich. $Pt(acac)_2$ (99.99%) was purchased from Strem. Sodium oleate (Na-oleate) (97%) was obtained from Tokyo Chemical Industry CO., LTD. The commercial C-Pt catalyst (46% loading) was purchased from BASF Company. The deionized water was obtained from a Millipore Autopure system.

Characterization

XRD characterizations were carried out on a Bruker AXS D8-Advanced diffractometer with Cu Kα radiation (λ =1.5418 Å). TEM images were obtained from a Philips CM 20 operating at 200 kV. TEM and HRTEM samples were prepared by depositing a single drop of diluted NPs dispersion on amorphous carbon coated copper grids. The inductively coupled plasma-atomic emission spectroscopy (ICP-AES) measurements were carried on a JY2000 Ultrace ICP Atomic Emission Spectrometer equipped with a JY AS 421 autosampler and 2400g/mm holographic grating. Electrochemical measurements were performed on a Autolab 302 potentiostat (6 mm GC). Reversible hydrogen was used as a reference electrode and platinum wire as a counter electrode.

Synthesis of MPt (M=Fe, Co) NWs

Under a gentle nitrogen flow and magnetic stirring, sodium oleate (0.3 g) was dissolved in ODE (12 mL) by heating the suspension to 180 ^{o}C. The solution was air-cooled to 60 ^{o}C, followed by the addition of $Pt(acac)_2$ (0.2 g) in 8 mL OAm and

further heating to 115 ^{o}C. Under a blanket of nitrogen, different amounts of $Fe(CO)_5$ and $Co_2(CO)_8$ (dissolved in 1,2-dichlorobenzene) were injected into the reaction solution. The solution was further heated to 240 ^{o}C at a ramping rate of 4–5 ^{o}C/min and kept there for 25 min. with different compositions. The NWs were separated by adding ethanol (50 mL), followed by centrifugation (9500 rpm, 10 min) followed by ethanol wash for twice. Different composition was obtained by varying the amount of $Fe(CO)_5$ and $Co_2(Co)_8$, as summerized in **Table 3.1**.

Catalyst Preparation

20 mg of NWs in 20 mL hexane were mixed with Ketjen 30 mg carbon suspended in a mixture of hexane/acetone (v/v 2:1, 30 mL). The mixture was sonicated for 1 h. The loading amounts of NWs on the carbon support were calculated from ICP to be 25.2% and 23.8% for FePt and CoPt. The C-NW catalyst was separated by centrifugation, washed twice with hexane, and mixed with acetic acid (30 mL). The suspension was heated at 70 ^{o}C for overnight. The product was then redispersed in a mixture of deionized water, isopropanol and Nafion (V/V/V = 4/1/0.05). 20 μL catalyst ink (2 mg/mL) was deposited on the working electrode (glassy carbon rotating disk electrode, GC-RDE) that was polished prior to catalyst deposition by 0.1 μm and 0.05 μm alumina powder and rinsed by sonication in ethanol and in deionized water. The catalyst was dried at ambient condition.

Electrochemical Measurements

Cyclic voltammograms (CVs) were obtained by scaning between 0.05 V-1.02 V *vs* RHE at a scan rate of 50 mV/s in Ar-saturated 0.1M $HClO_4$. ORR polarization curves

were obtained by scaning the potentials at a scan rate of 20 mV/s in O_2-saturated 0.1 M $HClO_4$ with the GC-RDE rotating at 1600 rpm.

3.3 Results and Discussion

3.3.1 Synthesis and Characterization of MPt (M=Fe, Co) NWs

Since both Fe and Co show important alloying effect on Pt, we start from FePt and CoPt NWs. FePt NWs were synthesized by co-reduction of platinum acetylacetonate, $Pt(acac)_2$, and thermal decomposition of iron pentacarbonyl, $Fe(CO)_5$ according to modified previous method (see **Experimental**).[12] Different from the previous approach to FePt NPs [13] and FePt NWs,[12] the current synthesis was performed in 1-octadecene (ODE) with sodium oleate (Na-oleate) and oleylamine (OAm). Depending on the metal carbonyl ($Fe(CO)_5$ or $Co_2(CO)_8$) used, FePt or CoPt NWs were obtained at a high synthetic yield and with the desired control over alloy composition. In the synthesis, OAm and Na-oleate were used to stabilize the NPs. $Fe(CO)_5$ or $Co_2(CO)_8$ was used as both the Fe or Co precursor and reducing agent. Fe/Pt ratio can be controlled by varing the Fe and Pt precursor ratio. However, in the synthesis of CoPt NWs, the amount of $Co_2(CO)_8$ added in the reaction mixture was the key to the formation of NW product. Too much (0.795 mmol) or too little (0.265 mmol) $Co_2(CO)_8$ would result in a mixture of NPs and thick NWs or a mixture of NPs and thin NWs. The final product ratio was measured by coupled plasma-atomic emission spectroscopy (ICP-AES) and summarized in Table 3.1. Transmission

electron microscopy (TEM) was used to characterize the NWs' morphology. Figure 3.2.1 shows the mixture of NWs and NPs with improper amount of Co-precursor. Figure 3.2.2 and Figure 3.2.3 show the representative transmission electron TEM images of the FePt and CoPt NWs with diameters at (2.5 ± 0.3) nm. The length of the FePt NWs is in the range of 30–100 nm and that of CoPt NWs in the range of 50–500 nm.

A $Fe(CO)_5$:$Pt(acac)_2$=1:0.5 (mmol)	Fe:Pt=68:32
B $Fe(CO)_5$:$Pt(acac)_2$=0.57:0.5 (mmol)	Fe:Pt=56:44
C $Fe(CO)_5$:$Pt(acac)_2$=0.32:0.5 (mmol)	Fe:Pt=42:58
D $Co_2(CO)_8$:$Pt(acac)_2$=0.53:0.5 (mmol)	Co:Pt=63:37
E $Co_2(CO)_8$:$Pt(acac)_2$=0.4:0.5 (mmol)	Co:Pt=32:68

Table 3.1 The composition control of as-synthesized FePt, CoPt NWs by varying the precursor ratio.

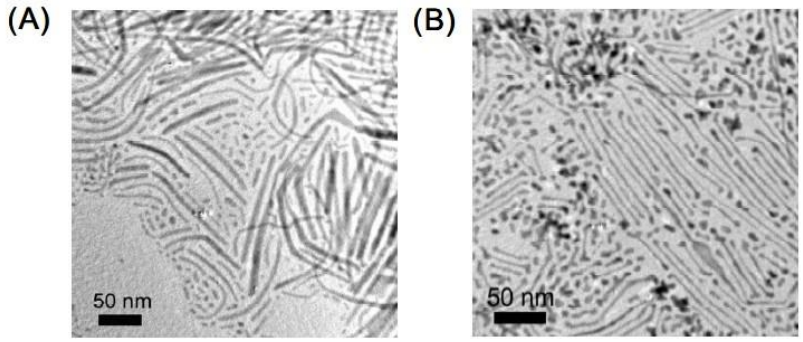

Figure 3.2.1 TEM images of different CoPt nanomaterials obtained through adding (A) 270 and (B) 90 mg $Co_2(CO)_8$ into the mixture containing $Pt(acac)_2$.

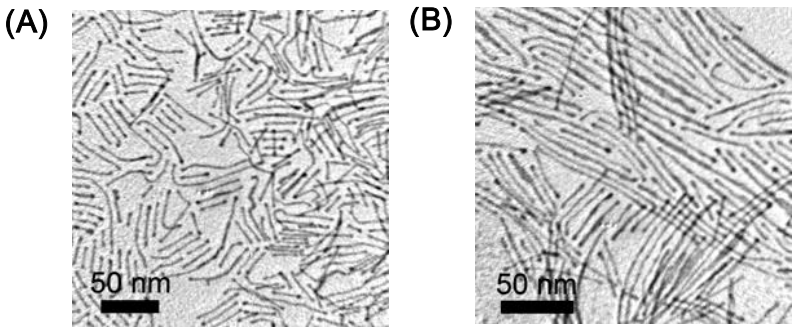

Figure 3.2.2 TEM images of (A) $Fe_{56}Pt_{44}$ and (B) $Co_{63}Pt_{37}$ NWs.

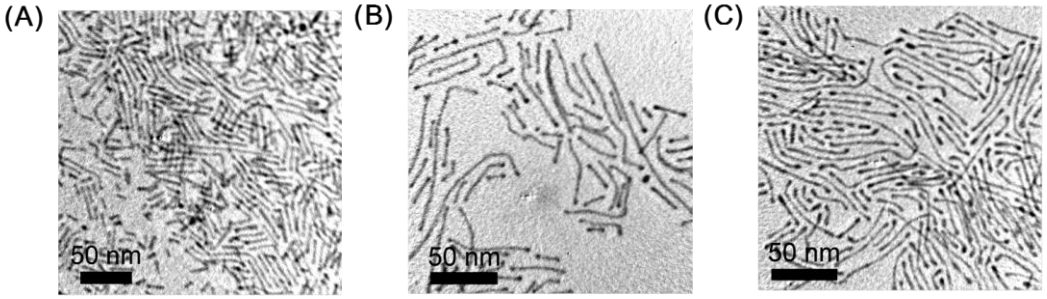

Figure 3.2.3 TEM images of (A) $Fe_{42}Pt_{58}$, (B) $Fe_{68}Pt_{32}$, and (C) $Co_{32}Pt_{68}$ NWs.

The FePt and CoPt NWs were further characterized by X-ray diffraction (XRD) in Figure 3.2.4. The broadened diffraction peaks from these NWs reveal the small dimension of the chemically disordered face centered cubic (*fcc*) crystal domains.

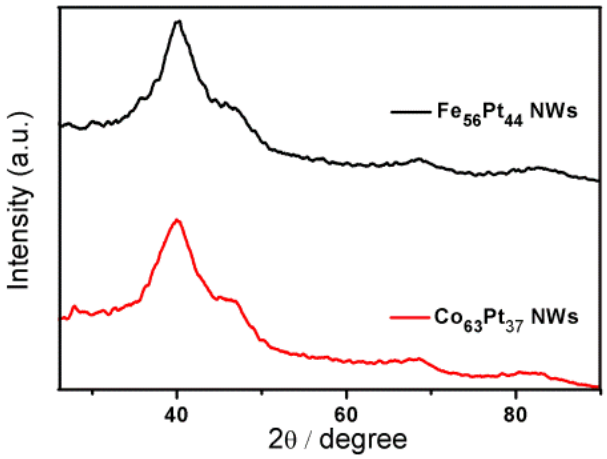

Figure 3.2.4 XRD patterns of (A) $Fe_{56}Pt_{44}$ and (B) $Co_{63}Pt_{37}$ NWs.

3.3.2 Catalytic Properties of MPt (M=Fe, Co) NWs

The as-synthesized MPt (M=Fe, Co) NWs were studied as catalysts for ORR. To perform the study, the NWs were first deposited on a carbon (C) support (Ketjen EC-300J) by sonicating the mixture of NWs and C (NW/C=4:6 by weight) in hexane/acetone (v/v=2:1) and then washed with acetic acid (99%) at 70 ^{o}C for overnight to remove the surfactant. The acid washing is an efficient process to protonate the OAm and leaves a clean surface for the catalytic reaction as illustrated in Figure 3.2.5.[14] Upon this acid treatment, part of the Fe in the FePt NWs was etched away, as confirmed by the change of the composition from $Fe_{42}Pt_{58}$, $Fe_{56}Pt_{44}$, and $Fe_{68}Pt_{32}$ to $Fe_{15}Pt_{85}$, $Fe_{20}Pt_{80}$, and $Fe_{23}Pt_{77}$, respectively. After the same treatment with acetic acid, a substantial amount of Co was lost, and less than 10% Co was retained in the NW structure. This indicates that CoPt NWs are more vulnerable to acid than FePt NWs.

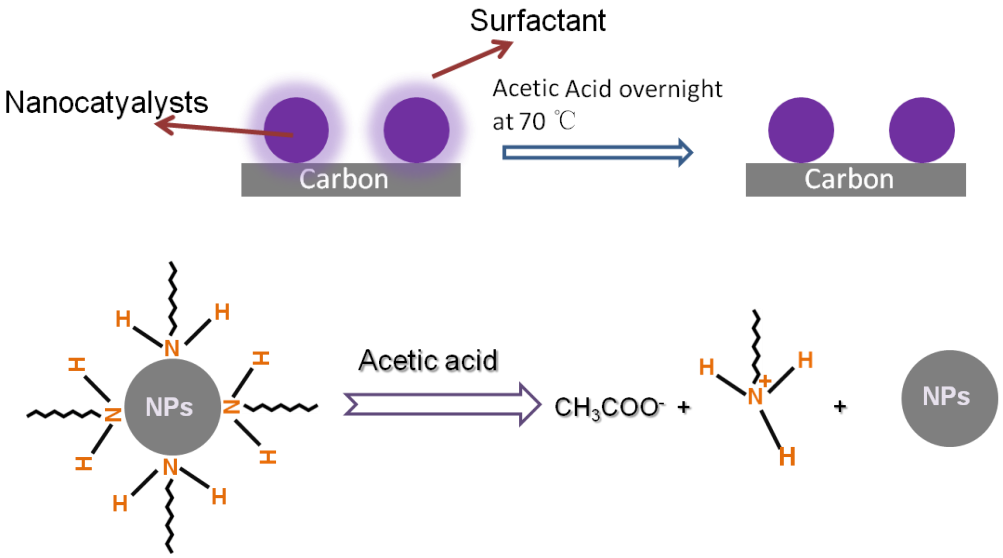

Figure 3.2.5 Schematic illustration of acetic acid treatment to remove the surfactant on NP surface.

Cyclic Voltammetry (CV) was first obtained to study the electrochemical active surface area (ECASA) based on H_2 underpotential formation/stripping.[15] Figure 3.2.6A shows the typical cyclic voltammograms (CVs) of the $Fe_{20}Pt_{80}$ NWs in Ar-saturated 0.1 M $HClO_4$ with a scan rate of 50 mV/s which exhibit strong peaks associated with hydrogen underpotential formation/stripping below 0.4 V and Pt oxidization/reduction above 0.6 V. Figure 3.2.6B shows a typical ORR polarization curve of the $Fe_{20}Pt_{80}$ NWs obtained at room temperature in 0.1 M O_2-saturated $HClO_4$ at a scan rate of 20 mV/s and a rotating disk electrode (RDE)'s rotation speed of 1600 rpm. The electrochemical reduction reaches the diffusion limit below 0.8 V and a mixed kinetic diffusion control region is between 0.8 and 1.0 V. The ORR kinetic current can be calculated from the polarization curve according to

Levich-Koutecky equation[16] $1/i = 1/i_k + 1/i_d$ by using mass-transport correction and normalizing to ECASA from the CV and Pt mass amount. CoPt NWs were studied according to the same procedure. The corresponding CVs and ORR polarization curves are shown in Figure 3.2.7. Their electrocatalytic behavior was compared with the commercial BASF 3.2 nm Pt catalyst supported on carbon (C-Pt, 46% loading). Figure 3.2.6C shows the Tafel plots, which indicate the specific activities (j_k, kinetic current density) as a function of electrode potential, and a comparison of the specific activities of $Fe_{20}Pt_{80}$ NWs, Co_8Pt_{92} NWs, and commercial Pt catalysts at 0.9 Vand 0.95 V (vs. RHE) is given in Figure 3.2.6D. The specific activity of $Fe_{20}Pt_{80}$ NWs reaches 1.53 mA/cm^2 at 0.9 V and 0.20 mA/cm^2 at 0.95 V, which is twice of Co_8Pt_{92} NWs (0.64 mA/cm^2 at 0.9 V and 0.11 mA/cm^2 at 0.95 V) and around three to five times of Pt catalyst (0.32 mA/cm^2 at 0.9 V and 0.08 mA/cm^2 at 0.95 V). The Co_8Pt_{92} NWs have a lower activity than $Fe_{20}Pt_{80}$ in catalyzing ORR due to the large amount loss of Co from CoPt NWs compared to that of Fe in the acid solution.

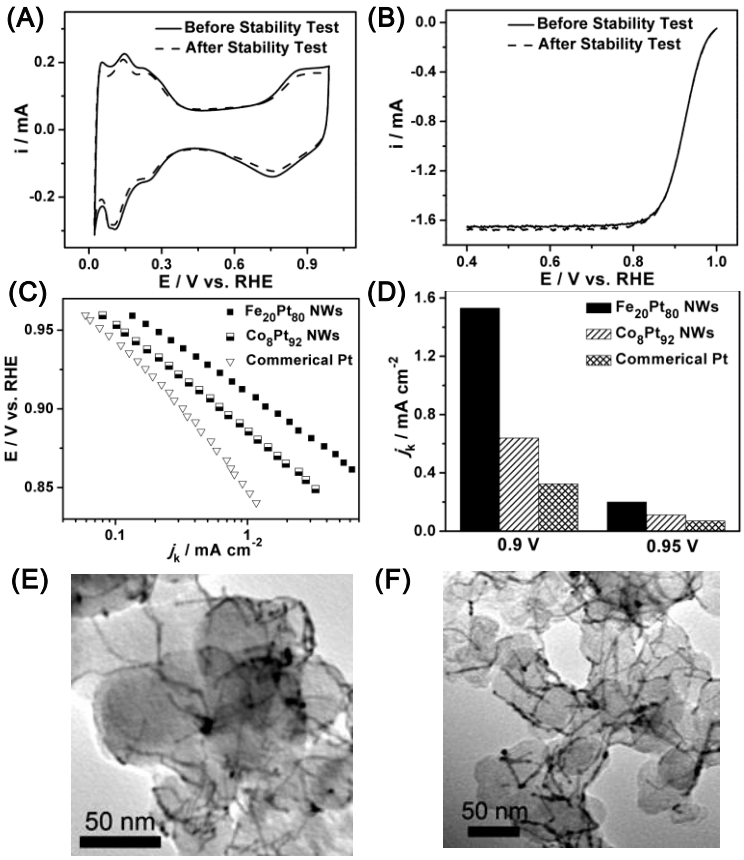

Figure 3.2.6 (A) CVs and (B) polarization curves of the $Fe_{20}Pt_{80}$ NWs before and after 4000 potential cycles between 0.6–1.0 V vs. RHE. (C) Specific ORR activities of different catalysts with the rotating disk electrode (RDE) rotation rate at 1600 rpm (Tafel plot), and (D) Specific ORR activities of different catalysts at 0.9 V and 0.95 V vs. RHE. TEM images of the C-$Fe_{20}Pt_{80}$ NWs before (E) and after (F) stability test.

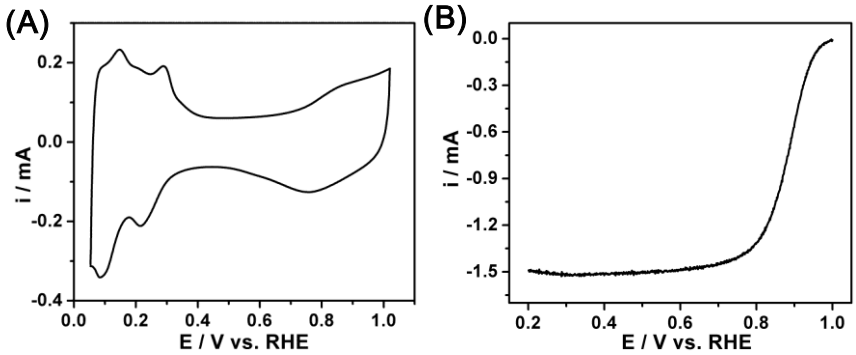

Figure 3.2.7 (A) CVs and (B) polarization curves of the Co_8Pt_{92} NWs in $HClO_4$.

The stability test on $Fe_{20}Pt_{80}$ NWs was obtained by cycling the scan between the potential 0.6 and 1 V (vs. RHE) in O_2-saturated 0.1 M $HClO_4$ at a scan rate of 100 mV/s. Figure 3.2.6A-B shows the CVs and ORR polarization curves of the $Fe_{20}Pt_{80}$ NWs after 4000 potential cycles. Only small portion of the initial ECASA for the $Fe_{20}Pt_{80}$ NWs is lost. The ORR polarization curves befor and after the stability test overlap. The final composition of FePt NWs is changed to $Fe_{16}Pt_{84}$, indicating only small amount of Fe is lost from the NWs' system after long time cycli ng. No obvious morphology change for FePt NWs was observed (Figure 3.2.6 E-F). The similar stability was also achieved in CoPt NWs' system (Figure 3.2.8 A-B).

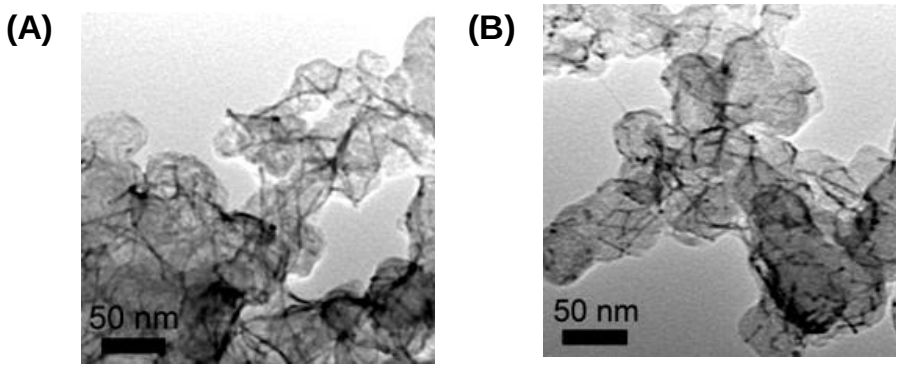

Figure 3.2.8. TEM images of C-Co_8Pt_{92} NWs before (A) and after stability test (B).

3.4 Conclusion

In summary, we have developed a facile process to synthesize FePt and CoPt NWs by thermal decomposition of $Fe(CO)_5$ or $Co_2(CO)_8$ and reduction of $Pt(acac)_2$ in a solution of ODE and OAm containing sodium oleate. By controlling the molar ratio of $Fe(CO)_5$ or $Co_2(CO)_8$ to $Pt(acac)_2$, the FePt (or CoPt) NW composition can be readily tuned. These NWs were first loaded on commercial carbon and treated with acetic acid to remove surfactant. The C-MPt NWs were found to be highly efficient in catalyzing ORR. With FePt NWs show largly improved acitivity and durability than commercial Pt NPs. This enhancement in ORR catalysis arises very likely from the Pt topmost atoms arranged along a long NW facet, as well as from the strong interaction between the NWs and the carbon support, which hinders NW dissolution, Ostwald ripening and aggregation. CoPt NWs show improved acitivity as well. But we should note that the Co effect may not be well presented here due to the large amount loss of Co. These NWs represent a new class active and durable catalyst for ORR and other catalytic applications.

Reference

1. V. R. Stamenkovic, B. S. Mun, K. J. J. Mayrhofer, P. N. Ross, N. M. Markovic, J. Rossmeisl, J. Greeley, J. K. Norskov, *Angew. Chem. Int. Ed*. **2006**, *45*, 2897-2901.

2. V. R. Stamenkovic, B. S. Mun, M. Arenz, K. J. J. Mayrhofer, C. A. Lucas, G. Wang, P. N. Ross, N. M. Markovic, *Nat. Mater*. **2007**, *6*, 241-247.

3. C. Wang, M. Chi, D. Li, D. van der Vliet, G. Wang, Q. Lin, J. F. Mitchell, K. L. More, N. M. Markovic, V. R. Stamenkovic, *ACS Catal.* **2011**, *1*, 1355-1359.

4. P. Strasser, S. Koh, T. Anniyev, J. Greeley, K. L. More, C. Yu, Z. Liu, S. Kaya, D. Nordlund, H. Ogasawara, M. F. Toney, A. Nilsson. *Nat. Chem.* **2010**, *2*, 454-460.

5. J.Wu, J. Zhang, Z. Peng, S. Yang, F. T.Wagner, H. Yang, *J. Am. Chem. Soc*. **2010**, *132*, 4984 – 4985;

6. J. Wu, L.Qi, H. You, A. M. Gross, J. Li, H. Yang, *J. Am. Chem. Soc.* **2012**, *134*, 11880 – 11883;

7. J. Kim, Y. Lee, S. Sun, *J. Am. Chem. Soc*. **2010**, *132*, 4996 – 4997;

8. J. Wu, A. Gross, H. Yang, *Nano Lett.* **2011**, *11*, 798 – 802.

9. C. Wang, D. van der Vliet, K.-C. Chang, H. You, D. Strmcnik, J. A. Schlueter, N. M. Markovic, V. R. Stamenkovic, *J. Phys. Chem. C* **2009**, *113*, 19365-19368.

10. S. Sun, G. Zhang, D. Geng, Y. Chen, R. Li, M. Cai, X. Sun, *Angew. Chem. Int. Ed.* **2011**, *50*, 422 – 426.

11. C. Koenigsmann, A. C. Santulli, K. Gong, M. B. Vukmirovic,W.-P. Zhou, E.Sutter, S. S. Wong, R. R. Adzic, *J. Am. Chem. Soc.* **2011**, *133*, 9783 – 9795.

12. C.Wang, Y. Hou, J. Kim, S. Sun, *Angew. Chem. Int. Ed.* **2007**, *46*, 6333 – 6335.

13. S. Sun, C. B. Murray, D. Weller, L. Folks, A. Moser, *Science* **2000**, *287*, 1989 – 1992

14. V. Mazumder, S. Sun, *J. Am. Chem. Soc.* **2009**, *131*, 4588 –4589

15. B. Lim, M. Jiang, P. H. C. Camargo, E. C. Cho, J. Tao, X. Lu, Y. Zhu, Y. Xia, *Science* **2009**, *324*, 1302-1305.

16. T. J. Schmidt, H. A. Gasteiger, Rotating thin-film method for supported catalysts, in: W. Vielstich, H. Gasteiger, A. Lamm (Eds.), Handbook of Fuel Cells-Fundamentals, Technology and Applications, **2003**, *2*, 316-333.

Chapter 4

Synthetic Control of FePtM Nanorods (M = Cu, Ni) to Enhance Oxygen Reduction Reaction

4.1 Background and Introduction

As we introduced in Chapter 1 and Chapter 3, developing highly efficient catalyst for oxygen reduction reaction (ORR) is key to fabrication of commercially viable fuel cell devices and metal-air batteries for future energy applications.[1-3] Recent search for advanced catalysts for ORR has led to some exciting advances in understanding the catalytic nature, allowing more rational tuning of catalytic properties via controlled syntheses. For example, when Pt is alloyed with early transition metal, such as Fe, Co, Ni, its d-band center is down-shifted and its bonding to oxygenated species is weakened, leading to the increase in catalytic activity for ORR.[3-5] More interestingly, when Pt is present as a thin shell in a core/shell structure, both its activity and durability are greatly enhanced due to the simultaneous down-shift of its d-band center and surface strain induced in the Pt shell, which is favorable for O_2 adsorption and activation.[6-8] Pt catalysis for ORR can be further activated when Pt catalysts are prepared in a controlled shape,[9-10] especially in one dimensional (1-D) nanostructure,[8-9] where interactions between a crystal facet and oxygenated species as well as carbon support can be optimized to achieve high catalytic activity with increased catalyst stability. These previous studies indicate that a 1-D core/shell nanostructure with Pt on shell can combine both alloy and shape effects to enhance ORR catalysis. Therefore a controlled synthesis of core/shell 1-D nanostructure may provide a new approach to highly efficient Pt catalyst for ORR. Recently, we prepared FePt, CoPt and FePtPd nanowires (NWs) and studied their catalysis for ORR.[11-12] We found that adding Pd to FePt NWs destabilized the catalyst without obvious activity gain. Conversely, these ternary NWs elevated the activity of methanol oxidation reaction.[11] Without the presence of Pd, the FePt and CoPt NWs

were more active and durable for ORR than the polyhedral NP catalysts as illustrated in Chapter 3.[12] However, upon acetic acid treatment to remove surfactant coating and to activate NW catalyst, a majority of M in MPt NWs was etched away, minimizing the M-effect on the enhancement of Pt catalysis. To fully realize the M-alloy benefits in catalysis, it is necessary to develop a 1-D nanostructure with M being preserved in acid solution. With this in mind, we developed a controlled synthesis of 20 nm x 2 nm nanorods (NRs) of FePtM (M = Cu, Ni) and studied their acid stability. We found that these thin FePtM NRs, especially FePtCu NRs, were much more stable in acid solution. When treated with acetic acid and etched electrochemically in 0.1 M $HClO_4$, these ternary alloy NRs were converted into core/shell FePtM/Pt NRs with Fe and M (especially Cu) being preserved in the core NRs, as illustrated in Figure 4.1 These core/shell NRs combine 1-D shape and core/shell effects on catalysis and show indeed much higher activity and durability for ORR.

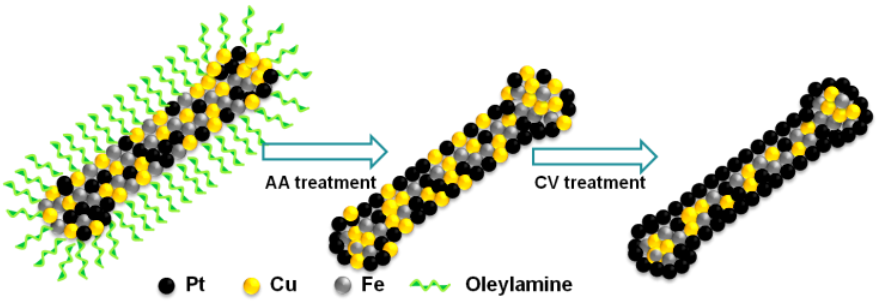

Figure 4.1 Schematic illustration of formation and activation of core/shell-type NR catalyst.

4.2 Experimental

Chemicals and Materials

Sodium oleate (Na-oleate), oleylamine (OAm, >70%), oleic acid (OA), 1-octadecene (ODE), $Pt(acac)_2$ (acac = aceylacetonate), $Cu(acac)_2$, $Ni(acac)_2$, iron pentacarbonyl ($Fe(CO)_5$), hexane, isopropanol, ethanol, acetic acid (99%) and Nafion (5%) were all purchased from Sigma Aldrich. C-Pt (20% mass loading with a diameter of 2.5-3.5 nm) catalyst was obtained from Fuel Cell Store.

Characterization

TEM images were obtained from a Philips CM 20 operating at 200 kV. High-resolution TEM (HRTEM) images were obtained from a JEOL 2010 with an accerating votalage of 200 kV. TEM and HRTEM samples were prepared by depositing a single drop of diluted nanorod (NR) dispersion in hexane on amorphous carbon coated copper grids. The inductively coupled plasma-atomic emission spectroscopy (ICP-AES) measurements were carried on a JY2000 Ultrace ICP Atomic Emission Spectrometer equipped with a JY AS 421 autosampler and 2400g/mm holographic grating. Electrochemical measurements were performed on a Fuel Cell Electrocatalyst RDE bundle from PINE Instrument Company with a model AFCBP1 with a three-electrode system consisting of a glassy carbon (GC) working electrode (5-mm in diameter), an Ag/AgCl reference electrode (10% KNO_3), and a platinum wire counter electrode.

Synthesis of FePtM (M=Cu, Ni) NRs

A mixture solution of sodium oleate (0.3g) and ODE (12 mL) in a four-necked

flask was heated to 200 °C under nitrogen flow and magnetic stirring to make sodium oleate dissolved thoroughly. Then the solution was cooled down to room temperature and a mixture of $Pt(acac)_2$ (98 mg) and OAm (8 mL) was added into the solution and heated to 120 °C. Under the blanket of nitrogen, $Fe(CO)_5$ (0.03 mL) was added into the solution that was then further heated to 160 °C. At this temperature, a mixture of $Cu(acac)_2$ (32 mg) and OAm (3 mL) was added into the solution followed by heating to 240 °C and keeping at this temperature for 1 h. After cooled down to room temperature, the FePtCu NRs were collected and washed by addition of isopropanol (20 mL) and subsequent centrifugation at 8500 rpm for 8 min. The product was redispersed into hexane and precipitated out by addition of ethanol and centrifugation to remove all residual impurities. Final product was FePtCu NRs and was dispersed in hexane for further use. Under the identical condition, by changing $Cu(acac)_2$ to $Ni(acac)_2$, FePtNi NRs were prepared. Different composition was obtained by varying the amount of $Cu(acac)_2$ or $Ni(acac)_2$ at a fixed ratio between $Fe(CO)_5$ and $Pt(acac)_2$, as summerized in Table 4.1.

Synthesis of FePtCu NWs

The synthetic procedure of FePtCu NWs was samilar to that of NRs except 0.07ml of $Fe(CO)_5$ was added at 120 °C.

Synthesis of FePt NRs

Similar to the synthesis of FePtCu NRs, FePt NRs were obtained by direct injection of $Fe(CO)_5$ and by heating the mixture to 240 ºC for 60 min at the heating

rate of about 4-5 ºC/min without the presence of $Cu(acac)_2$.

Catalyst Preparation

The as-synthesized NRs and Ketjen-300 J carbon at the weight ratio of 4:6 were mixed in 20 mL mixture of hexane and acetone (V/V=1/1) and sonicated for 1 h to deposit NRs on carbon. The product was separated from teh solvent by centrifugation and was suspended in 30 ml acetic acid at 70 ºC for overnight to remove the surfactant. The resultant solid product was separated from the acid by centrifugation and washed with ethanol and deionized water. The product was then redispersed in a mixture of deionized water, isopropanol and Nafion (V/V/V = 4/1/0.05). 20 µL catalyst ink was deposited on the working electrode (glassy carbon rotating disk electrode, GC-RDE) that was polished prior to catalyst deposition by 0.1 µm and 0.05 µm alumina powder and rinsed by sonication in ethanol and in deionized water. The catalyst was dried at ambient condition.

Electrochemical Measurements

Cyclic voltammograms (CVs) were obtained by scaning between -0.2 V-1.0 V *vs* Ag/AgCl at a scan rate of 50 mV/s in N_2-saturated 0.1M $HClO_4$. ORR polarization curves were obtained by scaning the potentials from 1.0 to -0.2 V *vs* Ag/AgCl at a scan rate of 10 mV/s in O_2-saturated 0.1 M $HClO_4$ with the GC-RDE rotating at 1600 rpm.

4.3 Results and Disscusion

4.3.1 Synthesis of FePtM (M=Cu, Ni) Nanorods (NRs)

FePtM (M = Cu, Ni) NRs were synthesized by the thermal decomposition of iron pentacarbonyl ($Fe(CO)_5$) and the reduction of metal acetylacetonates ($Pt(acac)_2$ and $Cu(acac)_2$ or $Ni(acac)_2$) (see **Experimental**).[12] The oleylamine (OAm) and sodium oleate (sodium-oleate) were used to control NR growth and stabilization, while the mixture of oleylamine and octadecene (v/v = 2/3) served as the solvent. In the synthesis, the composition of ternary NRs was controlled by the precursor ratios. Transmission electron microscopy (TEM) images show that the as-synthesized FePtM (M = Cu, Ni) NRs in different compositions had the same morphology with average length in 20 ± 2 nm and diameter in 2 ± 0.2 nm (Figure 4.2.1).Inductively coupled plasma-atomic emission spectroscopy (ICP-AES) analyses indicated that the Cu/Pt or Ni/Pt in the as-synthesized NRs was linearly proportional to the ratio of $Cu(acac)_2/Pt(acac)_2$ (Table 4.2.1). The $Fe_{51}Pt_{49}$ NRs were also made without the addition of $Cu(acac)_2$ and $Ni(acac)_2$ (Figure 4.2.2) and were used as a control. Figure 4.2.3 shows HRTEM image of the representative $Fe_{29}Pt_{41}Cu_{30}$ NRs, within which the adjacent lattice spacing was measure to be 0.22 nm, corresponding to the (111) interplanar distance of face centered cubic (fcc) FePtCu. The lattice fringe points away from the NR growth direction by approximately 55º, indicating that the NRs grow along the [100] direction, in consistent to that observed in the growth of FePt and FePtPd NWs.[11-13] These FePt and FePtM (M = Cu, Ni) NRs show typical fcc

structures, as indicated by XRD patterns in Figure 4.2.4.

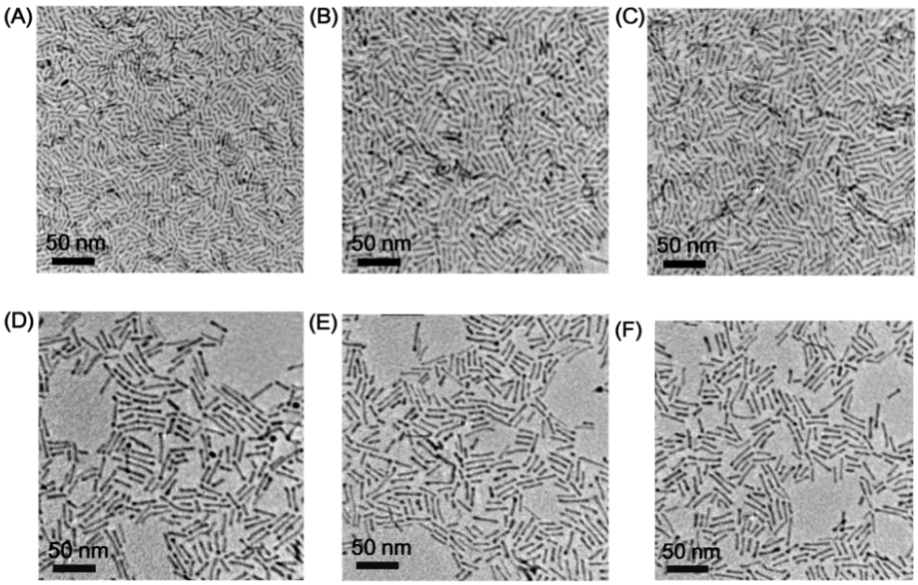

Figure 4.2.1 TEM images of (A) $Fe_{42}Pt_{44}Cu_{14}$, (B) $Fe_{38}Pt_{42}Cu_{20}$, (C) $Fe_{29}Pt_{41}Cu_{30}$, (D) $Fe_{43}Pt_{45}Ni_{12,}$ (E) $Fe_{35}Pt_{44}Ni_{21}$, and (F) $Fe_{31}Pt_{37}Ni_{32}$ NRs.

Precursor Fe:Pt:Cu	4:4:1	2:2:1	4:4:3
Final composition	$Fe_{42}Pt_{44}Cu_{14}$	$Fe_{38}Pt_{42}Cu_{20}$	$Fe_{29}Pt_{41}Cu_{30}$
Precursor Fe:Pt:Ni	4:4:1	2:2:1	4:4:3
Final composition	$Fe_{43}Pt_{45}Ni_{12}$	$Fe_{35}Pt_{44}Ni_{21}$	$Fe_{31}Pt_{37}Ni_{32}$

Table 4.1 Composition control of FePtCu and FePtNi NRs by varying the precursor ratio.

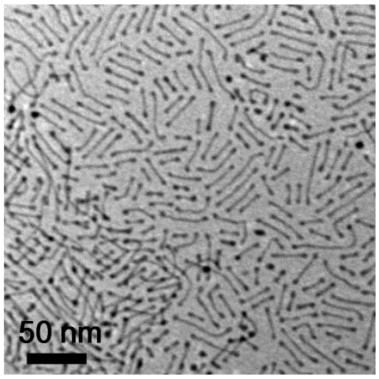

Figure 4.2.2 TEM image of the $Fe_{51}Pt_{49}$ NRs.

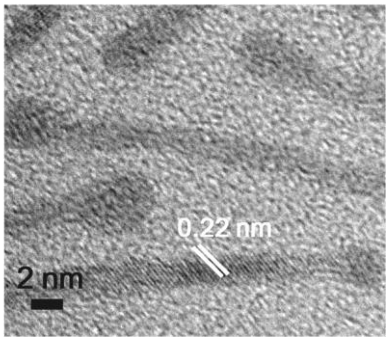

Figure 4.2.3 HRTEM image of $Fe_{29}Pt_{41}Cu_{30}$ NRs.

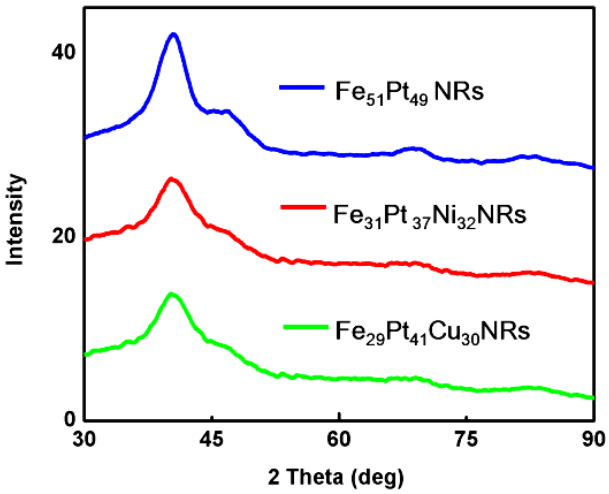

Figure 4.2.4 XRD patterns of FePt, FePtCu and FePtNi NRs.

Under the current synthetic condition, the 1-D FePt NRs were first formed before Cu- or Ni-precursor was added at 160 ºC (Figure 4.2.5). It looks that the FePt NRs served as the template and Cu/Ni was incorporated into the NR structure via intermetallic diffusion. The presence of $Fe(CO)_5$ and the formation of FePt was the key to the formation of ternary NRs. Without $Fe(CO)_5$, only irregular CuPt (or NiPt) NPs were produced. If the FePtM NRs were prepared when Fe- and Pt-precursor were in equal amount at 0.25 mmol each, the addition of Cu/Ni-precursors had no effect on the FePt formation as the Fe/Pt ratios in FePt and FePtM NRs were nearly the same. When the precursor Fe/Pt ratio was increased to 2 (0.5 mmol/0.25 mmol), the Fe/Pt ratio remained to be 1 (Figure 4.2.6). Here, Cu- or Ni-salts were mainly reduced by $Fe(CO)_5$ when the excess of $Fe(CO)_5$ was present. But with both $Fe(CO)_5$ and $Pt(acac)_2$ at 0.25 mmol, Cu- or Ni-salts tended to be reduced by oleylamine. The subsequent high-temperature (240 ºC) aging promoted the atomic diffusion, producing ternary alloy NRs. We should note that although the excess of $Fe(CO)_5$ had no obvious effect on the final NR composition, it did help to control the length of NRs. For example, a precursor ratio of Fe:Pt = 2:1 led to the formation of 60 nm x 2 nm NWs (Figure 4.2.6).

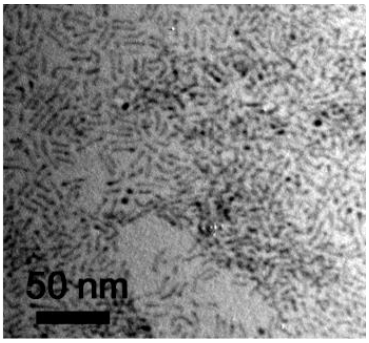

Figure 4.2.5 TEM image of the sample separated from the 160 ºC solution in the syntehsis of FePtCu NRs before $Cu(acac)_2$ was added.

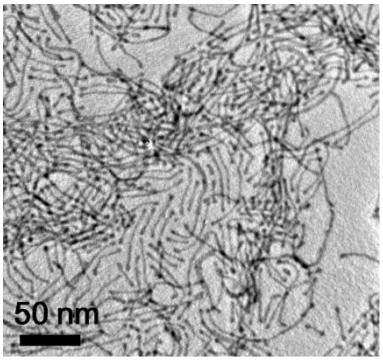

Figure 4.2.6 TEM image of the $Fe_{38}Pt_{40}Cu_{22}$ NWs.

4.3.2 Electrochemical dealloying of FePtM NRs

The as-synthesized 20 x 2 nm NRs were loaded on Ketjen carbon support (C) as reported.[14-15] The C-NRs were washed with acetic acid (AA) at 70 ºC to remove oleate/oleylamine coating.[16] ICP-AES analyses showed that this acid treatment led to partial loss of Fe and Ni in all NRs, but negligible loss of Cu in FePtCu NRs (Table 4.2.2**)**, indicating Cu is more acid resistant than Fe and Ni. After the washing step, the

C-NRs (or commercial C-Pt NPs, 20% mass loading with Pt particle diameter of 2.5-3.5 nm) were suspended in deionized water + isopropanol + 5% Nafion (v/v/v = 4/1/0.05) forming a suspension of 2 mg catalyst/mL. 20 μL of the suspension was deposited on the glassy carbon (GC) surface of a rotating disk electrode (RDE) and dried at ambient environment. The C-NRs deposited on GC-RDE were subject to further CV scanning from -0.2 V to 1.0 V in N_2-saturated 0.1 M $HClO_4$ for "Cu dealloying".[17] Figure 4.2.7 is the CV curves of the 10^{th} and 60^{th} potential cycles. We can see that the CV of the 60^{th} cycle shows a sharper hydrogen underpotential formation/stripping peak in the range of -0.2 to 0.15 V and a positive shift of the reduction peak related to Pt-oxygenated species, suggesting the Cu depletion of the near surface region and the formation of a Pt-enrichment shell.[17-20] After these CV scans, the NR composition was changed from $Fe_{12}Pt_{54}Cu_{34}$ to $Fe_{10}Pt_{75}Cu_{15}$. The core/shell FePtCu/Pt NRs were characterized by atomically resolved aberration-corrected scanning transmission electron microscopy (STEM) and STEM-electron energy loss spectroscopy (STEM-EELS). Figure 4.2.8 show the high-angle annular dark field (HAADF) image of the NRs after 60 CV cyclings (Inset) and the related EELS line scan, confirming the formation of a thin Pt-shell after surface dealloying.

Before AA wash	$Fe_{42}Pt_{44}Cu_{14}$	$Fe_{38}Pt_{42}Cu_{20}$	$Fe_{29}Pt_{41}Cu_{30}$
After AA wash	$Fe_{25}Pt_{58}Cu_{17}$	$Fe_{21}Pt_{54}Cu_{25}$	$Fe_{12}Pt_{54}Cu_{34}$
Before AA wash	$Fe_{43}Pt_{45}Ni_{12}$	$Fe_{35}Pt_{44}Ni_{21}$	$Fe_{31}Pt_{37}Ni_{32}$
After AA wash	$Fe_{24}Pt_{69}Ni_{7}$	$Fe_{20}Pt_{67}Ni_{13}$	$Fe_{20}Pt_{64}Ni_{16}$

Table 4.2 Composition change of FePtCu and FePtNi NRs before and after acetic acid wash.

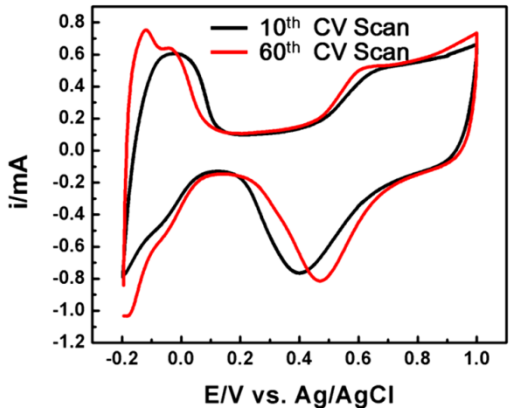

Figure 4.2.7 CVs at the beginning and at the end of the electrochemical etching process. The potentials were from -0.2 V to 1.0 V at a scan rate of 100 mV/s in N_2-saturated 0.1 M $HClO_4$.

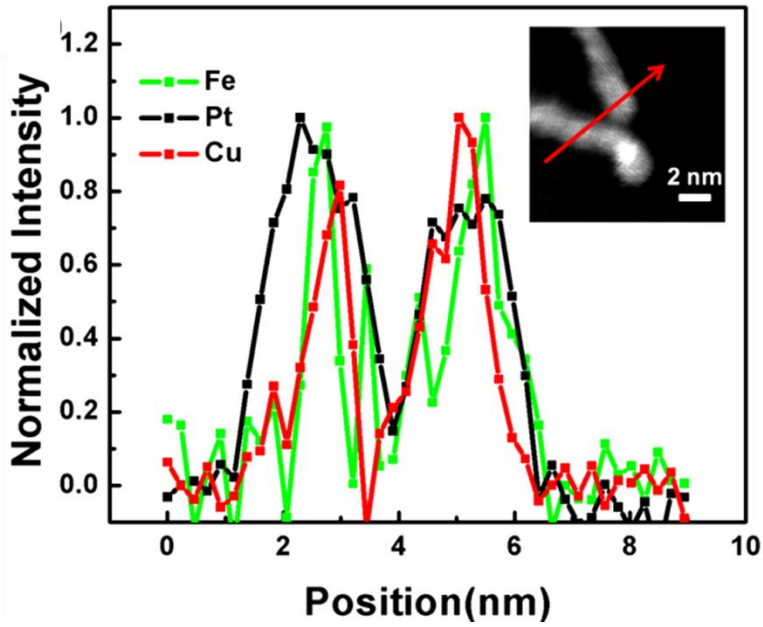

Figure 4.2.8 STEM-HAADF image (**Inset**) and STEM-EELS line scan of the representative $Fe_{10}Pt_{75}Cu_{15}$ NRs obtained after the CV-cycling of $Fe_{29}Pt_{41}Cu_{30}$ NRs.

4.3.3 Catalytic Properties of FePtM (M=Cu, Ni) NWs

Figure 4.2.9A shows the CVs of the core/shell NRs (from $Fe_{29}Pt_{41}Cu_{30}$ NRs) and C-Pt in N_2-saturated 0.1 M $HClO_4$. The peaks in the range of -0.2 to 0.15 V are from the common hydrogen underpotential formation/stripping and are used to estimate the electrochemically active surface area (ECASA) of the catalyst.[21] The metal oxidation/reduction peaks appear in the range of 0.4-0.9 V. The composition-dependent ORR activity of the FePtCu NRs was studied. Figure 4.2.9B shows the ORR polarization curves of the core/shell NRs of FePtCu NRs and commercial Pt NPs in O_2-saturated 0.1 M $HClO_4$. The ORR polarization curves depict the diffusion-limiting current region ranging from −0.05 to 0.4 V and the

mixed kinetic−diffusion control region between ~0.4 and ~0.7 V. With the increase in Cu, the half-wave potential of the FePtCu NRs shifts positively, indicating that the NRs with the initial composition of $Fe_{29}Pt_{41}Cu_{30}$ (0.557 V) have a better catalytic activity towards ORR than $Fe_{38}Pt_{42}Cu_{20}$ (0.551 V), $Fe_{42}Pt_{44}Cu_{14}$ (0.537 V) and $Fe_{51}Pt_{49}$ NRs (0.520 V) at the same NR loading by weight. The ORR activity of the $Fe_{10}Pt_{75}Cu_{15}$ NRs was compared with the C-Pt NPs (Figure 4.2.9C). The ORR half potential from the $Fe_{10}Pt_{75}Cu_{15}$ NRs is 45 mV more positive than that of the C-Pt catalyst (0.512 V). The $Fe_{10}Pt_{75}Cu_{15}$ NRs have a mass activity (MA) of 1.034 A/mgPt and a specific activity (SA) of 1.369 mA/cm^2 at 512 mV (*vs* Ag/AgCl), which is 7 and 5 times higher than that of the commercial C-Pt (0.138A/mg_{Pt} and 0.271 mA/cm^2). At 557 mV, the $Fe_{10}Pt_{75}Cu_{15}$ NRs have an MA of 0.222 A/mg_{Pt} and a SA of 0.299 mA/cm^2, while the commercial C-Pt shows only 0.035 A/mg_{Pt} and 0.068 mA/cm^2.

Durability of the core/shell NR catalyst was tested by cycling potentials between 0.4-0.8 V (vs. Ag/AgCl) at a sweep rate of 100 mV/s in O_2-saturated 0.1 M $HClO_4$. The CVs (Figure 4.2.9D) and polarization curves (Figure 4.2.9E) of the $Fe_{10}Pt_{75}Cu_{15}$ NRs before and after 5000 potential cycles nearly overlap. Correspondingly, the core/shell NRs show no obvious morphology and composition change before and after the durability test, as demonstrated by their TEM image (Figure 4.2.9F**)** and their slight composition drop in Fe/Cu from $Fe_{10}Pt_{75}Cu_{15}$ to $Fe_8Pt_{78}Cu_{14}$. These

suggest that the FePtCu/Pt core/shell NRs are highly stable in the current ORR condition.

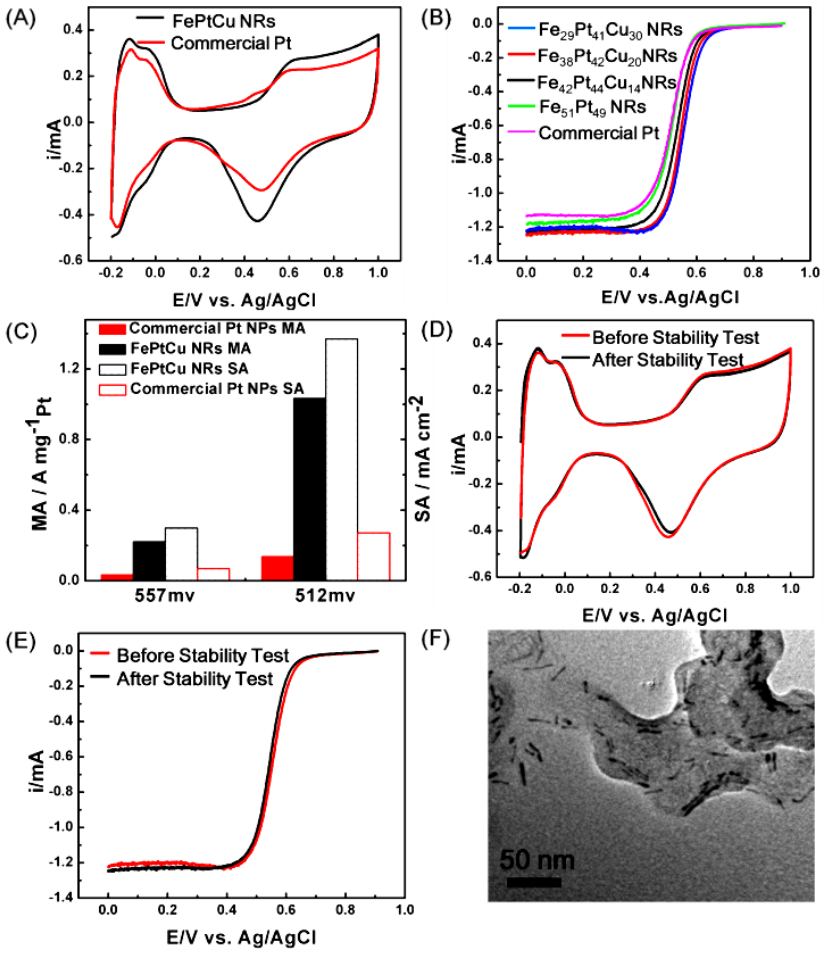

Figure 4.2.9 (A) CVs of the C-$Fe_{10}Pt_{75}Cu_{15}$ NRs and C-Pt NPs in N_2-saturated 0.1 M $HClO_4$ at a scan rate of 50 mV/s. (B) Polarization curves of the FePtCu NRs with different initial compositions and commercial Pt NPs in O_2-saturated 0.1 M $HClO_4$ at 295 K. **(C)** ORR mass activity (MA) and specific activity (SA) of $Fe_{10}Pt_{75}Cu_{15}$ NRs and commercial Pt NPs. (D) CVs of $Fe_{10}Pt_{75}Cu_{15}$ NRs in N_2-saturated 0.1 M $HClO_4$ before and after 5000 potential cycles between 0.4-0.8 V in O_2-saturated 0.1 M

$HClO_4$. (E) Polarization curves of the $Fe_{10}Pt_{75}Cu_{15}$ NRs in O_2-saturated 0.1 M $HClO_4$ at 295 K before and after 5000 potential cycles between 0.4-0.8 V in O_2-saturated 0.1 M $HClO_4$. (F) TEM image of the $Fe_{10}Pt_{75}Cu_{15}$ NRs on carbon support after 5000 cycles of stability test.

The FePtNi NRs also displayed composition-dependent ORR activities (Figure 4.2.10). More 3d transition metal (FeNi) present in FePtNi NRs led to higher activity. However, after the acetic acid treatment, a substantial amount of Ni was lost (Table 4.2.2). Therefore, FePtNi NRs were less stable in acid and less active for catalyzing ORR than FePtCu NRs.

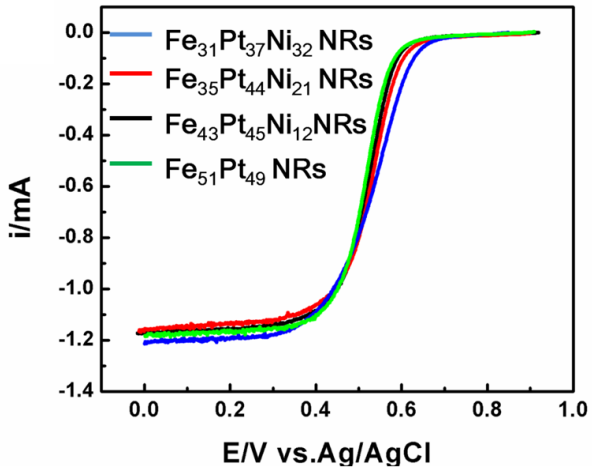

Figure 4.2.10 Polarization curves of the FePtNi and FePt NRs with different initial composition in O_2-saturated 0.1 M $HClO_4$ at 295 K.

4.4 Conclusion

In summary, we have developed a facile solution-phase process to synthesize ternary alloy FePtM (M = Cu, Ni) NRs with their dimension controlled to be 20 x 2 nm and their compositions tuned by the precursor ratios. These NRs are more stable in acid than their binary counterparts. When treated with acetic acid and electrochemical etching in 0.1 M $HClO_4$, these ternary alloy NRs are converted into core/shell structured FePtM/Pt NRs. These core/shell NRs, especially FePtCu/Pt NRs, are a new class of ORR catalyst superior to their binary counterparts and the commercial Pt catalyst. The core/shell NRs obtained from the $Fe_{29}Pt_{41}Cu_{30}$ alloy NRs show much enhanced durability and have the mass and specific activities that are 7- and 5-fold higher than the commercial Pt NP catalyst. Our controlled synthesis of core/shell 1-D nanostructure provides a new approach to highly efficient Pt catalyst for ORR. The same structure may also offer an alternative catalyst model to study electronic and strain effect for tuning NP catalysis for other chemical reactions.

Reference

1. J. Zhang, PEM Fuel Cell Electrocatalysts and Catalysts Layers Fundamentals and Application. Springer **2008**.
2. C. Wang, H. Daimon, T. Onodera, T. Koda, S. Sun, *Angew. Chem. Int. Ed.* **2008**, *47*, 3588-3591.
3. H. Lee, S. E. Habas, S. Kweskin, D. Butcher, G. A. Somorjai, P. Yang, *Angew. Chem., Int. Ed*. **2006**, *45*, 7824-7828.
4. (a) V. A. Sethuraman, J. W. Weidner, A. T. Haug, S. Motupally, L.V. Protsailo, *J. Electrochem. Soc.* **2008**, *155*, B50-B57. (b) R. R. Adz, J. X. Wang, *J. Phys. Chem. B.***1998**, *102*, 8988-8993.(c) B. N. Wanjala, B. Fang, J. Luo, Y. Chen, J. Yin, M. H. Engelhard, R. Loukrakpam, C. J. Zhong, *J. Am. Chem. Soc.* **2011**, *133*, 12714-12727.
5. V. R. Stamenkovic, B. S. Mun, M. Arenz, K. J. J. Mayrhofer, C. A. Lucas, G. Wang, P. N. Ross, N. M. Markovic, *Nat. Mater.* **2007**, *6*, 241-247.
6. V. Mazumder, M. Chi, K. L. More, S. Sun, *J. Am. Chem. Soc.* **2010**, *5*, 7848-7849.
7. C. Wang, D. Vliet, K. More, N. Zaluzec, S. Peng, S. Sun, H. Daimon, G. Wang, J. Greeley, J. Pearson, A. Paulikas, G. Karapetrov, D. Strmcnik, N. M. Markovic, V. R. Stamenkovic, *Nano Lett.* **2011**, *11*, 919-926.
8. (a) C. Cui, S. Yu, *Acc. Chem. Res.* **2013,** 46, DOI: 10. 1021/ar300254b. (b)C. Cui, H. Li, J. Yu, M. Gao, S. Yu, *Angew. Chem. Int. Ed.* **2010**, 49, 9149-9152. (c) H.

Li, C. Cui, S. Zhao, H. Yao, M. Gao, F. Fan, S. Yu, *Adv. Energy. Mater*. **2012**, 2, 1182-1187. (d) C. Koenigsmann, A. C. Santulli, K. Gong, M. B. Vukmirovic, W. Zhou, E. Sutter, S. S. Wong, *J. Am. Chem. Soc*. **2011**, *133*, 9783-9795.

9. H. Zhou, W. Zhou, R. R. Adzic, S. S. Wong, *J. Phys. Chem. C.* **2009**, *113*, 5460-5466.
10. S. Sun, G. Zhang, D. Geng, Y. Chen, R. Li, M. Cai, X. Sun, *Angew. Chem. Int. Ed.* **2011**, *50*, 422-426.
11. S. Guo, S. Zhang, X. Sun, S. Sun, *J. Am. Chem. Soc.* **2011**, *133*, 15354-15357.
12. S. Guo, D. Li, H. Zhu, S. Zhang, N. M. Markovic, V. R. Stamenkovic, *Angew. Chem. Int. Ed.* **2013**, *52*, 3465-3468.
13. C. Wang, Y. Hou, J. Kim, S. Sun. *Angew. Chem. Int. Ed.* **2007**, *46*, 6333-6335..
14. . Mazumder, S. Sun, *J. Am. Chem. Soc*. **2009**, *131*, 4588-4589.
15. S. Zhang, S. Guo, H. Zhu, D. Su, S. Sun, *J. Am. Chem. Soc*. **2012**, *134*, 5060-5063.
16. S. Guo, S. Sun, *J. Am. Chem. Soc.* **2012**, *134*, 2492-2495.
17. S. Koh, T. Anniyev, J. Greeley, K. More, C. Yu, Z. Liu, P. Strasser, *Nature Chem.* **2010**, *2*, 458-460.
18. C. Wang, M. Chi, D. Li, D. Strmcnik, G. Wang, V. Komanicky, N. M. Markovic, V. R. Stamenkovic, *J. Am. Chem. Soc.* **2011**, *133*, 14396-14403.
19. V. R. Stamenkovic, B. Fowler, B. S. Mun, G. Wang, P. N. Ross, C. A. Lucas, N. M. Markovic, *Science* **2007**, *315*, 493-497.

20. F. Maillard, L. Dubau, J. Durst, M. Chatenet, J. Andre, E. Rossinot, *Electrochem. Commun.* **2010**, *12*, 1161-1164.

21. J. Snyder, T. Fujita, M. W. Chen, J. Erlebacher, *Nat. Mater.* **2010**, *9*, 904−907.

Chapter 5

Surface Profile Control of FeNiPt/Pt Core/Shell Nanowires for Oxygen Reduction Reaction

5.1 Background and Introduction

The ever-increasing global energy demands require the search for renewable new energy scheme with low environmental impact. The sustainable new energy scheme, such as chemical-electrical conversion energy devices (fuel cells and metal-air batteries) is often limited by kinetically sluggish energy conversion reactions, especially the ubiquitous cathode reaction oxygen reduction reaction (ORR).[1-5] To date, extensive efforts have been put into controlling of Pt-based nanocatalysts' size, composition, shape and structure to enhance their performance in catalyzing ORR.[6-12] For example, core/shell nanoparticles (NPs) with Pt presenting in the shell and early transition metal components, such as Ni, Co and Fe presenting in the core combines both the electronic effect and strain effect together to improve their ORR performance.[10, 13, 14] Furthermore, recently 1-D nanowires (NWs) and nanorods (NRs) have been reported to show drastically improved activity and stability for ORR due to the strong interaction between 1-D nanostructure and the carbon support.[11, 15, 16] But our recent work in 1-D nanostructure ORR catalysts is centered on the composition and structure control with early transition component such as Fe, Co, Ni and Cu presenting on the surface as we introduced in Chapter 3-4. Subsequently, in the following acidic electrochemical environment, surface non-noble 3d transition metals were depleted, leaving a Pt-skeleton type of structure with a large number of low coordination sites for blocking species such as OH^- to attack[11, 15], thus limiting the catalyst's activity. Moreover, due to the strong interaction between Pt-O, these low

coordination sites are vulnerable to Pt migration and dissolution, resulting in a poor stability.[17-18] It can be envisioned that NPs with a smoother Pt-skin surface profile would potentially bring in an even more improved performance for ORR. Previous efforts to obtain smooth Pt-skin surface have been focused on acid etching and thermal annealing. Figure 5.1.1 illustrates previous method to obtain PtNi/multilayered Pt-skin structure.[19]

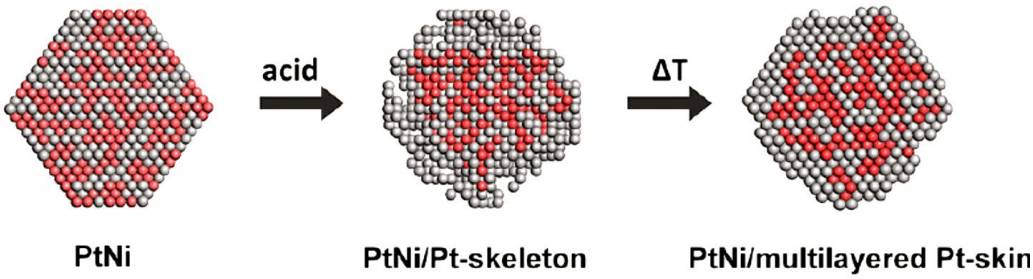

Figure 5.1.1 Schematic illustration of producing PtNi/multilayered Pt-skin structure through acid etching and thermal annealing.[19]

Similar, in order to improve our 1-D nanocatalysts' performance in ORR catalysis, our focus in this study is centred on tuning of surface profile of Pt-based nanocatalysts, which, for the first time, has been done in monodisperse NWs' regime. As shown in Figure 5.1.2, acid treatment was first applied to remove surface vulnerable early-transition metal component (Fe), leaving a Pt-skeleton surface. Further high temperature annealing promotes surface Pt atoms to rearrange into a multilayered skin structure.

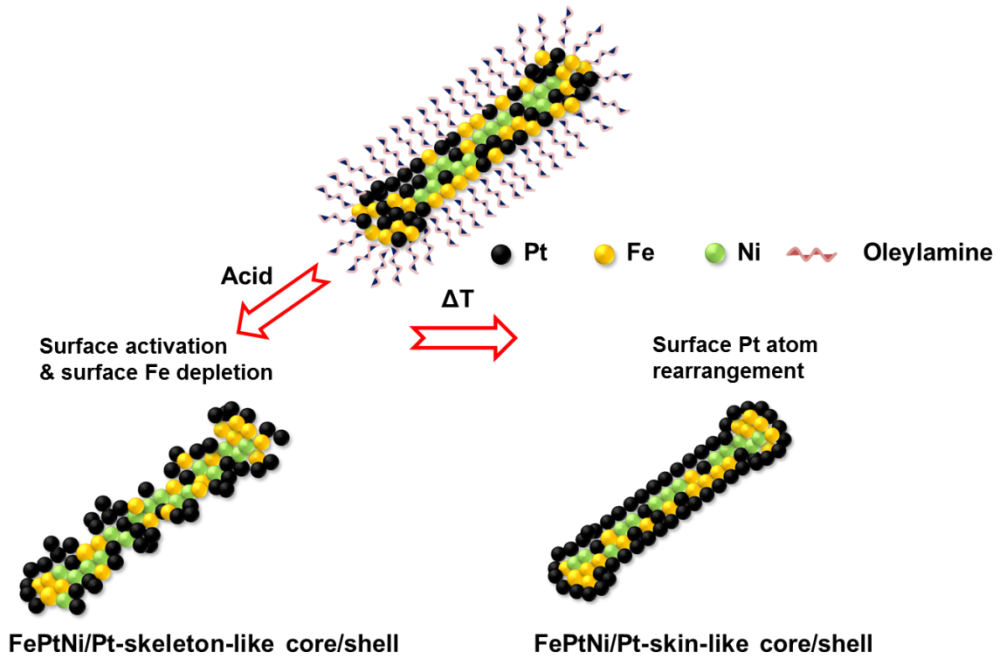

Figure 5.1.2 Schematic illustration of tailoring the NWs' surface profile through post-treatment.

5.2 Experimental

Chemicals and Materials

Oleylamine (OAm, >70%), oleic acid (OA), sodium oleate (Na-oleate), 1-octadecene (ODE), $Pt(acac)_2$ (acac = aceylacetonate), $Ni(acac)_2$, $Fe(CO)_5$, hexane, isopropanol, ethanol and Nafion (5%) were all purchased from Sigma Aldrich.

Characterization

TEM images were obtained from a Philips CM 20 operating at 200 kV. The inductively coupled plasma-atomic emission spectroscopy (ICP-AES) measurements were carried on a JY2000 Ultrace ICP atomic emission spectrometer equipped with a JY AS 421 autosampler and 2400g/mm holographic grating. X-ray diffraction (XRD)

characterization was carried out on a Bruker AXS D8-Advanced diffractometer with Cu Kα radiation (λ =1.5418 Å). HRTEM was performed on both JEOL 2100F (200 kV). STEM analyses were obtained on a Hitachi HD2700C (200 kV) with a probe aberration-correction in the Center for Functional Nanomaterial at Brookhaven National Laboratory. Electrochemical measurements were performed on a Autolab potentiostat from Metrohm Instrument Company (Autolab 302). A three-electrode system consisting of a glassy carbon (GC) working electrode (5-mm in diameter), an Ag/AgCl reference electrode (in 4 M KCl) and a platinum wire counter electrode was used for electrochemical study. All the potentials given were calibrated versus reversible hydrogen electrode (RHE).

Synthesis of FeNiPt NWs

0.2 sodium oleate (Na-oleate) was mixed with 12 mL 1-octandence (ODE) and heated to 180 ^{o}C under a continuous N_2 flow and magnetic stirring to form a homogenous clear solution. After cooled down to room temperature, 0.5 mmol $Pt(acac)_2$ and 8 mL oleylamine (OAm) was added into the solution. The system was heated to 120 ^{o}C and 0.5 mmol $Fe(CO)_5$ was added into the solution under a N_2 blanket. The solution was further heated to 160 ^{o}C and 0.5 mmol $Ni(acac)_2$ dissolved in the mixture of 2 mL OAm and 2 mL ODE was injected into the solution. The reaction solution was finally heated to 240 ^{o}C at a ramping rate of 3-4 ^{o}C/min and kept there for 1 hour. After cooled down to 50 ^{o}C, the solution was transferred into two 50 mL centrifuge tubes and 25 mL isopropanol was added into each centrifuge

tube to precipitate the NWs. The product was collected by centrifugation at 8500 rpm for 8 min. The obtained NWs were further washed by ethanol (25 mL) for three times and redispersed in hexane for following use.

Synthesis of FeNiPt/FePt NWs

0.25 mmol $Pt(acac)_2$ was dissolved in 10 mL ODE in presence of 2 mL OAm and 1.5 mL oleic acid (OA). The solution was heated up to 115 ^oC for 30 mins to remove the dissolved oxygen and moisture. Then 30 mg of the as-synthesized FeNiPt NWs in 2 mL hexane were added into the reaction solution as seeds. After 5 mins, 0.25 mmol $Fe(CO)_5$ was added into the solution to initiate the nucleation on the existing seeds under a N_2 blanket. The whole reaction solution was further raised to 220 ^oC at a rate of 3-4 ^oC and kept at this temparature for 30 mins before cooling down to room temperature. The precipitation and purification process was same as in the FeNiPt NWs' synthesis.

Surface activation of FeNiPt/FePt NWs

20 mg FeNiPt/FePt NWs was deposited on 20 mg carbon support through sonication the mixture of NWs' hexane dispersion and Ketjen EC-300J Carbon (C) for 1 hour. The C-FeNiPt/FePt NWs were precipitated out by centrifugation at 8500 rpm for 8mins. C-FeNiPt/FePt NWs were mixed with 25 mL acetic acid (AA) and heated up to 70 ^oC under a gentle N_2 flow for 12 hours to remove the surfactant and surface Fe. The C-FeNiPt/Pt NWs were washed first by deionized water followed by ethanol for two times to remove the excess AA and dried at ambient condition to

form powder for following use. Thermal annealing at 300 ^{o}C for 2 hours under a gentle forming gas flow was applied to produce C-FeNiPt/Pt-skin NWs.

Electrochemical Measurements

The commercial C-Pt, C-FeNiPt/Pt-skeleton NWs and C-FeNiPt/Pt-skin NWs were suspended in a mixture of deionized water, isopropanol and Nafion (V/V/V=4/1/0.05) to form an ink. 20 µl ink (2 mg/mL) was deposited on the polished glassy carbon (GC) working electrode and dried at ambient condition. The Pt-loading on GC was calculated to be 8.4 µg and 10.0 µg for C-FeNiPt/Pt-skeleton and C-FeNiPt/Pt-skin NWs by ICP-AES, respectively. The catalysts were first cycled at 100 mV/s in 0.1 M $HClO_4$ until stable CVs were obtained. CVs at 50 mV/s in N_2-saturated $HClO_4$ were obtained to estimate $ECASA_{Hupd}$. CO stripping was obtained after CO bubbling at 0.1 V for 15 mins. Linear scan voltammetry was conducted in an O_2-saturated 0.1 M $HClO_4$ solution by sweeping the potential from 0.26 to 1.06 V at 10 mV/s (1600 rpm). The stability test was studied by cycling potential between 0.66 V to 1.06 V at a rate of 100 mV/s for 10000 times in O_2-saturated 0.1 M $HClO_4$. Specific and mass activities were obtained at both 0.85 V and 0.9 V and were depicted as kinetic current densities normalized to the $ECASA_{CO}$ and Pt mass loading.

5.3 Results and Discussion

5.3.1 Synthesis of Core/Shell FeNiPt/FePt NWs

To perform our study, we first prepared FeNiPt/FePt core/shell NWs through a

seed-mediated growth by modifying previous reported method (see **Experimental**).[16] Ni is chosen because of its proper modification on Pt d-band to maximize the balance between the adsorption and desorption of the oxygenated species in ORR.[20] $Fe(CO)_5$ is necessary for the 1-D structure formation.[11, 15] FeNiPt NWs with a diameter of 2.5 nm was firstly synthesized as seeds via previous reported method.[11] The composition of FeNiPt can be readily tuned by controlling metal precursor ratio according to our previous report. Here we chose $Fe_{36}Ni_{32}Pt_{32}$ (Fe: Ni: Pt~1) as the representative system to study the surface structure effect. In the coating process, thermal decomposition of iron pentacarbonyl ($Fe(CO)_5$) initiates platinum acetylacetonate ($Pt(acac)_2$) reduction and Pt nucleation onto the existing FeNiPt NW seeds. The mass ratio between NW seed and metal precursor can be used to control the shell thickness.[16] Figure 5.2.1 and Figure 5.2.2 show the typical TEM images of as-synthesized FeNiPt and FeNiPt/FePt core/shell NWs. The size of FeNiPt NW was approximately 2.5 ± 0.2 nm x 20-50 nm (Figure 5.2.1). The core/shell FeNiPt/FePt NW was 4.5 ± 0.3 nm thick, indicating 1 nm shell coating (Figure 5.2.2). 1 nm shell coating was proved to be uniform as well as efficient to achieve both electronic and strain effects to modify surface Pt electronic structure.[21-22] HRTEM image of FePtNi NWs shows an interplanar distance of 0.22 nm, corresponding to (111) plane (Figure 5.2.3).

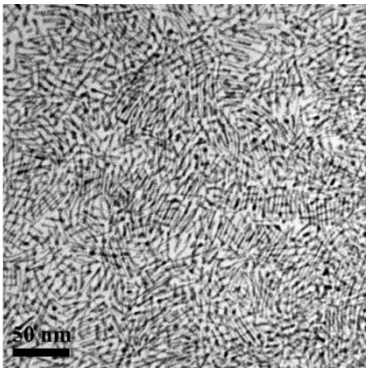

Figure 5.2.1 TEM images of the as-synthesized FeNiPt NWs.

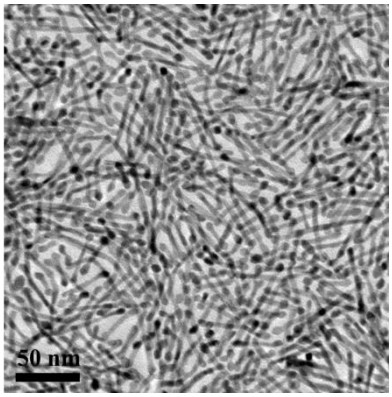

Figure 5.2.2 TEM images of the as-synthesized FeNiPt/FePt NWs.

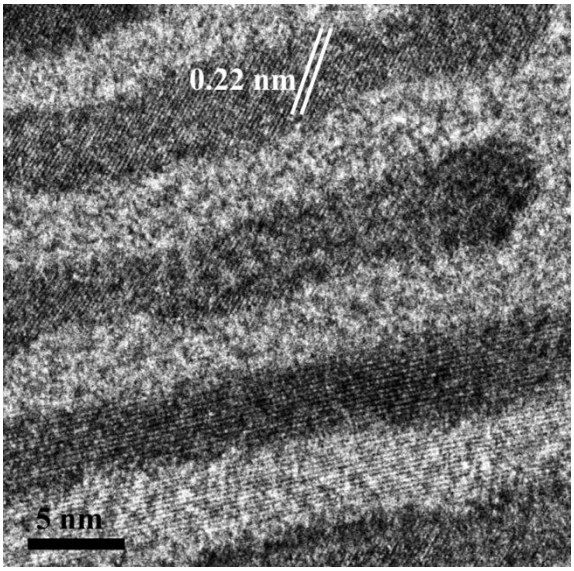

Figure 5.2.3 HRTEM image of FeNiPt/FePt NWs.

5.3.2 Surface Structure Control of FeNiPt/Pt NWs

With the as-synthesized FeNiPt/FePt NWs, we first loaded them on carbon (C) Ketjen EC-300J through sonication the mixture of NWs' hexane dispersion and C for 1 hour till the solution becomes colourless. Then the acetic acid (AA) treatment at 70 ^{o}C for 12 hours was applied to remove the surfactant and surface Fe according to previous reports.[21] The pre-leached core/shell NWs present a Pt-skeleton structure with only surface vulnerable 3d transition metal (Fe) been removed. Inductively coupled plasma atomic emission spectroscopy (ICP-AES) was applied to track the transition metal ratio change during the process. The as-synthesized FeNiPt seeds had a ratio of Fe: Ni: Pt=36: 32: 32. After FePt coating, the ratio was changed to Fe: Ni: Pt=42: 12: 46, indicating an equal ratio of Fe and Pt atoms were coated on the FeNiPt surface. After acid treatment, the final ratio of FeNiPt/FePt was changed to Fe: Ni: Pt=35: 13: 52. With Ni to Pt ratio almost unchanged (from 12:46 to 13:52) and Fe to Pt ratio changed drastically (from 42:46 to 35:52), we think this core/shell structure with surface FePt coating was effective to protect vulnerable early transition metal component Ni in the core region and only surface Fe was removed from the NWs. Further high temperature annealing (300 ^{o}C for 2 hours) of the pre-leached core/shell NWs in forming gas (95% argon, 5% hydrogen) promotes surface Pt atoms to rearrange into the multi-layer Pt-skin structure.[19] This annealing temperature was found to be the best condition to maintain the 1-D morphology. As shown in Figure

5.2.4, neither aggregation nor damage of 1-D structure was observed after annealing. Annealing at higher temperature such as 350 ^{o}C breaks the 1-D structure.

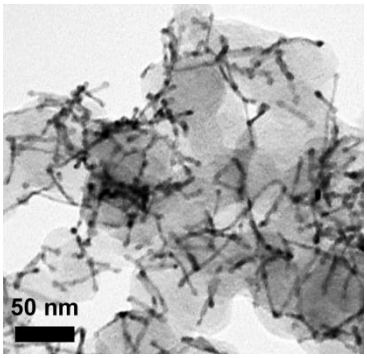

Figure 5.2.4 TEM images of C-FeNiPt/FePt after acid treatment and thermal annealing.

X-ray diffraction (XRD) pattern was first applied to track the structure evolution in these multimetallic NWs at different reaction stage. Figure 5.2.5 shows the XRD patterns of FeNiPt, FeNiPt/FePt, FeNiPt/Pt-skeleton and FePtNi/Pt-skin NWs. (111) peak position of all the NWs shifts to a higher angle comparing with pure Pt, indicating a reduction of lattice parameter due to the incorporation of Fe and Ni. At the same time, the (111) peak of FeNiPt/FePt NWs becomes narrower than FeNiPt NWs, indicating FePt coating increases the crystal domain size. Furthermore, high temperature annealing improves the NWs' crystallinity. As shown in Figure 5.2.5A, sharper peaks are observed in FeNiPt/Pt-skin NWs. Figure 5.2.5B indicates acid etching can effectively remove the surface Fe, demonstrated by a backshift to a lower

angle in FeNiPt/Pt-skeleton and FeNiPt/Pt-skin NWs comparing with FeNiPt/FePt NWs.

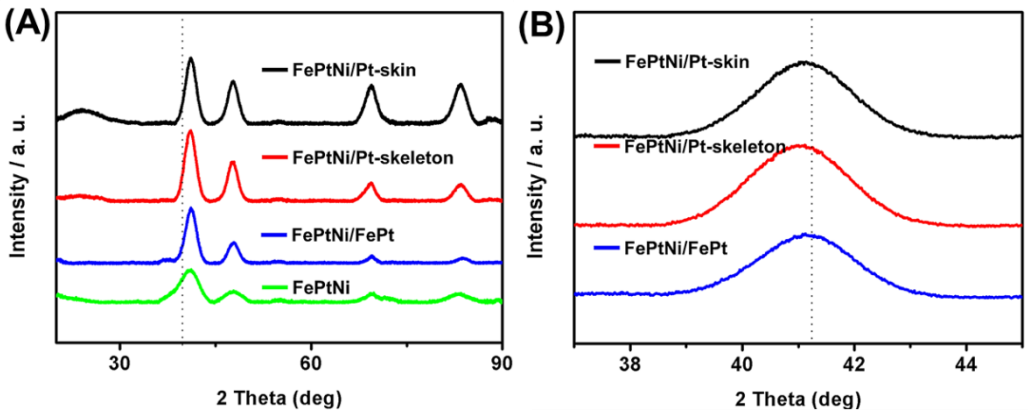

Figure 5.2.5 (A) XRD patterns of FeNiPt, FeNiPt/FePt, FeNiPt/Pt-skeleton and FeNiPt/Pt-skin NWs (dashed line denotes standard (111) peak of the bulk Pt). (B) (111) peak positions of FeNiPt/FePt, FeNiPt/Pt-skeleton and FeNiPt/Pt-skin NWs (dashed line denotes the (111) peak of FeNiPt/FePt NWs).

The FeNiPt/Pt-skeleton and FeNiPt/Pt-skin structures were further characterized by high-angle annular dark field (HAADF)-scanning transmission electron microscopy (STEM), STEM-electron energy-loss spectroscopy (STEM-EELS) and HRTEM. Figure 5.2.6A and Figure 5.2.6B show a typical HAADF-STEM image of a single FeNiPt/Pt-skin and FeNiPt/Pt-skeleton core/shell NWs. Boundaries were observed in the image. These boundaries were induced from the atom dislocation during the seed-mediated coating process, confirming the core/shell structure formation. STEM-EELS of both core/shell NWs after acid treatment and thermal annealing (Figure 5.2.7) proves the formation of Pt-shell and FeNiPt-core structure. HRTEM image (Figure 5.2.8) further proves a smoother surface in FeNiPt/Pt-skin

structure while humps are observed in FePtNi/Pt-skeleton structure.

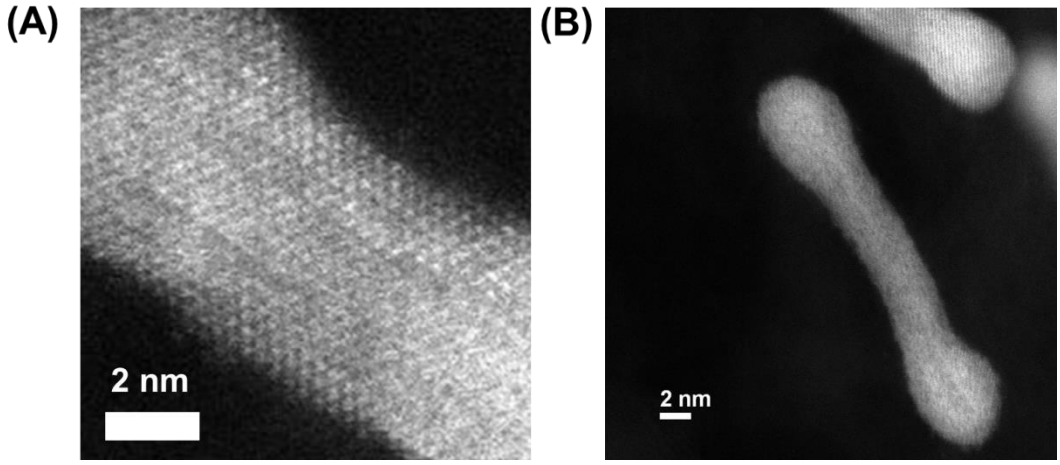

Figure 5.2.6 HAADF-STEM image of the FeNiPt/Pt-skin NWs (A) and FeNiPt/Pt-skeleton NWs (B).

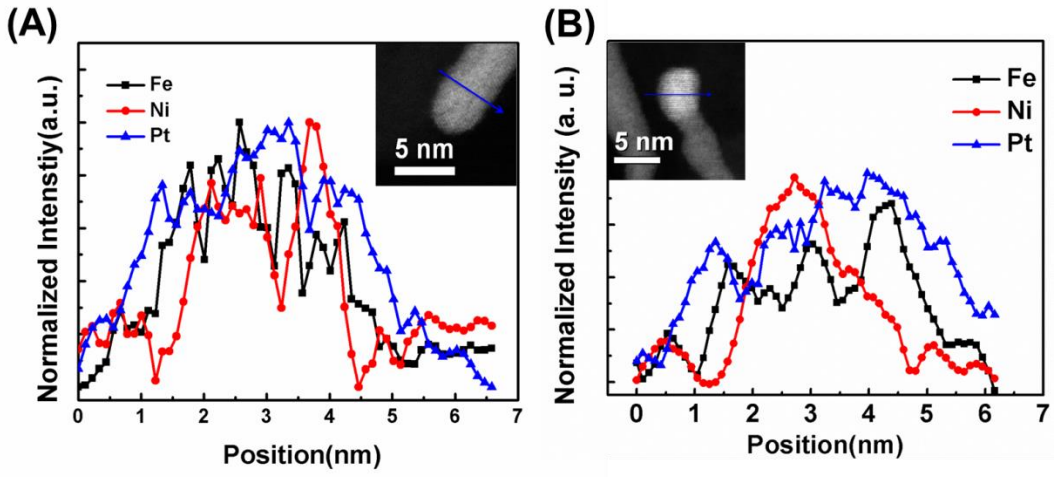

Figure 5.2.7 STEM-EELS line scan of the FeNiPt/Pt-skin NWs (A) and FeNiPt/Pt-skeleton NWs (B).

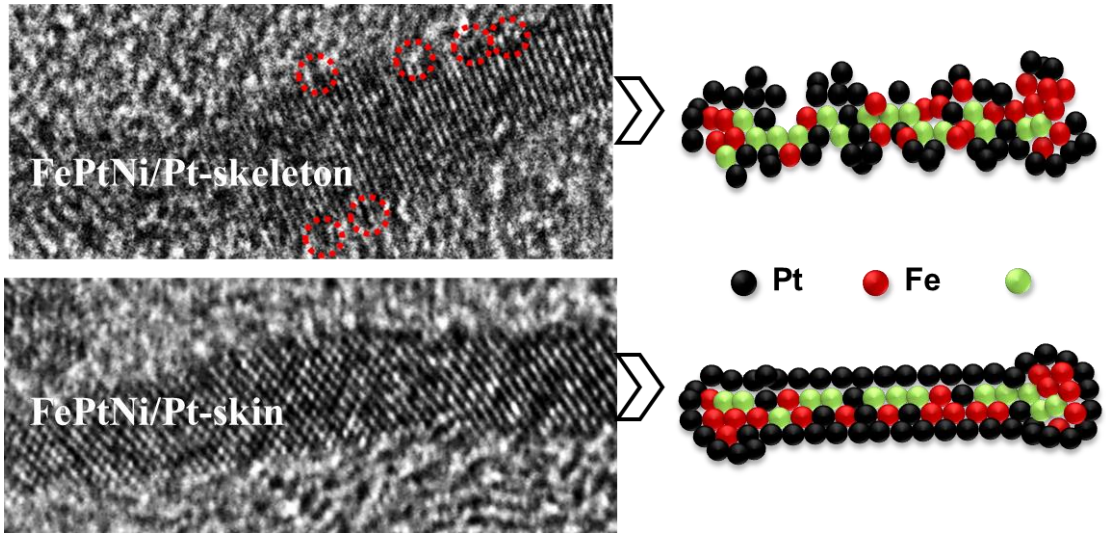

Figure 5.2.8 HRTEM images of a single FePtNi/Pt-skeleton and FePtNi/Pt-skin NW.

5.3.3 Catalytic Properties of FeNiPt/Pt NWs

To evaluate the electrocatalytic activities of FeNiPt/Pt-skeleton and FeNiPt/Pt-skin core/shell NWs on carbon, the catalyst ink was prepared (see Experimental). 20 μl of the catalyst ink was deposited on the glassy carbon rotation disk electrode (GC-RDE) and dried at ambient condition. Figure 5.2.9A shows the cyclic voltammetry (CV) scans of commercial C-Pt (20% mass loading with Pt NP diameter of 2.5-3.5 nm, Fuel Cell Store), C-FeNiPt/Pt-skeleton (21% Pt-mass loading) and C-FeNiPt/Pt-skin (25% Pt-mass loading) in 0.1 M $HClO_4$. In the range from 0.05 to 0.4 V, the pair of characteristic hydrogen underpotential formation/stripping peaks on Pt surface was obtained and used to estimate the electroactive surface area (ECASA) of the catalysts according to previous reports.[11] The ECASA was also estimated by electro-oxidation of adsorbed CO molecules (CO stripping).[16] Figure 5.2.10 demonstrates typical CO-stripping on FeNiPt/Pt-skeleton and FeNiPt/Pt-skin surfaces. One major peak was observed between 0.71 V-0.72 V, followed by a shoulder peak at 0.78 V. On FeNiPt/Pt-skeleton surface, this shoulder peak is more prominent than the one on FeNiPt/Pt-skin surface. This shoulder peak at a higher potential can be attributed to adsorbed CO oxidation on low coordination sites, which needs a higher energy.[23] The

suppressed shoulder peak on FeNiPt/Pt-skin surface indicates less low coordination atoms presented on the surface, confirming a smoother surface structure comparing with FeNiPt/Pt-skeleton NWs. The ratio between ECASA values determined by hydrogen underpotential deposition ($ECASA_{Hupd}$) and by CO stripping ($ECASA_{CO}$) was summarized in Table 5.1. The $ECASA_{CO}$ was estimated to be higher than $ECASA_{Hupd}$ in FeNiPt/Pt-skin structure, suggesting the formation of the Pt-skin surface structure.[24-25]

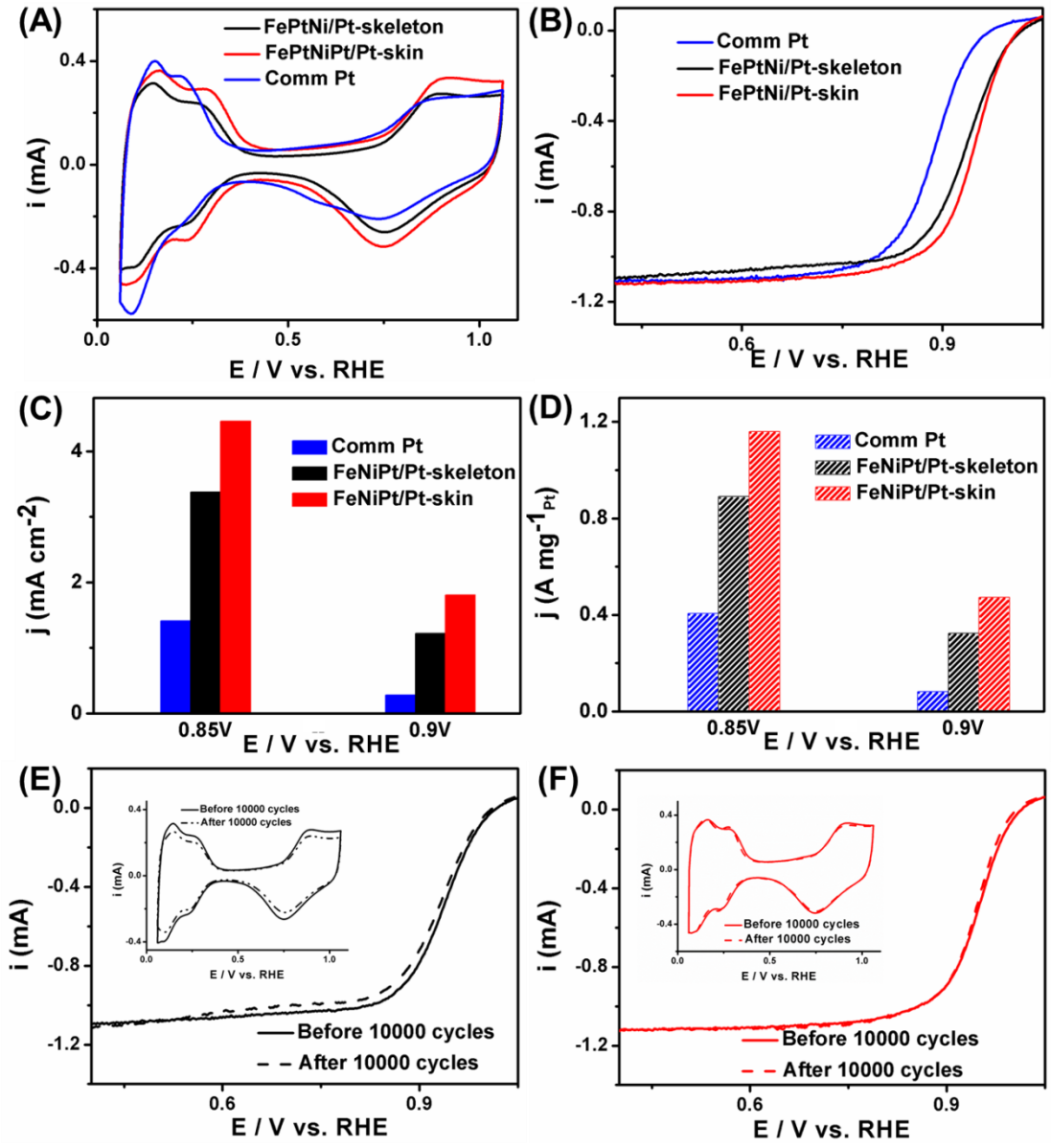

Figure 5.2.9 (A) CVs, (B) polarization curves with the rotating disk electrode rotation rate at 1600 rpm, (C) specific activities and (D) mass activities of the commercial C-Pt NPs, C-FeNiPt/Pt-skeleton and C-FeNiPt/Pt-skin NWs. Polarization curves before and after 10000 potential cycles with rotating disk electrode ration rate at 1600 rpm of E) C-FeNiPt/Pt-skeleton NWs and F) C-FeNiPt/Pt-skin NWs (insets: CVs of C-FeNiPt/Pt-skeleton and C-FeNiPt/Pt-skin NWs before and after 10000 potential cycles).

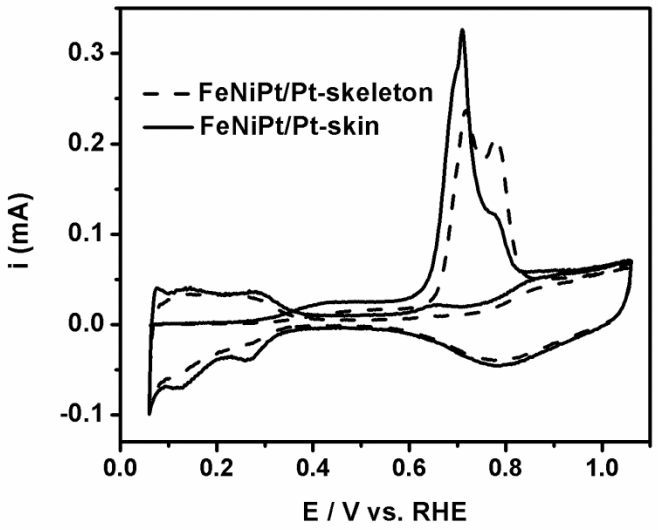

Figure 5.2.10 CO-stripping curves for FeNiPt/Pt-skeleton and FeNiPt/Pt-skin NWs.

	FePtNi/Pt-skeleton	FePtNi/Pt-skin
$ECASA_{CO}/ECASA_{Hupd}$	1.03	1.12

Table 5.1 Ratios between electrochemical surface areas (ECASA) from integrated

charge obtained by electrooxidation of adsorbed COad and underpotentially deposited hydrogen (Hupd).

ORR polarization curves were obtained by linear scan voltammetry (LSV) from 0 to 0.8 V in 0.1 $HClO_4$ at a sweep rate of 10 mV/s and a GC-RDE rotation speed of 1600 rpm. We can see that C-FeNiPt/Pt-skin shows a largely positive-shifted half-wave potential (0.944V) comparing with commercial Pt (0.880 V) and C-FeNiPt/Pt-skeleton (0.932 V) (Figure 5.2.9B). The kinetic current was calculated from the LSV curve by mass-transport correction and further normalized to $ECASA_{CO}$ and Pt mass to generate both specific and mass activities for each catalyst. As a result, C-FeNiPt/Pt-skin NWs achieve the specific activity of 4.46 mA/cm^2 at 0.85 V and 1.81 mA/cm^2 at 0.9 V (vs. reversible hydrogen electrode, RHE) respectively, higher than previously reported ultrathin FePt and FeNiPt NWs and NRs.[11, 16] C-FeNiPt/Pt-skeleton shows the specific activity of 3.38 mA/cm^2 at 0.85 V and 1.22 mA/cm^2 at 0.9 V, while the commercial C-Pt NPs only show the specific activity of 1.41 mA/cm^2 (0.85V) and 0.28 mA/cm^2 (0.9V) (Figure 5.2.9C). The mass activities were also summarized in Figure 4D with C-FeNiPt/Pt-skin reaching 1160 mA/mg at 0.85 V and 473 mA/mg at 0.9 V, higher than U. S. Department of Energy's 2017 target (440 mA/mg Pt). On the other hand, C-FeNiPt/Pt-skeleton has a mass activity of 890 mA/mg_{Pt} at 0.85 V and 324 mA/mg_{Pt} at 0.9 V, while commercial Pt only possesses a mass activity of 406 mA/mg at 0.85 V and 82 mA/mg at 0.9 V

(Figure 5.2.9D). The enhancement of the ORR activity in FeNiPt/Pt-skin core/shell NWs was originated from the smoother Pt-skin structure comparing with FePtNi/Pt-skeleton core/shell NWs. With a largely-reduced low coordination sites in FeNiPt/Pt-skin surface, the Pt atoms are less subject to OH^- and other oxygenated species blocking and hence an increased activity was obtained. Active as it is, stability is even more important for future fuel cell catalyst design and commercialization. Our recent work for 1-D NWs and NRs has demonstrated the superior durability of these materials owing to the strong interaction between the C support and the material.[11, 15-16] Here we further proved with a smoother Pt-surface, the stability of these 1-D materials can be improved. As shown in Figure 5.2.9E-F, we found that after 10000 CV cycles in O_2-staruated acid electrolyte, the FeNiPt/Pt-skin NWs show almost no $ECASA_{Hupd}$ and activity drop (Figure 5.2.9F), confirming a stable structure for ORR catalysis, while FeNiPt/Pt-skeleton NWs clearly dropped around 15% of its initial ECASA and 9 mV half-wave potential in the same testing condition (Figure 5.2.9E). The enhanced durability of the FeNiPt/Pt-skin NWs was also originated from the less dissolution of Pt atoms owing to a less-defected Pt-surface comparing with FeNiPt/Pt-skeleton ones.[19]

5.4 Conclusion

In conclusion, we have synthesized FeNiPt/FePt core/shell NWs through a seed-mediated organic chemical synthesis method. The surface profile of the core/shell NWs can be controlled through acid etching and thermal annealing to be

either Pt-skeleton or Pt-skin structure with their 1-D morphology being maintained. These core/shell NWs show both higher activity and durability in catalyzing ORR in acid electrolyte comparing with previous reported ultrathin NWs and commercial Pt NPs. More interestingly, FeNiPt/Pt-skin NWs demonstrated higher performance than FeNiPt/Pt-skeleton ones. This is attributed to the fine tuning of the surface profile achieved in FeNiPt/Pt-skin NWs with less low coordination Pt atoms presented on the surface. The fine tuning of the surface profile of monodisperse 1-D nanomaterial opens the avenue for rational design and synthesis of advanced functional nanomaterials for catalytic reactions.

References

1. Y. Bing, H. Liu, L. Zhang, D. Ghosh, J. Zhang, *Chem. Soc. Rev.* **2010**, *39*, 2184 – 2202.

2. J. Chen, B. Lim, E. P. Lee, Y. Xia, *Nano Today* **2009**, *4*, 81 – 95.

3. J. Suntivich, H. A. Gasteiger, N. Yabuuchi, H. Nakanishi, J. B. Goodenough, S. Yang, *Nat. Chem.* **2011**, *3*, 546 – 550.

4. C. Cui, H. Li, J. Yu, M. Gao, S. Yu, *Angew. Chem. Int. Ed.* **2010**, *49*, 9149 – 9152.

5. S. Zhang, S. Guo, H. Zhu, S. Sun, *J. Am. Chem. Soc.*, **2012**, *134*, 5060–5063.

6. S. Guo, S. Zhang, S. Sun, *Angew. Chem. Int. Ed.* **2013**, *52*, 8526 – 8544.

7. C. Wang, H. Daimon, T. Onodera, T. Koda, S. Sun, *Angew. Chem. Int. Ed.* **2008**, *47*, 3588 – 3591.

8. J. Wu, L. Qi, H. You, A. Gross, J. Li, H. Yang, *J. Am. Chem. Soc.* **2012**, *134*, 11880 – 11883.

9. C. Wang, D. van der Vliet, K.-C. Chang, H. You, D. Strmcnik, J. A. Schlueter, N. M. Markovic, V. R. Stamenkovic, *J. Phys. Chem. C* **2009**, *113*, 19365 – 19368.

10. S. Zhang, X. Zhang, G. Jiang, H. Zhu, S. Guo, D. Su, G. Lu, S. Sun, *J. Am. Chem. Soc.*, **2014**, *136*, 7734–7739.

11. H. Zhu, S. Zhang, S. Guo, D. Su, S. Sun, *J. Am. Chem. Soc.*, **2013**, *135*, 7130–7133.

12. C. Cui, L. Gan, M. Heggen, S. Rudi, P. Strasser, *Nat. Mater.* **2013**, *12*, 765-771.

13. C. Wang, D. Li, M. Chi, J. Pearson, R. B. Rankin, J. Greeley, Z. Duan, G. Wang, D. van der Vliet, K. L. More, N. M. Markovic, V. R. Stamenkovic, *J. Phys. Chem. Lett.* **2012**, *3*, 1668-1673.

14. C. Cui, L. Gan, H. Li, S. Yu, M. Heggen, P. Strasser, *Nano Lett.* **2012**, *12*, 5885-5889.

15. S. Guo, D. Li, H. Zhu, S. Zhang, N. M. Markovic, V. R. Stamenkovic, S. Sun, *Angew. Chem. Int. Ed.* **2013**, *52*, 3465 –3468.

16. S. Guo, S. Zhang, D. Su, S. Sun, *J. Am. Chem. Soc.*, **2013**, *135*, 13879–13884.

17. D. S. Strmcnik, D. V. Tripkovic, D. van der Vliet, K. C. Chang, V. Komanicky, H. You, G. Karapetrov, J. Greeley, V. R. Stamenkovic, N. M. Markovic, *J. Am. Chem. Soc.* **2008**, *130*, 15332–15339.

18. R. Borup, J. Meyers, B. Pivovar, Y. S. Kim, R. Mukundan, N. Garland, D. Myers, M. Wilson, F. Garzon, D. Wood, P. Zelenay, K. More, K. Stroh, T. Zawodzinski, J. Boncella, J. E. McGrath, M. Inaba, K. Miyatake, M. Hori, K. Ota, Z. Ogumi, S. Miyata, A. Nishikata, Z. Siroma, Y. Uchimoto, K. Yasuda, K. Kimijima, N. Iwashita, *Chem. Rev.* **2007**, *107*, 3904–3951.

19. C. Wang, M. Chi, D. Li, D. Strmcnik, D. van der Vliet, G. Wang, V. Komanicky, K. Chang, A. P. Paulikas, D. Tripkovic, J. Pearson, K. L. More, N. M. Markovic, V.R. Stamenkovic, *J. Am. Chem. Soc*. **2011**, *133*, 14396-14403.

20. V. R. Stamenkovic, B. S. Mun, M. Arenz, K. J. J. Mayrhofer, C. A. Lucas, G. Wang, P. N. Ross, N. M. Markovic, *Nat. Mater.* **2007**, *6*, 241−247.

21. V. Mazumder, M. Chi, K. L. More, S. Sun, *J. Am. Chem. Soc.* **2010**, *132*, 7848-7849.

22. X. Sun, D. Li, Y. Ding, W. Zhu, S. Guo, Z. Wang, S. Sun, *J. Am. Chem. Soc.* **2014**, *136*, 5745-5749.

23. S. Brimaud, Z. Jusys, R. J. Behm, *Beilstein J. Nanotechnol*. **2014**, *5*, 735-746.

24. C. Chen, Y. Kang, Z. Huo, Z. Zhu, W. Huang, H. Xin, J. D. Snyder, D. Li, J. A. Herron, M. Mavrikakis, M. Chi, K. L. More, Y. Li, N. M. Markovic, G. A. Somorjai, P. Yang, V. R. Stamenkovic, Science 2014, 343, 1339-1343.

25. D. F. van der Vliet, C. Wang, D. Li, A. P. Paulikas, J. Greeley, R. B. Rankin, D. Strmcnik, D. Tripkovic, N. M. Markovic, V. R. Stamenkovic, *Angew. Chem. Int. Ed.* **2012**, *51*, 3139-3142.

Chapter 6

Structure Control of FePt Nanoparticles for Oxygen Reduction Reaction

6.1 Background and Introduction

In Chapter 3-5, we have demonstrated our strategy to control 1-D nanomaterial to enhance their catalysis involved in energy conversion reaction. In the past decades, in searching for highly efficient nanoparticle (NP) catalysts for energy conversions, such as for oxygen reduction reaction (ORR), one often explores Pt-based NP sizes, shapes, and compositions as important parameters to tune NP catalytic properties.[1-4] It has become increasingly important to rationalize NP parameters with catalysis in order to provide predictable models and rules for catalyst design and optimization. As we demonstrated in Chapter 1, recent studies on ORR have indicated that Pt-Pt bond compression and the resultant d-band down-shift weaken the bonding between Pt and oxygenated species (O) and increase catalytic activity for ORR.[5-7] Density functional theory (DFT) calculations further indicate that Pt-O binding energy (E_O), a key "descriptor" to measure the adsorption/desorption of oxygenated species, should be at 0.2 eV relative to the Pt (111) surface to achieve an optimum ORR activity.[8-10] However, the control of Pt-based NP catalysts' E_O to be close to the optimum value and hence to achieve an enhanced performance through control of NPs' parameters has rarely been achieved.

In this Chapter, we report a strategy to tune ORR catalysis of multimetallic core/shell NPs by controlling the crystal structure of the core and surface strain of the shell. In previous studies on ORR catalysis, chemically disordered Pt alloy NPs (PtNi, PtCo, PtFe and *etc.*) are the universal choice of the catalyst and are often in face

centered cubic (fcc) solid solution structure. Chemically ordered intermetallic structure is rarely studied as a factor due to the difficulty in obtaining such a structure without sacrificing other NP parameters, such as sizes, shapes and compositions.[11-12] Previously, we have synthesized monodisperse FePt alloy NPs with controlled sizes and compositions.[13-14] When these alloy NPs were deposited on the carbon support, they could withstand high temperature annealing without aggregation or sintering, and their solid solution-like fcc structure could be converted to intermetallic face-centered tetragonal (fct) structure. The fct structure is an intermetallic ordered structure with Fe and Pt assembled into a layer by layer architecture as shown in Figure 3.1. More importantly, electro-anodization of these FePt NPs in 0.1 M $HClO_4$ led to core/shell FePt/Pt NPs after the surface Fe dealloying. We want to study and control the surface strain of Pt atoms by controlling the core structure to be either fcc or fct in order to enhance the ORR catalysis.

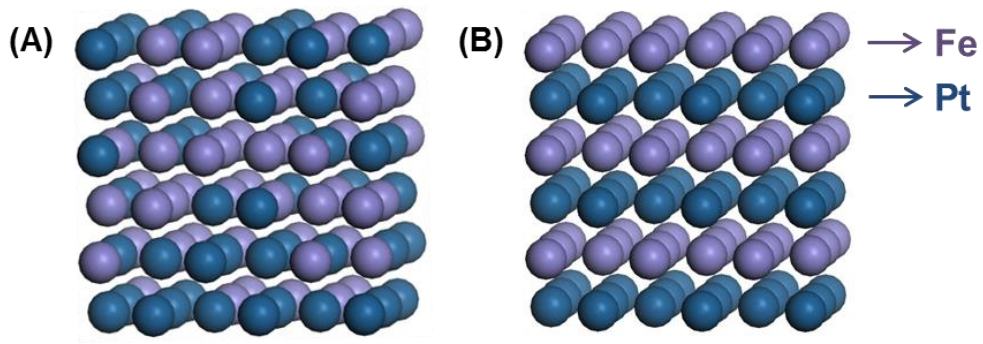

Figure 6.1 Schematic illustration of crystalline structure of *fcc*-FePt (A) and *fct*-FePt (B).

6.2 Experimental

Chemicals and Materials

Oleylamine (OAm) (>70%), oleic acid (OAc), 1-octadecene (ODE), $Pt(acac)_2$ (acac=aceylacetonate), $Cu(acac)_2$, iron pentacarbonyl ($Fe(CO)_5$), hexane, isopropanol, ethanol, and Nafion (5%) were all purchased from Sigma Aldrich and used without further purification. The commercial Pt (20% mass loading on carbon with a diameter of 2.5-3.5 nm) catalyst was obtained from Fuel Cell Store.

Characterization

Transmission electron microscopy (TEM) images were acquired from a Philips CM 20 operating at 200 kV. X-ray diffraction (XRD) patterns of the NPs were collected on a Bruker AXS D8-Advanced diffractometer with Cu Kα radiation (λ =1.5418 Å). Scanning transmission electron microscopy (STEM) analyses were carried out on a Hitachi HD2700C (200 kV) with a probe aberration-corrector, in the

Center for Functional Nanomaterials at Brookhaven National Lab. The electron energy loss spectroscopy (EELS) line-scan was obtained by a high resolution Gatan-Enfina ER with a probe size of 1.3Å. A power law function was used for EELS back-ground subtraction. TEM and high resolution-TEM (HRTEM) samples were prepared by depositing a single drop of diluted NPs dispersion on amorphous carbon coated copper grids. The inductively coupled plasma-atomic emission spectroscopy (ICP-AES) measurements were carried on a JY2000 Ultrace ICP Atomic Emission Spectrometer equipped with a JY AS 421 autosampler and 2400g/mm holographic grating. Electrochemical measurements were performed on an Autolab 302 potentiostat with glassy carbon rotating disk (5 mm in diameter) as a working electrode), Ag/AgCl (4 M KCl) as a reference electrode, and platinum wire as a counter electrode.

Synthesis of FePt NPs

Under a gentle flow of N_2, 10 mL ODE, 4 mmol OAc, 4 mmol OAm and 0.5 mmol $Pt(acac)_2$ were mixed in a four-necked flask. The mixture was magnetically stirred and heated to 120 ºC to generate a light yellow solution. 0.16 mL (1.23 mmol) of $Fe(CO)_5$ was added into the solution under the N_2 blanket. The solution was further heated to 220 ºC at a rate of about 3 °C/min and kept at this temperature for 1 h before it was cooled to room temperature. The NPs were separated by adding isopropanol (50 mL), followed by centrifugation (8500 rpm, 8 min). The NPs were further purified by dispersing into hexane (20 mL) and centrifugation (5000 rpm, 8

min) to re-move any undispersed precipitates. The product was precipitated out by adding ethanol (50 mL) and centrifugation (8500 rpm, 8 min) and redispersed in hexane. The synthesis yielded $Fe_{51}Pt_{49}$ NPs. In the same condition and when 1.07 mmol of $Fe(CO)_5$ was used in the synthesis, $Fe_{42}Pt_{58}$ NPs were obtained. In the pres-ence of 1.07 mmol of $Fe(CO)_5$ and at 200 °C (or 180 °C), $Fe_{33}Pt_{67}$ (or $Fe_{27}Pt_{73}$) NPs were separated.

Electrochemical Measurement

The NPs were first subject to cyclic voltammetry (CV) scans between 0 V and 1.0 V (vs RHE) at 100 mV/s in N_2-saturated 0.1 M $HClO_4$ until a stable CV was obtained (150 scans for the *fcc*-FePt and 300 scans for the *fct*-FePt NPs). Once the core/shell FePt/Pt NPs were obtained, their CVs were recorded at a scan rate of 50 mV/s in N_2-saturated 0.1 M $HClO_4$ and were used to estimate electrochemically active surface area (ECASA). ORR polarization curves were recorded by linear-sweep voltammetry (LSV) at a scan rate of 20 mV/s in O_2-saturated 0.1 M $HClO_4$ with the rotation disk electrode rotating at 1600 rpm.

QM-MM Simulations

Core/shell NPs are modeled by cuboctahedrons with eight (111) facets and six (100) facets. The core/shell structure consists of an fcc-Pt shell (with three atomic layers) and a FePt core. The size of NPs is 8 nm corresponding to 10179 atoms in total.

relative to the flat Pt (111) surface is determined by placing an O atom at the hollow site on the (111) facet of fcc-Pt, following

$$E_{\mathrm{O}} = (E_{\mathrm{QM/MM}}[\mathrm{NP+O}] - E_{\mathrm{QM/MM}}[\mathrm{NP}]) - (E_{\mathrm{QM}}[\mathrm{Pt(111)+O}] - E_{\mathrm{QM}}[\mathrm{Pt(111)}])$$

where $E_{\mathrm{QM/MM}}[\mathrm{NP+O}]$ and $E_{\mathrm{QM/MM}}[\mathrm{NP}]$ are total energies of NPs with and without O adsorbate, respectively from QM-MM calculations. $E_{\mathrm{QM}}[\mathrm{Pt(111)+O}]$ and $E_{\mathrm{QM}}[\mathrm{Pt(111)}]$ are the total energies of the flat Pt (111) surface with and without the absorbed O atom calculated by DFT.

In QM-MM calculations, as shown in Figure 6.2.13, the entire modeled system is partitioned into two spatial domains: a QM region (red, pink and green spheres) treated by constrained DFT and a MM region (blue spheres) by empirical atomistic simulations.[15-17] The QM region is further divided into an interior QM region and a boundary QM region. The former involves bond breaking, chemical reaction and charge transfer, etc. where topological changes of charge density take place. The latter serves as a buffer region where no such topological change to the charge density occurs. The technical details and validations of the QM-MM method can be found elsewhere.[18] The QM region measures 17Å×17Å×8Å in x, y, and z directions, respectively with 195 atoms, where the innermost 8.4Å×7.3Å×4Å is the interior QM region containing the adsorbed oxygen atom on the fcc-hollow site. The MM region consists of the rest of the system where the strain effect due to the core/shell lattice mismatch can be captured. The DFT calculations are carried out using the VASP package[19-20] with the projector augmented wave pseudopotentials (PAW)[21] and

Perdew-Burke-Ernzerhof generalized gradient approximation (PBE-GGA)8. The calculations are performed at Γ point with 400 eV energy cutoff. The embedded atom method (EAM) potentials are used in the MM simulations, which have been rescaled to yield the same lattice constant and bulk modulus as those of DFT.[22] The force convergence criterion for atomic relaxation is 0.03 eV/Å.

Equilibrium Lattice Constants of FePt NPs from DFT Calculations

A periodic supercell consisting of 108 atoms is used to determine the atomic structure of FePt core. For *fcc*-FePt, 53 Pt atoms and 55 Fe atoms are randomly arranged in the supercell; For *fct*-FePt, 54 Pt atoms and 54 Fe atoms with an alternating layers are arranged in the supercell. All atoms are fully relaxed under the constant zero pressure by using the DFT calculations. The DFT geometry optimizations are performed using the VASP package with PAW approach and PBE-GGA under the constant (zero) pressure. An energy cutoff of 280 eV is used for the plane-wave basis set. The Brillouin zone is sampled based on the Monkhorst-Pack scheme with a 3×3×3 *k*-point mesh.[23] Spin-polarized DFT calculations are used for all materials under the investigation.

6.3 Results and Discussion

6.3.1 Synthesis of FePt NPs

The fcc-FePt NPs were synthesized by the reduction of platinum acetylacetonate, $Pt(acac)_2$, and thermal decomposition of iron pentacarbonyl, $Fe(CO)_5$, in the presence

of oleylamine (OAm) and oleic acid (OAc) as reported.[24] Fe/Pt compositions were controlled by $Fe(CO)_5/Pt(acac)_2$ molar ratios and reaction temperatures, and were analyzed by inductively coupled plasma-atomic emission spectroscopy (ICP-AES) as shown in Table 6.1 Transmission electron microscopy (TEM) images show that the as-synthesized fcc-$Fe_{51}Pt_{49}$ NPs are cube-like with lateral dimension at 8.5 nm ± 0.5 nm (Figure 6.2.1). TEM images of the other FePt NPs of similar sizes are shown in Figure 6.2.2.

Sample	$Pt(acac)_2$, mol	$Fe(CO)_5$, ml	Temperature, °C	As-synthesized NPs
A	0.5	0.16	220	$Fe_{51}Pt_{49}$
B	0.5	0.14	220	$Fe_{42}Pt_{58}$
C	0.5	0.14	200	$Fe_{33}Pt_{67}$
D	0.5	0.14	180	$Fe_{27}Pt_{73}$

Table 6.1 The composition control of as-synthesized FePt NPs by varying the precursor ratio of $Fe(CO)_5/Pt(acac)_2$ and reaction temperature.

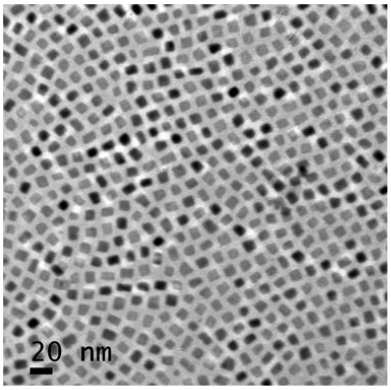

Figure 6.2.1 TEM images of the as-synthesized $Fe_{51}Pt_{49}$ NPs.

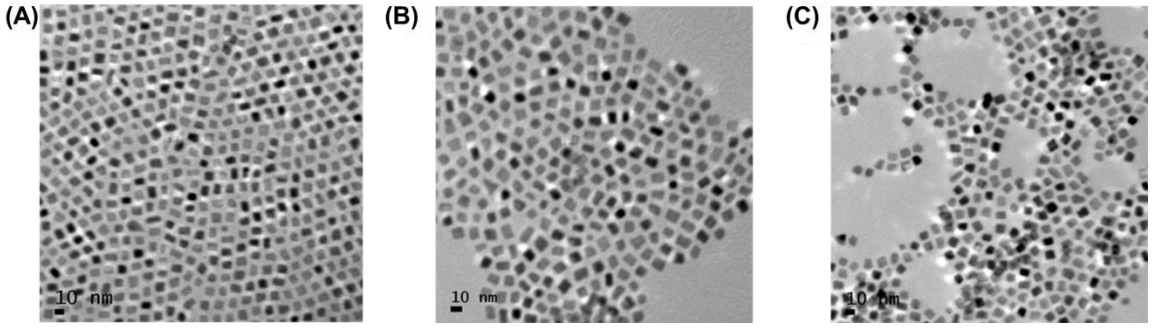

Figure 6.2.2 TEM images of the as-synthesized $Fe_{27}Pt_{73}$ (A), $Fe_{33}Pt_{67}$ (B), $Fe_{42}Pt_{58}$ (C) NPs.

6.3.2 Structure Control of FePt NPs

The fcc-FePt NPs were firstly deposited on Ketjen carbon (C), similar to what has been reported[25], and were denoted as C-FePt NPs. High temperature annealing was applied to remove the organic surfactants as well as to convert the structure. The C-FePt NPs were annealed in 95% Ar + 5% H_2 for 1 h at temperatures from 400 °C to

700 °C, and 650 °C was found to be the best temperature to convert fcc-$Fe_{51}Pt_{49}$ to fct-$Fe_{51}Pt_{49}$ without causing obvious NP aggregation/sintering, as shown in Figure 6.2.3 and Figure 6.2.4. After annealing, both fcc- and fct-FePt NPs adopted the same thermodynamically more stable polyhedral shape. The structure of fcc- and fct-FePt NPs were confirmed by X-ray diffraction pattern (XRD) with fct-FePt showing extra superlattice peaks (Figure 6.2.5). Furthermore, other Pt-rich FePt NPs could not be converted into fct structure under this annealing condition.

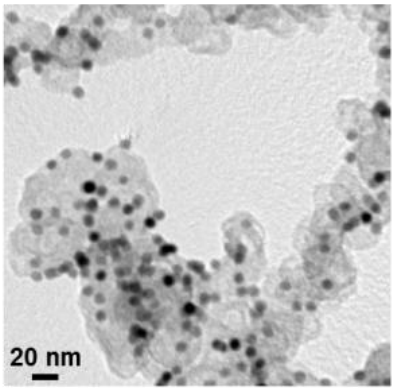

Figure 6.2.3 TEM images of the C-$Fe_{51}Pt_{49}$ after 650 ^{o}C annealing.

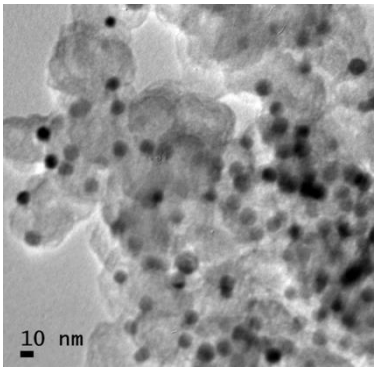

Figure 6.2.4 TEM images of the C-$Fe_{51}Pt_{49}$ after 650 ^{o}C annealing.

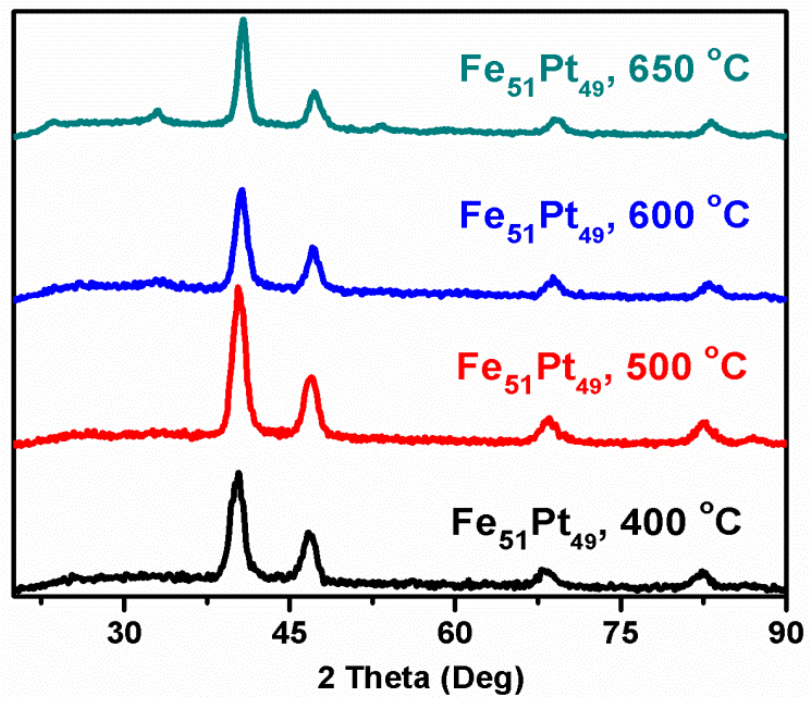

Figure 6.2.5 XRD patterns of the $Fe_{51}Pt_{49}$ NPs annealed at 400 ^{o}C, 500 ^{o}C, 600 ^{o}C and 650 ^{o}C.

6.3.3 Catalyic Properties of FePt NPs

The C-fcc-$Fe_{51}Pt_{49}$ and C-fct-$Fe_{51}Pt_{49}$ NPs were deposited on the glassy carbon (GC) rotating disk electrode (RDE) and were subject to a potential scan between -0.2 V to 1.0 V (vs. Ag/AgCl) in the N_2-saturated 0.1 M $HClO_4$ solution till a stable current-potential curve was obtained. The process oxidized and dissolved the surface Fe, leading to the formation of stable core/shell FePt/Pt NPs. The core/shell structure was observed in both fcc-FePt and fct-FePt and was characterized by

aberration-corrected high-angle annular dark field scanning transmission electron microscopy (HAADF-STEM) and STEM-electron energy loss spectroscopy (STEM-EELS), as shown in Figure 6.2.6, Figure 6.2.7 and Figure 6.2.8. Both the fcc- and fct-$Fe_{51}Pt_{49}$ NPs show a Pt-shell of ~0.6 nm (~3 atomic layers) with the FePt cores maintaining their structures. In addition, the alternate Pt and Fe layers in the fct-FePt core region are clearly indicated by their brighter (high Z-contrast for Pt) and darker (low Z-contrast for Fe) contrasts as shown in Figure 6.2.8.[25] In the core/shell NPs, the final Fe/Pt composition is measured to be at 25/75 in the fcc-FePt/Pt and 26/74 in the fct-FePt/Pt, indicating that the core/shell NPs have the same Fe/Pt ratios.

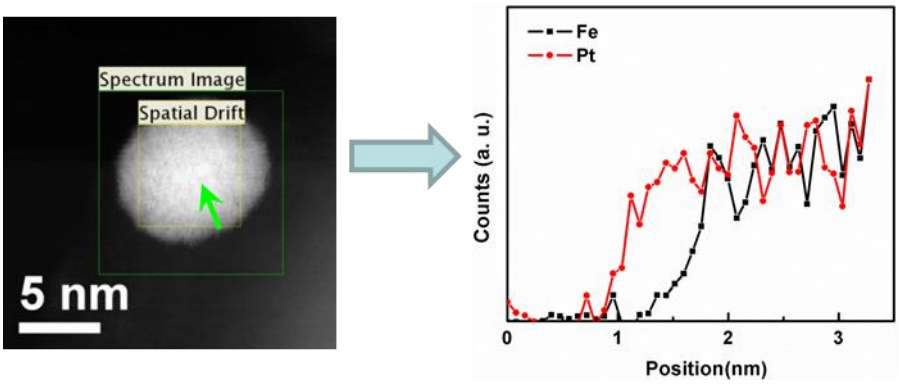

Figure 6.2.6 HAADF-STEM image and STEM-EELS line scan of an electrochemically dealloyed C-fcc-$Fe_{51}Pt_{49}$ NP, forming C-fcc-FePt/Pt. The arrow indicates the line scan position.

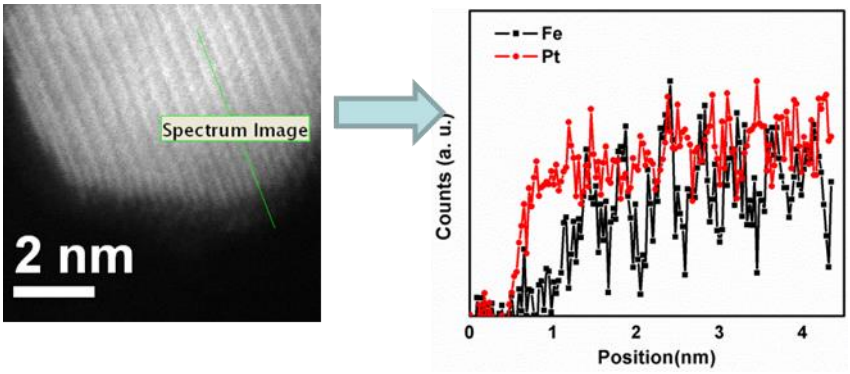

Figure 6.2.7 HAADF-STEM image and STEM-EELS line scan of an electrochemically dealloyed C-fct-$Fe_{51}Pt_{49}$ NP, forming C-fct-FePt/Pt. The arrow indicates the line scan position.

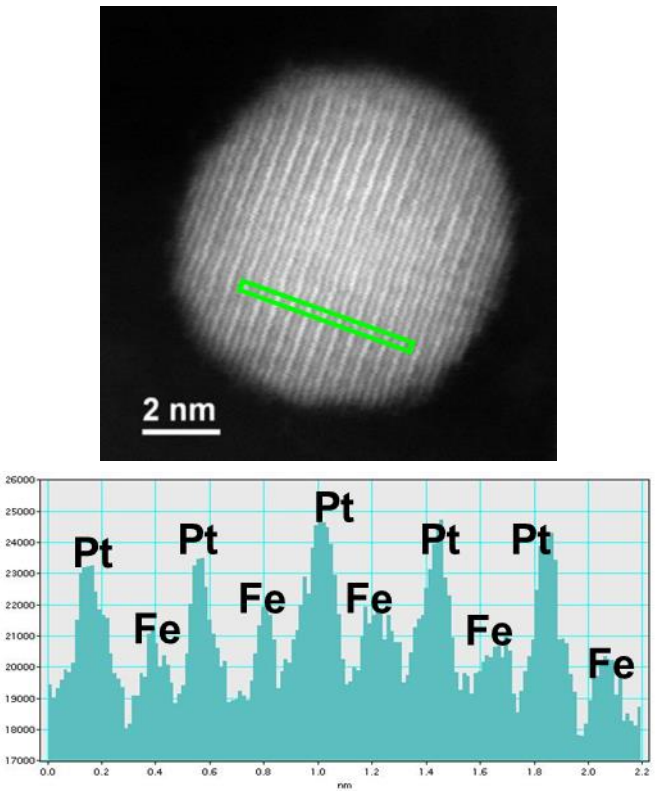

Figure 6.2.8 STEM-EELS line scan of an electrochemically dealloyed C-fct-$Fe_{51}Pt_{49}$

NP. The green line indicates the line scan position, confirming an ordered structure core.

Electrochemically active surface area (ECASA) of the FePt/Pt, as well as the commercial Pt (2.5-3.5 nm Pt NPs), were obtained by integrating the hydrogen underpotential desorption (Hupd) peaks of their cyclic voltammograms (CVs) (Figure 6.2.9).[26] Their ORR polarization curves are shown in Figure 6.2.10A with fct-FePt/Pt showing a positively shifted half-wave potential comparing with fcc-FePt/Pt. The specific current density of commerical Pt (0.32 mA/cm2), fcc-FePt/Pt (1.63 mA/cm^2) and fct-FePt/Pt (2.95 mA/cm^2) was further summarized in Figure 6.2.10B. We can see clearly that fct-FePt/Pt is more active than fcc-FePt/Pt and Pt NPs for ORR catalysis. Stability test was carried out by cycling between 0.6 V and 1.0 V for 4000 scans at 50mV/s, room temperature. We found that fct-FePt/Pt NPs were highly durable as shown in Figure 6.2.11 and Figure 6.2.12 with no obvious ECASA and specific activity drop after the 4000 cycles.

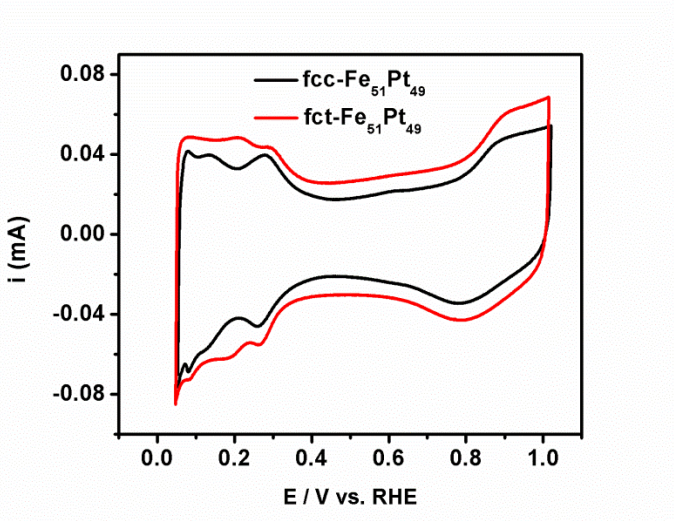

Figure 6.2.9 CVs of the *fcc*-FePt/Pt and *fct*-FePt/Pt NPs in N_2-saturated 0.1 M $HClO_4$ with the scan rate of 50 mV/s.

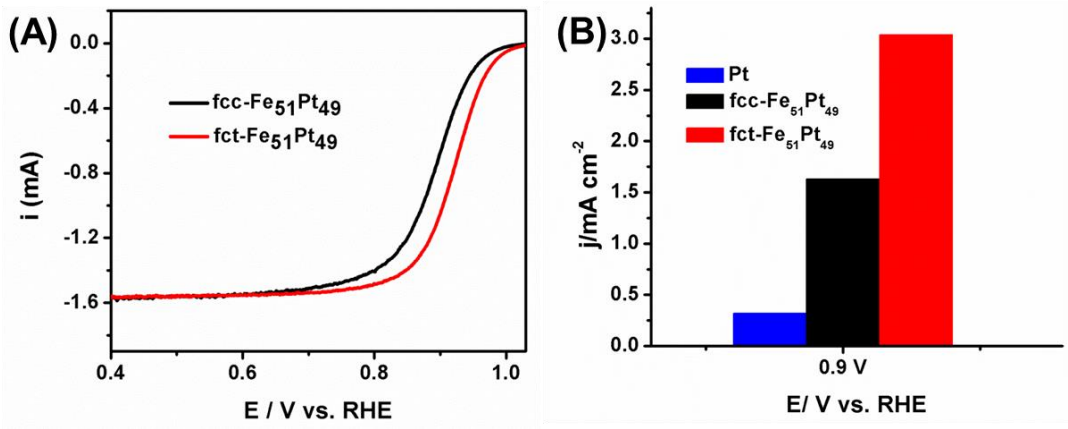

Figure 6.2.10 (A) ORR polarization curves of fcc-FePt/Pt and fct-FePt/Pt in O_2-saturated 0.1 M $HClO_4$ (1600 rpm) at a scan rate of 20 mV/s. (B) Specific activities of commercial Pt, fcc-FePt/Pt and fct-FePt/Pt at 0.9 V vs. RHE.

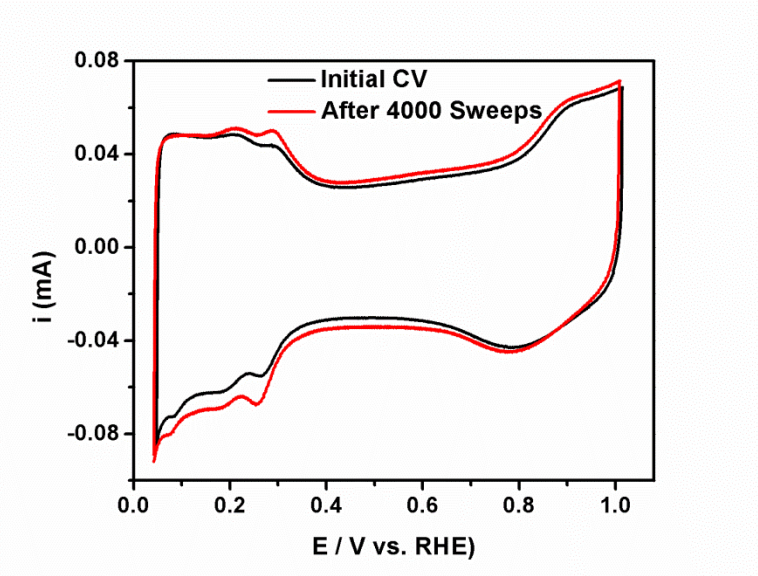

Figure 6.2.11 CVs of the fct-FePt/Pt NPs before and after stability test in N_2-saturated 0.1 M $HClO_4$ with the scan rate of 50 mV/s.

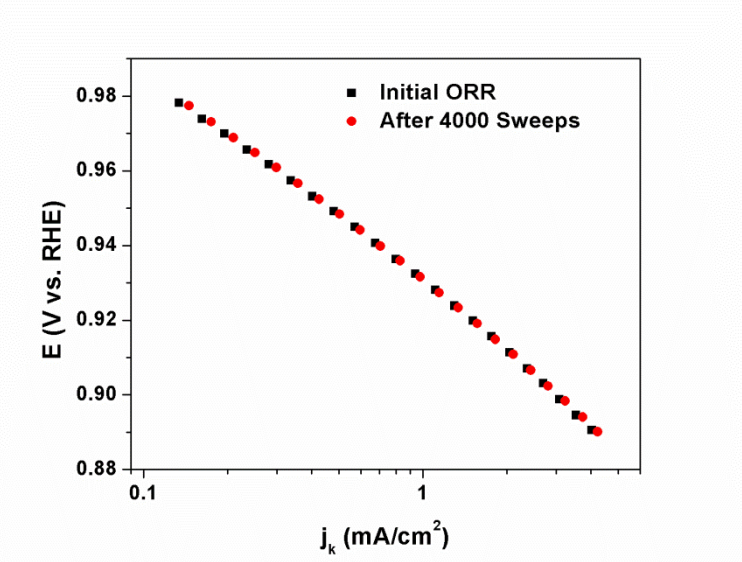

Figure 6.2.12 Specific current density as a function of potential of *fct*-FePt/Pt NPs before and after stability test (Tafel plot).

Since both fcc-FePt/Pt and fct-FePt/Pt are monodisperse NPs with the same size, shape, Fe/Pt ratio and Pt thickness (~3 atomic layers of Pt), their ORR catalysis difference must originate from structure-induced surface change. To understand this change, we performed quantum mechanics-molecular mechanics (QM-MM) simulations to calculate Pt-O binding energies on the surface of the FePt/Pt NPs (see **experimental**). The QM-MM modeling combines both the quantum mechanical and classical descriptions where the QM density functional theory (DFT) is applied to reactive sites to capture chemical reactions, while the long-range strain field of NPs is handled by the classical MM method.[27-28] As a result, the QM-MM method can treat much larger particle sizes (e.g., 8 nm) than previously feasible (~1 nm).[29-30] We built an 8 nm cuboctahedral core/shell NP model consisting of $Fe_{50}Pt_{50}$ alloy core (fcc- or fct-FePt) and fcc-Pt shell (3 atomic layers) (Figure 6.2.13). The core/shell FePt/Pt NPs have a theoretical composition of around $Fe_{25}Pt_{75}$, consistent with the FePt/Pt NPs studied experimentally. Figure 6.2.13C illustrates atomic configuration of a cuboctahedral NP, which is partitioned to QM region and MM region. By using QM-MM and by placing an O atom at the center of the QM region, we calculated E_O's of the fcc-FePt/Pt and fct-FePt/Pt to be 0.26 eV and 0.23 eV respectively. Commercial Pt catalyst was also simulated to have an EO of 0.1 eV based on QM-MM method and 3 nm NP model, which was consistent with the previous reported value through DFT calculations.[31] We can easily expect a NP catalyst better than commercial Pt NP should possess an Eo in the range of 0.1-0.3 eV (0.2 eV is the

optimal value). Our fcc-FePt/Pt and fct-FePt/Pt both fall into this regime. As the E_O value of the fct-FePt/Pt is closer to the optimal value of 0.20 eV, the fct-FePt/Pt shows higher ORR activity than the fcc-FePt/Pt.

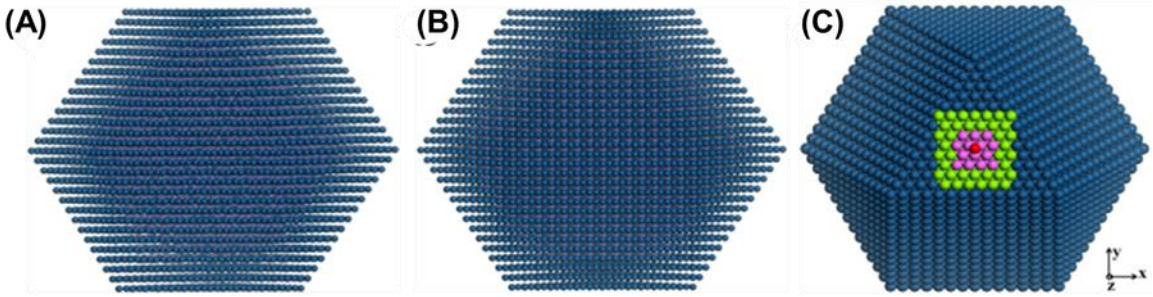

Figure 6.2.13 8 nm cuboctahedral fcc-FePt/Pt (A) and fct-FePt/Pt (B) core/shell models constructed for QM-MM calculations. The model (A) contains 7667 Pt atoms and 2512 Fe atoms, and the model (A) consists of 7704 Pt atoms and 2405 Fe atoms. Both models have a core composition of $Fe_{50}Pt_{50}$ and a shell of three-atomic-layer Pt. (C) Atomic configuration of a cuboctahedron NP for QM-MM calculation, viewing along <111> direction. The entire system is partitioned into a QM region (red, pink and green spheres), and an MM region (blue spheres).

E_O is related to the compression (or stretch) of Pt (i.e. Pt strain) on the catalyst surface.[32] In our FePt/Pt core/shell structure this strain is caused by the crystal lattice mismatch between the core and the shell. Using the supercell models (Figure 6.1) and DFT, we calculated the equilibrium crystalline lattice constants (Table 6.2) and the surface Pt strain (ε) of the fcc- and fct-FePt/Pt and compared them with fcc-Pt (Table

6.3). Both fcc- and fct-FePt have smaller lattice constants than Pt and the corresponding surface Pt strains are in 3% - 5%, higher than 2.3% required for the optimal E_O (0.20 eV).[33] When the fcc-FePt serves as a core, the surface Pt is slightly over-compressed (E_O=0.26 eV). But when fcc-FePt transforms to fct-FePt in the core, the interplanar distance of the core expands in [100]/[010] directions and shrinks in [001] direction. The overall effect is to relieve the over-compression on the Pt surface, resulting in a better E_O and higher activity for ORR.

Materials	$a_{[100]}/a_{Pt}$	$a_{[010]}/a_{Pt}$	$a_{[001]}/a_{Pt}$
fcc-$Fe_{50}Pt_{50}$	0.961	0.964	0.965
fct- $Fe_{50}Pt_{50}$	0.971	0.971	0.945

Table 6.2 Crystalline lattice constants of FePt based on DFT calculations. a_{Pt} is the lattice constant of *fcc*-Pt. $a_{[100]}$, $a_{[010]}$, $a_{[001]}$ are the calculated interplanar distances along [100], [010] and [001] directions of each material.

Catalyst	$\varepsilon_{[100]}$	$\varepsilon_{[010]}$	$\varepsilon_{[001]}$	E_O (eV)
fcc-FePt/Pt	3.9%	3.6%	3.5%	0.26
fct-FePt/Pt	2.9%	2.9%	5.5%	0.23

Table 6.3 Surface strain ε from DFT calculations and E_O from QM-MM simulations. Compressive strain is calculated by $\varepsilon_i = (a_{Pt}-a_i)/aPt$, where i indicates [100], [010]

and [001] directions. a_{Pt} is the lattice constant of fcc-Pt. a_i is the interplanar distance along i direction of each core material.

6.4 Conclusion

We have demonstrated a new strategy to tune core/shell FePt/Pt NP catalysis by controlling core structure and shell strain. The FePt/Pt NPs are synthesized by electro-anodization of the FePt alloy NPs. The core FePt structure is controlled to be fcc or fct and the shell is in ~3 atomic layer thick. The fct-FePt/Pt NPs show much high activity for ORR than the fcc-FePt/Pt ones and the QM-MM simulations reveal that this activity enhancement is due to the release of over-compressed Pt strain and to the improvement of Pt-O binding energy from 0.26 eV to 0.23 eV. This strain-tuning strategy can potentially be extended to other multimetallic alloy systems, providing a novel approach to rational tuning of NP catalytic efficiency for many chemical reactions.

References

1. S. Guo, S. Zhang, S. Sun, *Angew. Chem. Int. Ed.* **2013**, *52*, 2-21.

2. W. Yu, M. D. Porosoff, J. G. Chen, *Chem. Rev.* **2012**, *112*, 5780-5817.

3. V. R. Stamenkovic et al., *Nat. Mater.* **2007**, *6*, 241 - 247.

4. C. Wang, H. Daimon, T. Onodera, T. Koda, S. Sun, *Angew. Chem. Int. Ed.* **2008**, *47*, 3588-3591.

5. M. Mavrikakis, B. Hammer, J. K. Norskov, *Phys. Rev. Lett.* **1998**, *81*, 2819-2822.

6. A. Nilsson, L. G. M. Pettersson, J. K. Norskov, *Chemical bonding at surfaces and interfaces*. **2008**, Elsevier, Amsterdam.

7. P. Strasser *et al.*, *Nat. Chem.* **2010**, *2*, 454-460.

8. J. K. Norskov *et al.*, *J. Phys. Chem. B* **2004**, *108*, 17886-17892.

9. H. Wang, Y. Guo, G. Lu, P. Hu, *J. Chem. Phys.* **2009**, *130*, 224701-224706.

10. V. R. Stamenkovic, *et al.*, *Angew. Chem. Int. Ed.* **2006**, *45*, 2897-2901.

11. S. Zhang, S. Guo, H. Zhu, D. Su, S. Sun, *J. Am. Chem. Soc.* **2012**, *134*, 5060-5063.

12. H. Chen, *et al.*, *J. Am. Chem. Soc.* **2012**, *134*, 18453-18459.

13. S. Sun, C. B. Murray, D. Weller, L. Folks, A. Moser, *Science* **2000**, *287*, 1989-1992.

14. J. Kim, C. Rong, J. P. Liu, S. Sun, *Adv. Mater.* **2009**, *21*, 906-909.

15. Q. Zhao, R. G. Parr, *J. Chem. Phys*. **1993**, *98*, 543-548.

16. Q. Zhao, R. C. Morrison, R. G. Parr, *Phys. Rev.* **1994**, *A* 50, 2138-2142.

17. Q. Wu, T. V. Voorhis, *Phys. Rev.* **2005**, *A* 72, 024502-024505.

18. X. Zhang, G. Lu, W. A. Curtin, *Phys. Rev.* **2013**, *B* 87, 054113-054122.

19. G. Kresse, J. Hafner, *Phys. Rev.***1993**, *B* 47, 558-561.

20. G. Kresse, J. Furthmuller, *Phys. Rev.* **1996,** *B 54*, 11169-11186 (1996).

21. Blochl, P. E. *Phys. Rev.* **1994,** *B* 50, 17953-17979.

22. X. W. Zhou, R. A. Johnson, H. N. G. Wadley, *Phys. Rev.* **2004,** *B 69*, 144113-144122.

23. H. J. Monkhorst, J. D. Pack, *Phys. Rev.***1976**, *B 13*, 5188-5192.

24. J. Kim, C. Rong, J. P. Liu, S. Sun, *Adv. Mater.* **2009**, *21*, 906-909.

25. A. V. Crewe, J. Wall, J. Langmore, *Science* **1970**, *168*, 1338-1340.

26. S. Guo, S. Zhang, D. Su, S. Sun, *J. Am. Chem. Soc.* **2013**, *135*, 13879-13884.

27. X. Zhang, G. Lu, W. A. Curtin, *Phys. Rev. B* **2013**, *87*, 054113-054122.

28. N. S. Froemming, G. Henkelman, *J. Chem. Phys.* **2009**, *131*, 234103-234109.

29. X. Zhang, G. Lu, *J. Phys. Chem. Lett.* **2014**, *5*, 292–297.

30. W. Tang, G. Henkelman, *J. Chem. Phys.* **2009**, *130*, 194504-194509.

31. L. Li, A. H. Larsen, N. A. Romero, V. A. Morozov, C. Glinsvad, F. Abild-Pedersen, J. Greeley, K. W. Jacobsen, J. K. Nørskov, *J. Phys. Chem. Lett.* **2013**, *4*, 222-226.

32. M. Mavrikakis, B. Hammer, J. K. Norskov, *Phys. Rev. Lett.* **1998**, *81*, 2819-2822.

33. A. Nilsson, L. G. M. Pettersson, J. K. Norskov, *Chemical bonding at surfaces and interfaces*. Elsevier, Amsterdam, **2008**.

Chapter 7

Monodisperse $M_xFe_{3-x}O_4$ (M = Fe, Cu, Co, Mn) Nanoparticles and Their Electrocatalysis for Oxygen Reduction Reaction

7.1 Background and Introduction

As we illustrated in Chapter 1-6, promoting oxygen reduction reaction (ORR) at cathode is an important step towards building fuel cells or metal-air batteries into highly efficient energy conversion devices.[1, 2] Ideally, ORR can occur at theoretical thermodynamic electrochemical potentials. In reality, however, ORR is observed always at a more negative potential due to the difficulty in O_2 adsorption on electrode surface and O-O bond activation/cleavage. To lower this over-potential, an active and robust catalyst must be present. Among different catalysts tested, metallic Pt-based catalysts are proven to be the most efficient catalyst for ORR in either acid or alkaline media.[3-8] Consequently, various forms of catalysts based on Pt nanoparticles (NPs), such as examples given in Chapter 3-6, have been fabricated and studied for applications in practical energy devices. One of the most challenging issues encountered in pursuing the commercialization of Pt-based energy devices is the high cost associated with the heavy use of Pt – an expensive metal with limited natural supply. It has become increasingly clear that for the fuel cell or metal-air battery design to become a reality, the use of Pt must be minimized, or even better, robust non-Pt catalysts with their catalytic efficiency close to Pt are developed. Although Pt catalysts constantly outperforms the non-Pt catalysts in ORR catalysis, especially when commercially more relevant acid media are used, recent search has demonstrated that Au- or Pd-based NPs can function as a Pt-alternative to catalyze ORR in alkaline media.[9-10] More interestingly, when graphene or carbon nanotube is

used as a support, some early transition metal oxide NPs, including Co_3O_4 and Mn_3O_4 NP, can exhibit the promising ORR activity in alkaline media.[11-16] But their activity drops significantly when these NPs are supported on conventional carbon supports.[17,18]

Here we report that M(II)-substituted magnetite $M_xFe_{3-x}O_4$ supported on conventional carbon support are catalytically active for ORR and $MnFe_2O_4$ NPs even outperform the commercial Pt NP catalyst in catalyzing ORR in 0.1 M KOH solution. Like Fe_3O_4 ($FeO•Fe_2O_3$), M(II)-substituted magnetite $M_xFe_{3-x}O_4$ ($M_xFe_{1-x}O•Fe_2O_3$) have a common inverse spinel structure in which O's form the face centered cubic (fcc) packing with M(II) occupying the octahedral (O) interstitial sites and Fe(III) distributed evenly in the O and tetrahedral (T) sites.[19,20] Such a structure has shown good electrical conductivities due to the electron hopping between different valence states of metals in O-sites,[21-23] and should also provide necessary surface redox active metal centers for O_2 adsorption and activation.[23] To perform the study, we synthesized a series of $M_xFe_{3-x}O_4$ NPs with M = Fe, Cu, Co, Mn and NP sizes controlled less than 8 nm. Loaded on commercial carbon support, these $M_xFe_{3-x}O_4$ NPs show the M(II)-dependent ORR catalytic activities in 0.1 M KOH solution with MnxFe3-xO4 being the most active followed by $Co_xFe_{3-x}O_4$, $Cu_xFe_{3-x}O_4$, and Fe_3O_4. The ORR activity of the $Mn_xFe_{3-x}O_4$ could be further tuned by the composition x, and $MnFe_2O_4$ NPs were found to be the most active catalyst with their catalysis comparable to the commercial Pt NP catalyst in catalyzing ORR in 0.1 M KOH

solution. The $MnFe_2O_4$ NPs represent a new class of non-Pt catalysts for catalyzing ORR in alkaline media.

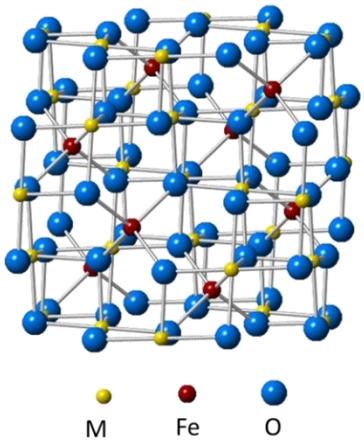

Figure 7.1 Schematic illustration of crystal structure of inverse spinel.

7.2 Experimental

Chemicals and Materials

$Fe(acac)_3$, $Cu(acac)_2$, $Co(acac)_2$, $Mn(acac)_2$ (acac = acetylacetonate), oleylamine (OAm, >70%), oleic acid (OA), benzyl ether (BE, >98%), 1,2-tetradecanediol, hexane, ethanol and Nafion (5%) were all purchased from Sigma Aldrich. C-Pt catalyst (20% mass loading with Pt particle diameter of 2.5-3.5 nm) was obtained from Fuel Cell Store.

Characterization

TEM and HRTEM samples were prepared by depositing a drop of diluted nanoparticle (NP) dispersion in hexane on amorphous carbon coated copper grids.

TEM images were obtained from a Philips CM 20 operating at 200 kV. High-resolution TEM (HRTEM) images were obtained from a JEOL 2010 with an accerating voltage of 200 kV. X-ray diffraction (XRD) patterns of the NPs were collected from a Bruker AXS D8-Advanced diffractometer with Cu Kα radiation (λ =1.5418 Å). Metal components within NPs were analyzed by inductively coupled plasma-atomic emission spectroscopy (ICP-AES) on a JY2000 Ultrace ICP Atomic Emission Spectrometer equipped with a JY AS 421 autosampler and 2400g/mm holographic grating, and the mass ratios were converted into atomic ratios. Electrochemical measurements were carried out on a Autolab potentiostat from Metrohm Instrument Company (Autolab 302). A three-electrode system consisting of a glassy carbon (GC) working electrode (5-mm in diameter), an Ag/AgCl reference electrode (in 4 M KCl) and a platinum wire counter electrode, was used. Magnetic properties were measured on a Lakeshore 7404 high sensitivity vibrating sample magetometer (VSM) with fields up to 1.5 T.

Synthesis of $M_xFe_{3-x}O_4$ NPs (M=Fe, Cu, Co, Mn)

A solution of 25 ml BE, 0.96 ml OA, 1 ml OAm, 1.15 g 1,2-tetradecandiol and 1 mmol $Fe(acac)_3$ in a four-necked flask was heated to 120 ^oC under nitrogen flow and magnetic stirring and was kept at this temperature for 1 h. The solution was heated up to 210 ^oC at a rate of 8 ^oC/min and kept at this temperature for 2 h. Under a blanket of nitrogen atmosphere and at a slow heating rate (3 ^oC/min), the solution was further heated up to 300 ^oC and kept at this temperature for 1 h. After cooled down to room

temperature, the NPs were collected and washed by addition of ethanol (20 ml) and subsequent centrifugation at 10000 rpm for 8 min. The product was redispersed into hexane and precipitated out by addition of ethanol and centrifugation to remove all residual impurities. Final product, 7 nm Fe_3O_4 NPs, was dispersed in hexane for further use.

Similarly, other $M_xFe_{3-x}O_4$ NPs with M = Cu, Co, or Mn were synthesized by adding 0.5 mmol $Cu(acac)_2$/$Co(acac)_2$/$Mn(acac)_2$ in the beginning of the reaction. Specifically, 5 nm $Mn_xFe_{3-x}O_4$ NPs with different x were synthesized by varying the amount of $Mn(acac)_2$, OA and OAm. To synthesize $Mn_{0.4}Fe_{2.6}O_4$ NPs, 0.35 mmol $Mn(acac)_2$, 1 ml OA and 1.1 ml OAm were added in the reaction mixture. To prepare $MnFe_2O_4$ NPs, 0.67 mmol $Mn(acac)_2$, 0.92 ml OA and 1 ml OAm were added.

Catalyst Peraparation

The as-synthesized NPs were mixed with Ketjen-300 J carbon with a ratio of 4:6 by weight in 20 ml mixture of hexane and acetone (V/V=1:1) and followed by 1 h sonication to load NPs on carbon. The C-NPs were separated from the solvents by centrifugation and annealed in air at 165 ^oC for 12 h to remove the surfactant. This annealing treatment caused no NP aggregation or structure change. The C-NPs were dispersed in a mixture of deionized water, isopropanol and Nafion (V/V/V=4/1/0.05) to form a catalyst ink (2mg/ml) for electrochemistry measurements.

GC electrode was polished by 0.1 μm and 0.05 μm alumina powder and rinsed with deionized water, followed by sonication first in ethanol and then in deionized water.

20 µl catalyst ink was deposited on the GC working electrode and dried at ambient condition.

Electrochemical Measurements

Cyclic voltammograms (CVs) were obtained by scaning between 0.2 V to -0.8 V vs Ag/AgCl at a scan rate of 50 mV/s in N_2-saturated 0.1 M KOH solution. CVs were also obtained by scaning between 0 V to -0.8 V vs Ag/AgCl at a scan rate of 50 mV/s in O_2-saturated 0.1 M KOH solution. ORR polarization curves were obtained by linear sweep voltammetry scanning from 0.2 V to -0.8 V vs Ag/AgCl at a scan rate of 10 mv/s in O2-saturated 0.1 M KOH with RDE at different rpms (400-2500 rpm). Chronoamperometric was performed to evaluate the catalyst durability at -0.3 V vs Ag/AgCl with the electrode rotating at 200 rpm in O_2-saturated 0.1 M KOH. The electron transfer number (n) was calculated from the slopes of the Koutecky-Levich plots according to:

$$\frac{1}{I} = \frac{1}{I_L} + \frac{1}{I_K} = \frac{1}{I_K} + \frac{1}{B\omega^{1/2}}$$

$$B = 0.62nAFC_{O_2} D_{O_2}^{2/3} \nu^{-1/6}$$

where I, I_K and I_L are measured current, kinetic current and diffusion-limiting current respectively, ω is the angular velocity, F is the Faraday constant (96485 C mol^{-1}), A is the electrode surface area, CO_2 is the concentration of dissolved O_2 (1.2×10^{-6} mol cm^{-3}) , DO_2 is the diffusion coefficient of O_2 (1.9×10^{-5} cm^2 s^{-1}) and υ is kinetic viscosity of the electrolyte (0.01cm^2 s^{-1}). The constant 0.62 is applied when the rotation speed is expressed in radius per second (rad/s).

7.3 Results and Dissuction

7.3.1 Synthesis of $M_xFe_{3-x}O_4$ NPs (M=Fe, Cu, Co, Mn)

$M_xFe_{3-x}O_4$ NPs were synthesized by thermal decomposition of $Fe(acac)_3$ and $Cu(acac)_2$, or $Co(acac)_2$, or $Mn(acac)_2$ in benzyl ether, which was modified from a previous method.[24,25] 1,2-tetradecanediol was used as a mild reducing agent to reduce $Fe(acac)_3$, and oleylamine and oleic acid were employed as stabilizers. In the synthesis, the composition of the NPs was controlled by varying the ratio of $M(acac)_2/Fe(acac)_3$ (see **Experimental**). According to the composition analysis by inductively coupled plasma atomic emission spectroscopy (ICP-AES), the NP obtained from $M(acac)_2/Fe(acac)_3$ = 1/2 show a M:Fe ratio of Cu:Fe = 22:78, Co:Fe = 27:73 and Mn:Fe = 20:80, corresponding to $Cu_{0.7}Fe_{2.3}O_4$, $Co_{0.8}Fe_{2.2}O_4$ and $Mn_{0.6}Fe_{2.4}O_4$ respectively in the product. Changing the amount of $M(acac)_2$ led to the formation of $M_xFe_{3-x}O_4$ NPs with different x. For instance, $Mn_{0.}4Fe_{2.6}O_4$, $Mn_{0.6}Fe_{2.4}O_4$, and $MnFe_2O_4$ NPs were prepared by controlling the Mn:Fe precursor ratios at 0.35, 0.5 and 0.67 (see Experimental). Transmission electron microscopy (TEM) images show that the as-synthesized magnetite Fe_3O_4 as well as Cu(II)-, Co(II)- and Mn(II)-substituted magnetite NPs were monodisperse with an average diameter of 7 ± 0.2, 8 ± 0.3, 5 ± 0.2 and 5 ± 0.2 nm respectively (Figure 7.2.1 and Figure 7.2.2). High resolution TEM (HRTEM) of the representative $MnFe_2O_4$ NPs shows the typical (111) lattice fringe distance of 0.22 nm (Figure 7.2.3), indicating

that the NP has the single crystalline fcc structure. The $MnFe_2O_4$ NP structure was further characterized by X-ray diffraction (XRD), as shown in Figure Figure 7.2.4. The diffraction pattern is similar to the bulk Fe_3O_4.

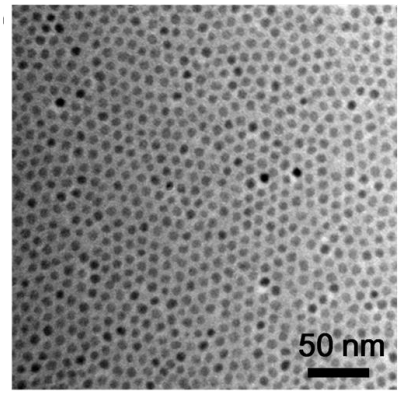

Figure 7.2.1 TEM image of the as-synthesized 5 nm $MnFe_2O_4$ NPs.

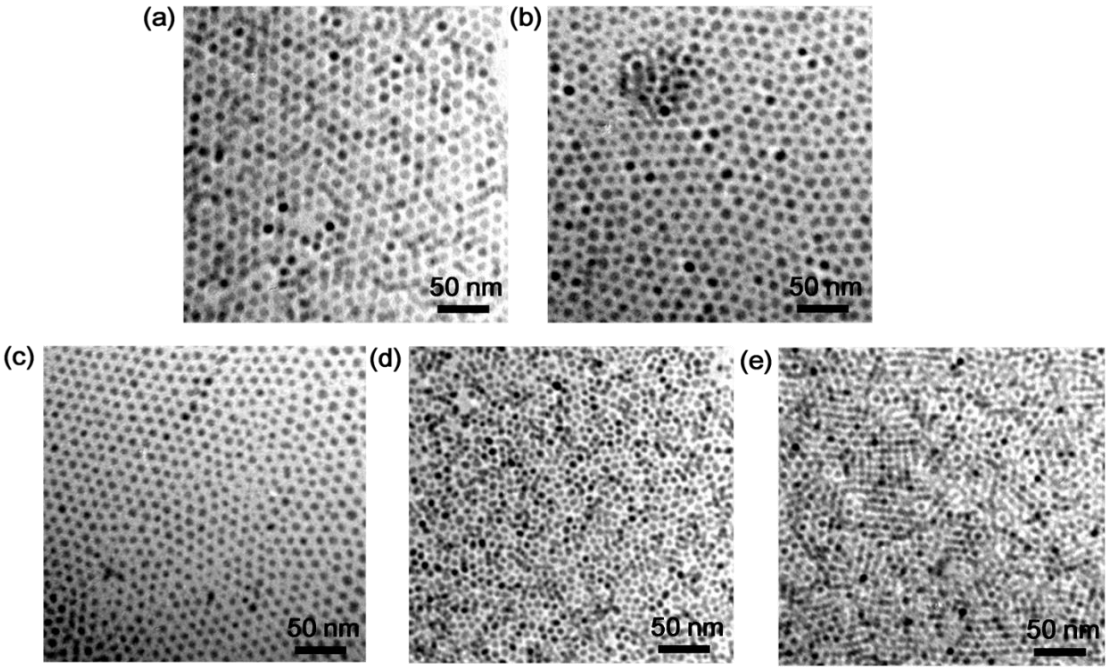

Figure 7.2.2 TEM images of the as-synthesized (a) 7 nm Fe_3O_4, (b) 8 nm $Cu_{0.7}Fe_{2.3}O_4$, (c) 5 nm $Co_{0.8}Fe_{2.2}O_4$ and (d) 5 nm $Mn_{0.4}Fe_{2.6}O_4$ NPs and (e) $Mn_{0.6}Fe_{2.4}O_4$ NPs.

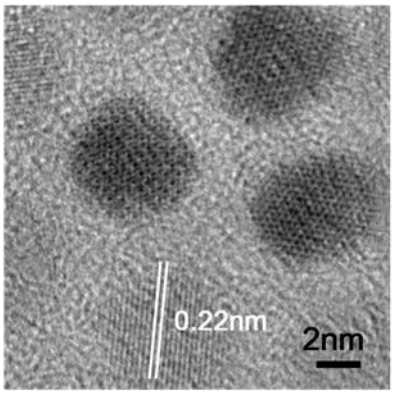

Figure 7.2.3 HRTEM image of the $MnFe_2O_4$ NPs.

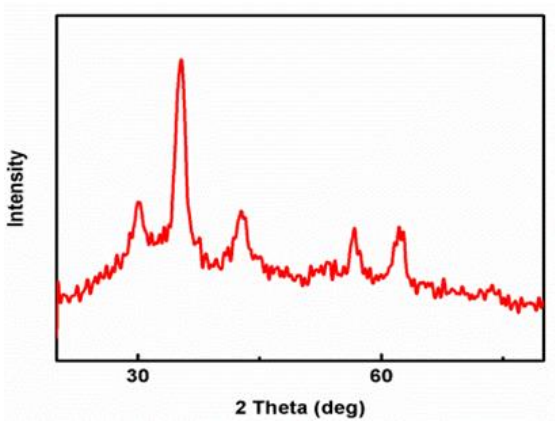

Figure 7.2.4 XRD pattern of the $MnFe_2O_4$ NPs.

The $MnFe_2O_4$ NPs are superparamagnetic at room temperature (Figure 7.2.5a). Among three different kinds of $Mn_xFe_{3-x}O_4$ NPs studied, the larger the x value, the higher the magnetic moment (Figure 7.2.5b). This is consistent with the magnetism observed from the inverse spinel structure, in which two Fe^{3+} are antiferromagnetically coupled and magnetic moment of the ferrite structure is mostly

decided by the spins of d-electrons in M^{2+}. In the octahedral interstitial site, Mn^{2+} (d^5) have more parallel spins than Fe^{2+} (d^6), and therefore, the increase of Mn in $Mn_xFe_{3-x}O_4$ leads to higher magnetic moments.

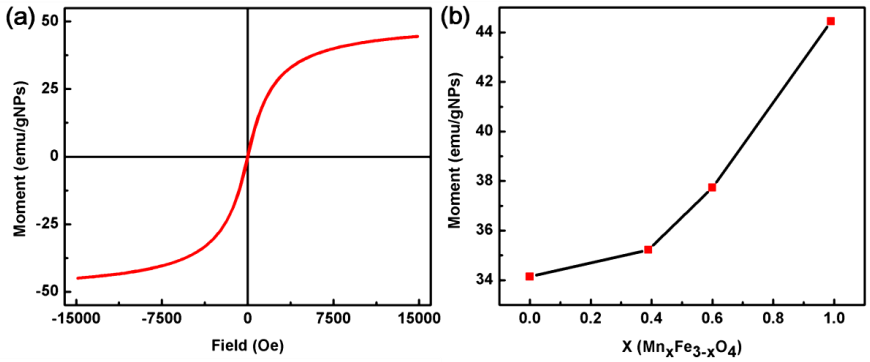

Figure 7.2.5 (a) Hysteresis loop of the $MnFe_2O_4$ NPs measured at room temperature; (b) magnetic moment change vs. x in $Mn_xFe_{3-x}O_4$ NPs.

7.3.2 Catalytic Properties of $Mn_xFe_{3-x}O_4$ NPs (M=Fe, Cu, Co, Mn)

To study NP electrocatalysis towards ORR, we loaded the NPs on Ketjan carbon (C) with a weight ratio of 4:6 (NPs:C) through sonication of the NP dispersion and C in hexane and acetone (V/V=1:1). The C-NPs were activated via thermal annealing under air atmosphere at 165 °C for 12 h (see **Experimental**). The representative TEM images (Figure 7.2.6 and Figure 7.2.7) and XRD patterns (Figure 7.2.8) reveal that these NPs were uniformly deposited on C and preserved their morphology and crystalline structure in the loading-annealing process.

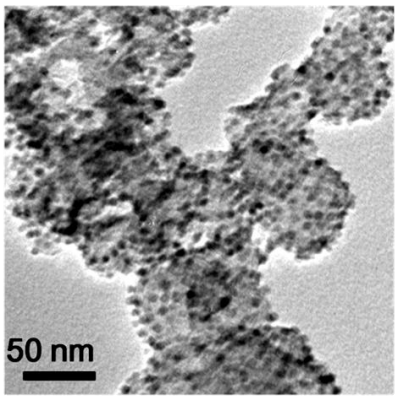

Figure 7.2.6 TEM image $MnFe_2O_4$NPs on carbon after air annealing at 165 ^oC for 12h.

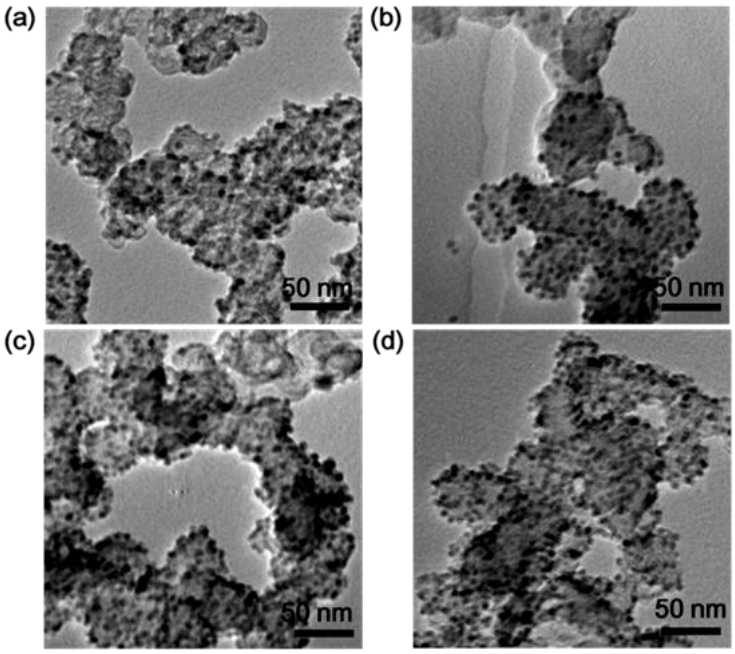

Figure 7.2.7 TEM images of (a) Fe_3O_4, (b) $Cu_{0.7}Fe_{2.3}O_4$, (c) $Co_{0.8}Fe_{2.2}O_4$, (d) $Mn_{0.6}Fe_{2.4}O_4$ NPs on carbon after air annealing at 165 ^oC for 12 h.

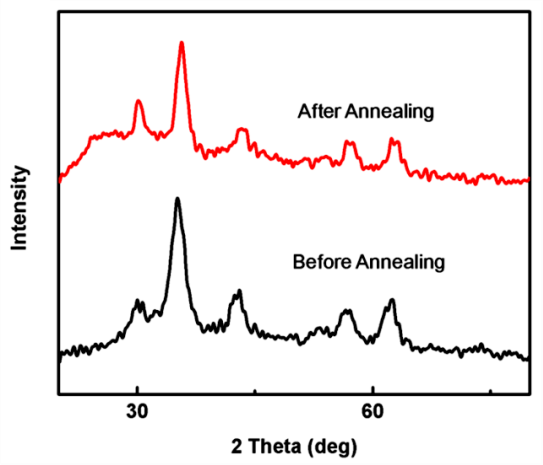

Figure 7.2.8 XRD of the $MnFe_2O_4$ NPs before and after air annealing at 165 ^oC in air.

The C-NPs were dispersed in the deionized water + isopropanol + 5% Nafion (v/v/v = 4/1/0.05) with a concentration of 2 mg/mL, 20 µL of which was deposited on the glassy carbon (GC) rotating disk electrode (RDE) for electrochemical characterization. We first studied the M(II) effect in NP electrocatalytic activity. Figure 7.2.9 shows the cyclic voltammograms (CVs) of the C-Fe_3O_4 and C-$MnFe_2O_4$ in O_2-saturated 0.1 M KOH aqueous solution. CV's of the Cu(II)- and Co(II)-substituted magnetite NPs are given in Figure 7.2.10. From these CV's, we can see a large positive shift of the onset reduction potential with the peak appearing at -0.340V (Fe_3O_4) and -0.210V ($MnFe_2O_4$) respectively (Figure 7.2.9) while the peak potentials of other ferrite NPs appearing in between (Figure 7.2.10). This suggests that O_2 is most easily reduced on $MnFe_2O_4$ NP surface.

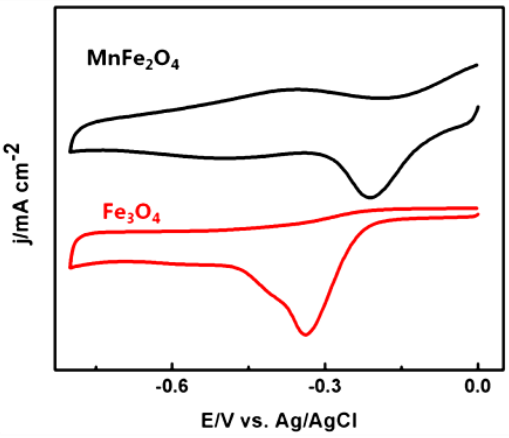

Figure 7.2.9 CVs of Fe_3O_4 and $MnFe_2O_4$ NPs in O_2-saturated 0.1 M KOH solution at a scan rate of 50 mV/s.

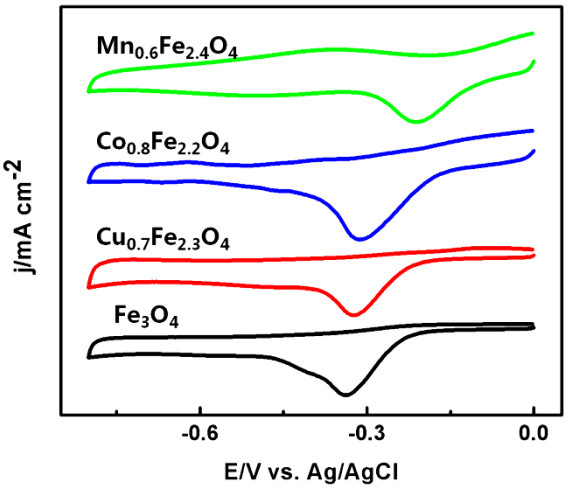

Figure 7.2.10 CV's of the Fe_3O_4 $Cu_{0.7}Fe_{2.3}O_4$, $Co_{0.8}Fe_{2.2}O_4$ and $Mn_{0.6}Fe_{2.4}O_4$ NPs in O_2-saturated 0.1 M KOH at a scan rate of 50 mV/s.

Rotating-disk electrode (RDE) measurements were further carried out to reveal the ORR kinetics of these NPs (see Experimental). Figure 7.2.11-7.2.13 show the ORR

polarization curves of Fe_3O_4 and $MnFe_2O_4$ as well as $Cu_{0.7}Fe_{2.3}O_4$ and $Co_{0.8}Fe_{2.2}O_4$ NP catalysts at different rotation rates. At 1600 rpm, Fe_3O_4 NPs have the half-wave potentials at -0.342 V, while $MnFe_2O_4$ NPs show a positively shifted half-wave potential at -0.154 V ($Cu_{0.7}Fe_{2.3}O_4$ and $Co_{0.8}Fe_{2.2}O_4$ NPs have the half-wave potentials at -0.319 V and -0.244 V respectively). The ORR kinetics was studied by Koutecky-Levich plots (insets of Figures 7.2.11-7.2.13). The linear plots suggest the first order reaction kinetics towards O_2 on NPs from -0.4 V to - 0.7 V. The separation of the K-L plots for Fe_3O_4 indicated a less completed kinetics comparing with $MnFe_2O_4$ in the same potential region. The number (n) of electrons transferred on Fe_3O_4, $MnFe_2O_4$ as well as on Cu- and Co-ferrite NPs was calculated (see SI) to be ~3.83 and ~4.18 respectively (~3.84 for Cu- and ~3.99 for Co-ferrite NPs), demonstrating a $4e^-$ oxygen reduction process from each of these NP catalysts. This is also similar to that obtained from the commercial C-Pt (n = 4) catalyst measured in the same condition.[8,9]

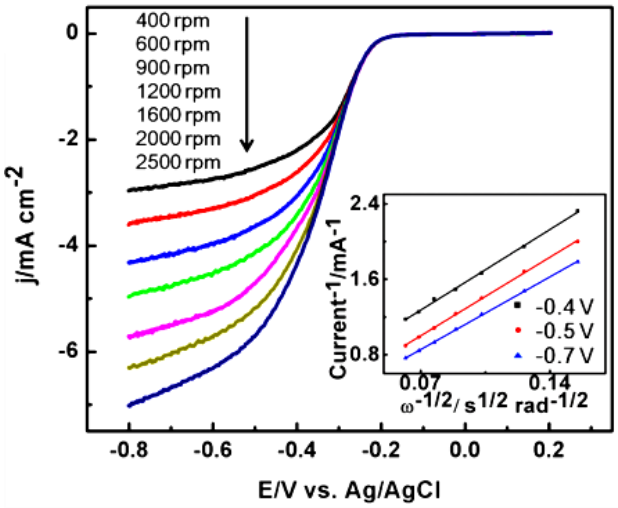

Figure 7.2.11 ORR polarization curves of Fe_3O_4 NPs at different rpm (400 rpm -2500 rpm) in O_2-saturated 0.1 M KOH at a scan rate of 10 mV/s. Insets: Koutecky-Levich plots at different potentials (-0.4 V, -0.5 V and -0.7 V).

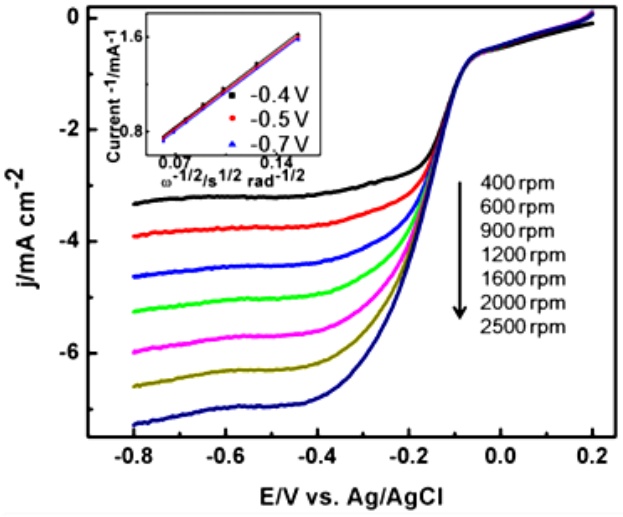

Figure 7.2.12 ORR polarization curves of $MnFe_2O_4$ NPs at different rpm (400 rpm -2500 rpm) in O_2-saturated 0.1 M KOH at a scan rate of 10 mV/s. Insets: Koutecky-Levich plots at different potentials (-0.4 V, -0.5 V and -0.7 V).

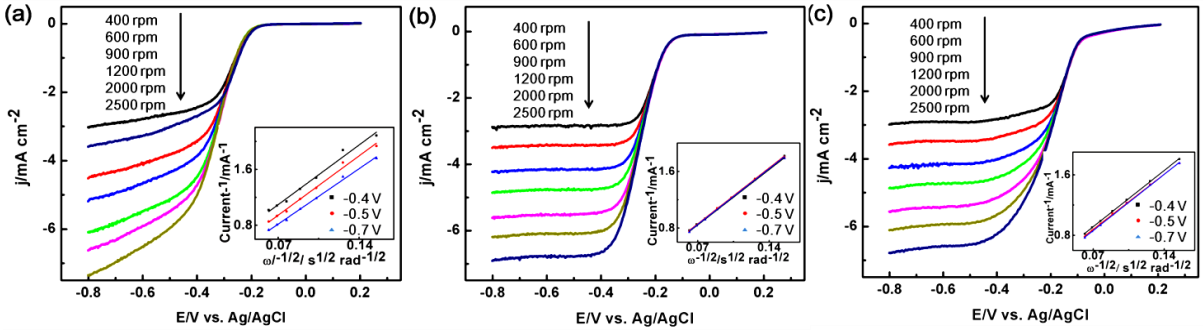

Figure 7.2.13 ORR polarization curves of (a) $Cu_{0.7}Fe_{2.3}O_4$, (b) $Co_{0.8}Fe_{2.2}O_4$ and (c) $Mn_{0.6}Fe_{2.4}O_4$ NPs at different rpm (400 rpm -2500 rpm) in O_2-saturated 0.1 M KOH at a scan rate of 10 mV/s. Insets: Koutecky-Levich plots at different potentials (-0.4 V, -0.5 V and -0.7 V).

To understand why the $MnFe_2O_4$ NPs have such a high activity, we studied the redox properties of the $M_xFe_{3-x}O_4$ in N_2-saturated 0.1 M KOH. Figure 7.2.14 shows the typical CVs of these NP catalysts. We can see that only $Mn_{0.6}Fe_{2.4}O_4$ NPs show a pair of redox peaks in the range of -0.077 V to 0.062 V, corresponding to the redox of Mn(III)/Mn(II), that occurs at the potential more positively than that for ORR. Compared with other M(II) described here, Mn(II) has a higher tendency to adsorb O_2 and to transfer electrons to O_2, regenerating Mn(III).[22,26] This may explain why $Mn_xFe_{3-x}O_4$ NPs are much more active than any other $M_xFe_{3-x}O_4$ reported in catalyzing ORR.

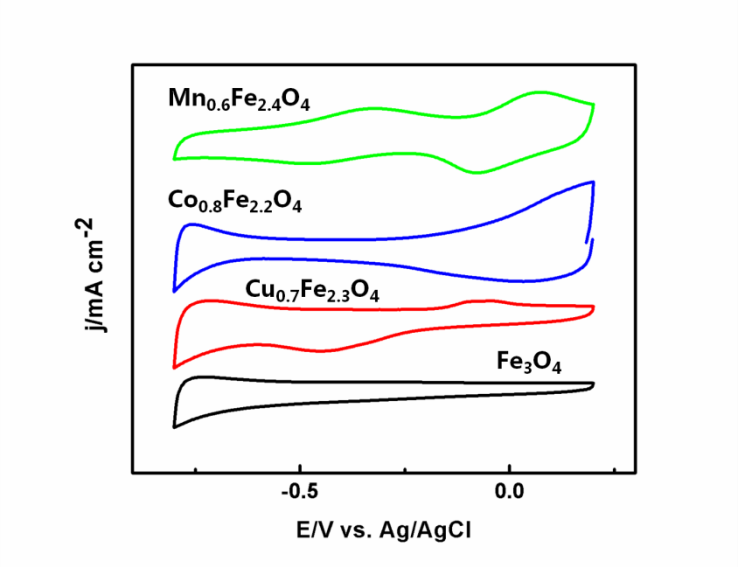

Figure 7.2.14 CV's of the Fe_3O_4 $Cu_{0.7}Fe_{2.3}O_4$, $Co_{0.8}Fe_{2.2}O_4$ and $Mn_{0.6}Fe_{2.4}O_4$ NPs in N_2-saturated 0.1 M KOH at a scan rate of 50 mV/s.

We also studied the composition-dependent electrocatalytic properties of the C-$Mn_xFe_{3-x}O_4$ NPs. CVs of the C-$Mn_xFe_{3-x}O_4$ NPs with different x in N_2-saturated 0.1 M KOH (Figure 7.2.15a) show that the redox peaks of Mn(III)/Mn(II) in the range of -0.077 V to 0.062 V increase with more Mn(II) present in $Mn_xFe_{3-x}O_4$ NPs. A pair of weak redox peaks in the region of -0.45V to -0.52V may be related to Mn(II)/Mn(0). Figure 7.2.15b shows the ORR polarization curves of these $Mn_xFe_{3-x}O_4$ NPs measured in O_2-saturated 0.1 M KOH. With the increase in x, both ORR onset and half-wave potentials are shifted positively and the background I-V curve shows a downward slope from 0.2 V to -0.08 V. This slope relates to the valence change from Mn(III) and Mn(II). ORR polarization curves (Figure 7.2.15c)

indicate that the $MnFe_2O_4$ NPs have the best ORR activity with the half-wave potential at -0.154 V, close to that from the commercial Pt. Tafel plot (inset of Figure 7.2.15c) also confirms that $MnFe_2O_4$ and the commercial Pt catalysts have very similar kinetic behaviors and kinetic current densities, especially in the low overpotential region.

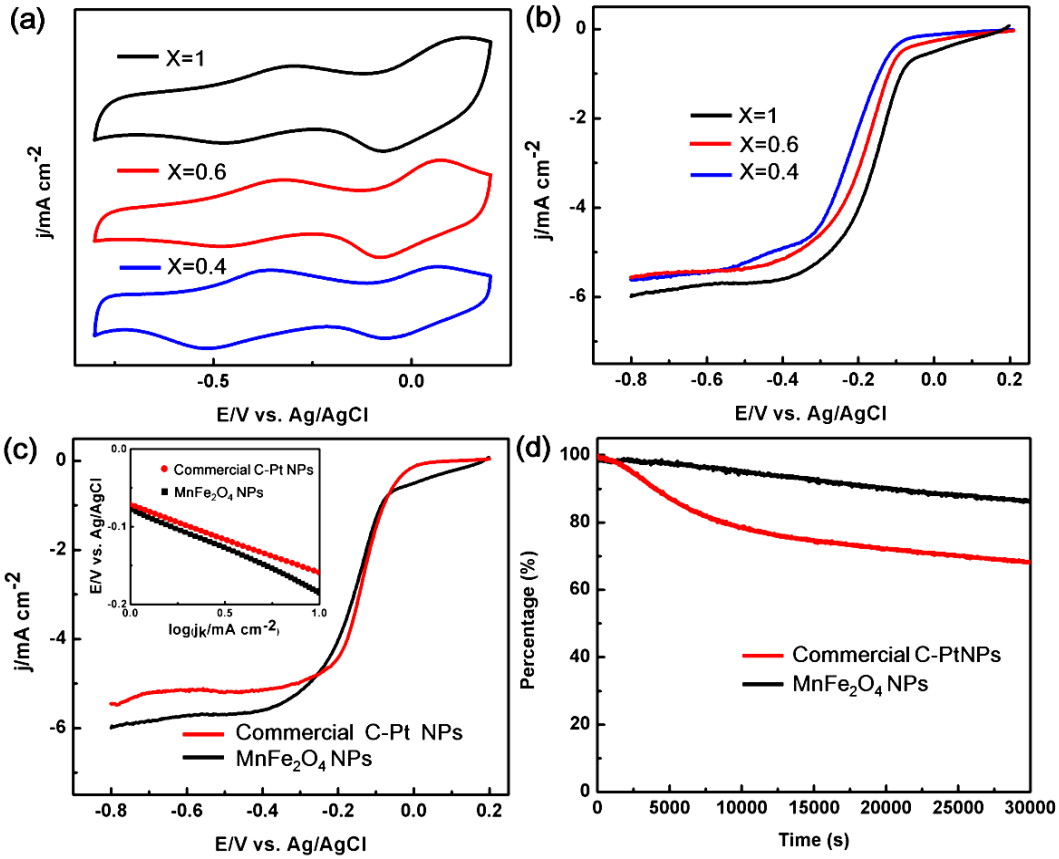

Figure 7.2.15 (a) CVs of $Mn_xFe_{3-x}O_4$ NPs with different x in N_2-saturated 0.1 M KOH electrolyte at a scan rate of 50 mV/s. (b) ORR polarization curves of $Mn_xFe_{3-x}O_4$ NPs with different x at 1600 rpm in O2-saturated 0.1 M KOH electrolyte at a scan rate of 10 mV/s. (c) ORR polarization curves for $MnFe_2O_4$ NPs and

commercial C-Pt NPs at 1600 rpm in O_2-saturated 0.1 M KOH electrolyte at a scan rate of 10mV/s (inset are Tafel plots at low over potentials). (d) Current percentage-time curves obtained from chronoamperometric method at -0.3 V in O_2-saturated 0.1 M KOH at 200 rpm.

The stability of the C-$MnFe_2O_4$ NPs was tested by chronoamperometric test at -0.3 V and compared with the commercial C-Pt NP catalyst. As shown in Figure 7.2.15d, the C-$MnFe_2O_4$ catalyst shows a much slower current decay than the commercial C-Pt catalyst. After a 9-h test, the current density measured from the C-$MnFe_2O_4$ still has 87% of its initial current density while that from the commercial C-Pt drops to 61%. The poor stability of the commercial C-Pt arises likely from the formation of Pt-OH on the catalyst surface,[27] which may be facilitated by the use of KOH as the electrolyte. As a comparison, the C-$MnFe_2O_4$ NPs already have the Mn-O on the NP surface and the presence of KOH can further increase their stability in solution during the test. Our tests infer that the C-$MnFe_2O_4$ catalyst has a better long-term stability than the commercial C-Pt catalyst in 0.1 M KOH solution.

7.4 Conclusion

In summary, we have synthesized a series of M(II)-substituted magnetite $M_xFe_{3-x}O_4$ NPs with M = Fe, Cu, Co, Mn with x controlled up to 1. We studied their

electrochemical and electrocatalytic properties toward ORR in 0.1 M KOH solution. We found that these $M_xFe_{3-x}O_4$ NPs supported on conventional Ketjan carbon (C) support were active for ORR and their activity was dependent on the chemical nature of M(II). Due to the unique redox properties of Mn(III)/Mn(II) observed near ORR onset potential region, the C-$Mn_xFe_{3-x}O_4$ NPs showed much higher activity than any of the other $M_xFe_{3-x}O_4$ NPs, reaching the optimum value when x = 1. The C-$MnFe_2O_4$ NPs even outperformed the commercial C-Pt NP catalyst in catalyzing ORR in 0.1 M KOH. They represent a new class of non-precious metal NP catalyst for ORR in alkaline media and other energy conversion applications.

References

1. M. Winte, R. J. Brodd, *Chem. Rev*., 2004, *104*, 4245-4270.
2. A. A. Gewirth, M. S. Thorum, *Inorg. Chem.*, 2010, *49*, 3557-3566.
3. C. Wang, H. Daimon, T. Onodera, T. Koda, S. Sun, *Angew. Chem. Int. Ed*. 2008, *47*, 3588-3591.
4. C. Wang, H. Daimon, S. Sun, *Nano Lett*. 2009, *4*, 1493-1496.
5. V. Mazumder, M. Chi, K. L. More, S. Sun, *J. Am. Chem. Soc.* 2010, *132*, 7848-7849.
6. C. Wang, M. Chi, D. Li, D. Strmcnik, D. Vliet, G. Wang, V. Komanicky, K. Chang, A. P. Paulikas, D. Tripkovic, J. Pearson, K. L. More, N. M. Markovic, V. R. Stamenkovic, *J. Am. Chem. Soc*. 2011, *133*, 14396-14403.
7. H. Lee, S. E. Habas, S. Kweskin, D. Butcher, G. A. Somorjai, P. Yang, *Angew. Chem. Int. Ed.* 2006, *45*, 7824-7828.
8. V. R. Stamenkovic, B. S. Mun, M. Arenz, K. J. J. Mayrhofer, C. A. Lucas, G. Wang, P. N. Ross, N. M. Markovic, *Nat.Mater*. 2007, *6*, 241-247.
9. M. S. EI-Deab, T. Sotomora, T. Ohsaka, *Electrochem. Commun*. 2005, *7*, 29-34.
10. D. A. Slanac, W. G. Hardin, K. P. Johnston, K. J. Stevenson, *J. Am. Chem. Soc.* 2012, *134*, 9812-9819.
11. Y. Liang, Y. Li, H. Wang, J. Zhou, J. Wang, T. Regier, H. Dai, *Nat.Mater*. 2011, *10*, 780-786.

12. Y. Liang, H. Wang, P. Diao, W. Chang, G. Hong, Y. Li, M. Gong, L. Xie, J. Zhou, J. Wang, T. Regier, F. Wei, H. Dai, *J. Am. Chem. Soc.* 2012, *134*, 15849-15857.
13. J. Feng, Y. Liang, H. Wang, Y. Li, J. Zhang, J. Wang, T. Regier, H. Dai, *Nano Res.* 2012, *5*, 718-725.
14. Y. Liang, H. Wang, J. Zhou, Y. Li, J. Wang, T. Regier, H. Dai, H. *J. Am. Chem. Soc*. 2012, *134*, 3517-3523.
15. S. Guo, S. Zhang, L. Wu, S. Sun, *Angew. Chem. Int. Ed.* 2012, *51*, 11770-11773.
16. Z. Wu, S. Yang, Y. Sun, K. Parvez, X. Feng, K. Mullen, *J. Am. Chem. Soc*. 2012, *134*, 9082-9085.
17. Y. Wang, L. Cheng, F. Li, H. Xiong, Y. Xia, *Chem. Mater*. 2007, *19*, 2095-2101.
18. F. Cheng, Y. Su, J. Liang, Z. Tao, J. Cheng, *Chem. Mater.* 2010, *22*, 898-905.
19. J. Lee, Y. Huh, Y. Jun, J. Seo, J. Jang, H. Song, S. Kim, E. Cho, H. Yoon, J. Suh, J. Cheon, *Nat. Med*. 2007, *13*, 95-99.
20. Y. Jun, J. Seo, J. Cheng, *Acc. Chem. Res.* 2008, *41*, 179-189
21. E. Rios, J. Gautier, G. Poillerat, P. Chartier, *Electrochimica Acta*. 1998, *44*, 1491-1497.

22. V. Nebuvchilov, H. Wang, J. J. Martin, W. Qu, *J. Power. Sources.* **2010**, *195*, 1271-1291.

23. M. Hamdani, R. N. Singh, P. Chartier, P. *Int. J. Electrochem. Sci.* **2010**, *5*, 556-577.

24. S. Sun, H. Zeng, D. B. Robinson, S. Raoux, P. M. Rice, S. X. Wang, G. Li, *J. Am. Chem. Soc.* **2004**, *126*, 273-279.

25. H. Zeng, P. M. Rice, S. X. Wang, S. Sun, *J. Am. Chem. Soc.* **2004**, *126*, 11458-11459.

26. C. Choi, S. Park, S. Woo, Phys. *Chem. Chem. Phys.* **2012**, *14*, 6842-6848.

27. W. Jin, H. Du, S. Zheng, H. Xu, Y. Zhang, *J. Phys. Chem. B.* **2010**, *114*, 6542-6548.

Chapter 8

Controlled Synthesis of Au-MnO Nanocomposites for H_2O_2 Excellular Detection.

8.1 Background and Introduction

In Chapter 3-7, we have demonstrated several examples for NP catalysts for oxygen reduction reaction (ORR). Since H_2O_2 is an important intermediate during ORR, we can extend our system for H_2O_2 chemical conversion. H_2O_2 is an important reactive oxygen species generated in cells via oxygen metabolism and is involved actively in cell signaling and cell growth. However its uncontrolled over-production can cause detrimental oxidation of biomolecules and lead to aging, cancer and other diseases.[1] Therefore, being capable of monitoring H_2O_2 concentration levels associated with different cells is considered an important step towards understanding pathological, physiological and biomedical function of H_2O_2. Conventionally, H_2O_2 concentrations are measured by assays based on H_2O_2 reduction catalyzed by horseradish peroxidase (HRP).[2] Alternatively, the HRP-catalyzed H_2O_2 reduction reaction can be detected by electrochemical method as shown in Figure 8.1.1.[3,4] To improve detection sensitivity, HRP is often anchored on the surface of gold (Au) nanoparticles (NPs) that have been pre-deposited on the electrode to enrich HRP around the electrode surface area.[5] Despite the high sensitivity and selectivity achieved, this enzyme-based sensor is of very limited use due to the complications associated with HRP purification, immobilization and protection from denaturing. Recently, metal and metal oxide NPs that are active electrocatalysts for H_2O_2 reduction have been studied as enzyme-mimic sensors to detect H_2O_2 in various

environments.[6-7] Further studies indicate that the detection sensitivity can be improved by using composite NPs such as dumbbell-like Au-Fe_3O_4 or PtPd-Fe_3O_4.[8,9] Specifically, PtPd-Fe_3O_4 NPs have been used to detect H_2O_2 at nano-molar concentration (nM) level, and are applicable to monitor H_2O_2 released from RAW 264.7 cells (mouse leukemic monocyte macrophage cell line).[9]

Herein, we report new core/shell structured Au/MnO NPs as the sensitive catalyst for electrochemical detection of H_2O_2 with the detection sensitivity reaching nM, which is suitable for monitoring and quantifying H_2O_2 concentrations released from cells. Metal oxide, especially Mn-oxide NPs have been explored as biocompatible and enzyme-mimic catalyst for H_2O_2 detection.[7b-f] However, these oxide NPs are generally not as active as Pt-based NPs in catalyzing electrochemical reduction of H_2O_2 due most likely to their poor electron conductivity. One strategy to improve their detection sensitivity is to couple the Mn-O with metallic NPs so that synergistic effect can be applied to control both electron conductivity and catalytic activity. Among the common metal NPs studied, Au NPs come out as the best choice because Au is highly conductive and catalytically active for H_2O_2 reduction.[5,6a] More importantly, Au NPs are considered biocompatible.[5,10] We developed a unique approach to composite Au-MnO NPs by first preparing AuMn alloy NPs followed by air oxidation. We found that by controlling the AuMn compositions, Au-MnO NPs with different morphologies could be obtained, as illustrated in Figure 8.1.2. These

composite NPs were all active catalysts for electrochemical reduction of H_2O_2 and the core/shell Au/MnO NPs showed the best activity with the H_2O_2 detection limit reaching 8 nM. This high detection sensitivity allowed the quantification of H_2O_2 concentrations released from both non-tumorigenic and tumorigenic cells.

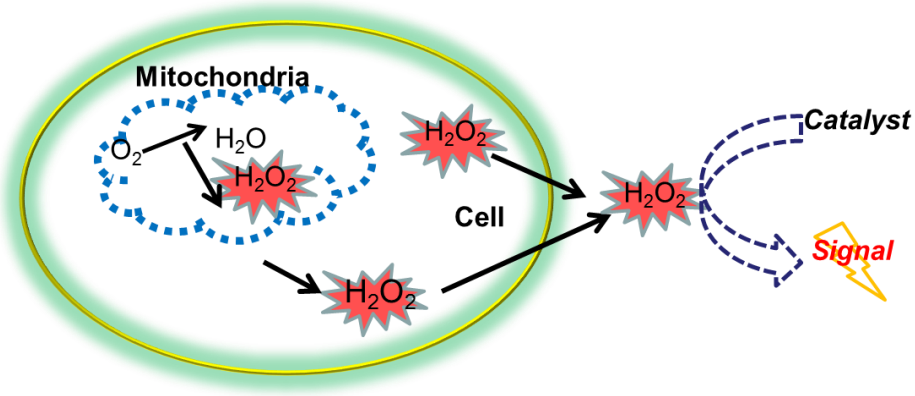

Figure 8.1.1 Schematic illustration of electrochemical detection of H_2O_2 releasing from cells.

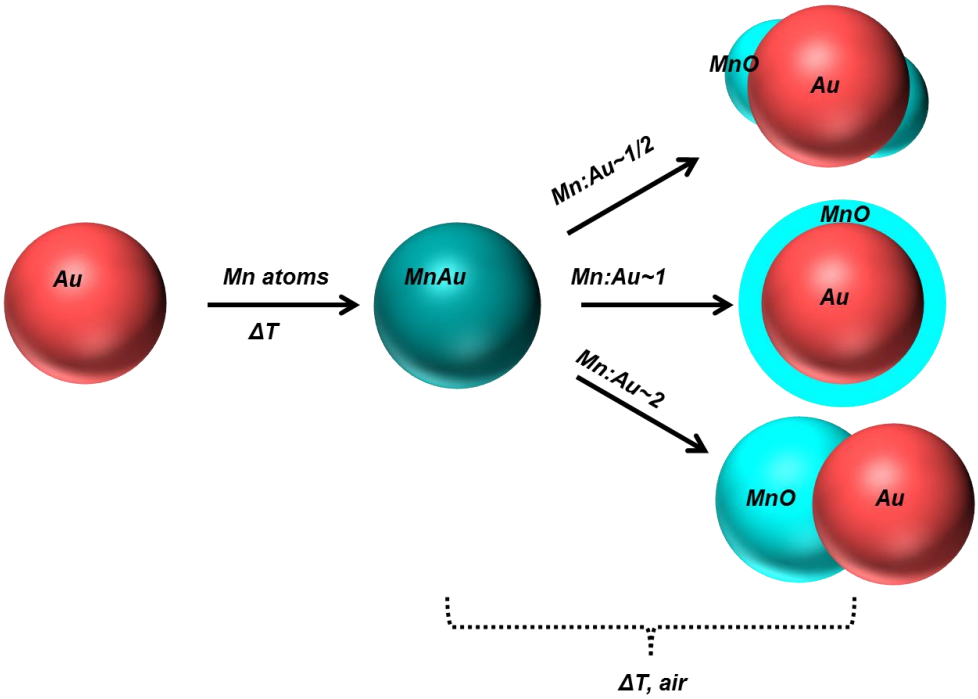

Figure 8.1.2 Schematic illustration of the controlled synthesis of Au-MnO composite NPs.

8.2 Experimental

Chemicals and Materials

Potassium triethylborohydride solution ($KBEt_3H$, 1.0 M in THF), oleylamine (OAm, >70%), oleic acid (OA), 1-octadecene (ODE), Mn(acac)2 (acac = aceylacetonate), choloroauric acid, tetralin, borane tert-butylamine (BBA), N-formylmethionyl-leucyl-phenylalanine, hexane, acetone, isopropanol, ethanol and Nafion (5%) were all purchased from Sigma Aldrich. Phosphate buffered saline (0.1

M, 10X, PH=7.4) was from Gibco by Life Technologies. Hydrogen peroxide was purchased from Fisher Scientific. All cells, MDA-MB-435S, HCT 116 and M4A4 were bought from ATCC .

Characterization

TEM images were obtained from a Philips CM 20 operating at 200 kV. The inductively coupled plasma-atomic emission spectroscopy (ICP-AES) measurements were carried on a JY2000 Ultrace ICP atomic emission spectrometer equipped with a JY AS 421 autosampler and 2400g/mm holographic grating. X-ray diffraction (XRD) characterization was carried out on a Bruker AXS D8-Advanced diffractometer with Cu Kα radiation (λ =1.5418 Å). HRTEM was performed on JEOL 2100 (200kV) TEM with an field-emission electron source and STEM analyses were obtained on a Hitachi HD2700C (200 kV) with a probe aberration-correction in the Center for Functional Nanomaterial at Brookhaven National Laboratory. STEM-EELS mapping using simutaniously recorded Mn L edges and Au M edges were acquired using Gatan-Enfina spectrometer at high dispersion. XPS was carried out by using a Physical Electronics Quantum2000 Microprobe with monochromotic Al X-rays at 500 W and a 200 μM spot area in University of Massachusettes, Amherst. Electrochemical measurements were performed on a Autolab potentiostat from Metrohm Instrument Company (Autolab 302). A three-electrode system consisting of a glassy carbon (GC) working electrode (5-mm in diameter), an Ag/AgCl reference electrode (in 4 M KCl) and a platinum wire counter electrode.

Synthesis of $Au_{67}Mn_{33}$ NPs

100 mg $Mn(acac)_2$ was mixed (by a magnetic stirring) with 2.5 mL oleylamine (OAm) and 12 mL 1-octadecene (ODE) and heated up to 110 oC for 30 min under a gentle flow of N_2 to remove the dissolved oxygen and moisture. Then 60 mg OAm-coated Au NPs in hexane dispersion were added into the reaction system. After 5 min, 2 mL KBEt3H was added and the reaction mixture was heated to 240 ^oC at a rate of 4-5 ^oC/min. After 1 h, the reaction solution was air-cooled to room temperature. The solution was transferred into a 50 mL centrifuge tube and 3 mL OAm and 3 mL oleic acid (OA) were added into the solution to further stabilize the as-synthesized NPs and stand there for 12 h. The AuMn NPs were precipitated out by adding 35 mL isopropanol and centrifugation at 10000 rpm for 8 min, followed by ethanol wash and centrifugation (10000 rpm, 8 min). The AuMn NPs were further purified by dispersion in 20 mL hexane and centrifugation at 5000 rpm for 7 min to remove any un-dispersed impurities. The AuMn NPs were dispersed in hexane for further use.

Under the same reaction condition, 150 mg $Mn(acac)_2$, 60 mg Au seeds and 2.5 mL $KBEt_3H$ yielded $Au_{44}Mn_{56}$ NPs while 200 mg $Mn(acac)_2$, 60 mg Au seeds and 3 mL $KBEt_3H$ gave $Au_{35}Mn_{65}$ NPs.

From AuMn to Au-MnO

The as-synthesized NPs including both Au and AuMn NPs were loaded on Ketjen-300 J carbon (C) with the ratio of 4:6 (by weight) in 20 mL hexane by

sonication for 1 h till the hexane solution turns clear. After wash with ethanol, the product was annealed in air at 170 oC overnight to remove the surfactant. The Au and Au-MnO deposited on C was suspended in a mixture of deionized water, isopropanol and Nafion (V/V/V=4/1/0.05) to form an ink. 20 µl ink was deposited on the GC working electrode that had been polished by 0.1 µm and 0.05 µm alumina powder, rinsed with deionized water, and sonicated in ethanol and then in deionized water). The deposit was dried at ambient condition.

Cell Culture

All the cells were incubated at 37 oC with 5% CO2 in Dulbecco's Modified Eagle Medium (DMEM) with 10% fetal bovin serum (FBS) and 1% Penicillin-Streptomycin. Cells were grown up to 80% confluency. After wash with PBS twice, the cells were trypsinized and collected by centrifugation and re-dispersed in 2 ml 1X PBS for further use.

Electrochemical Measurements

The Au or Au-MnO NP coated electrode was first cleaned by scanning CV between 0.6 V to -0.4 V vs. Ag/AgCl for 60 times. Then CVs were obtained by scanning between 0.6 V to -0.4 V vs Ag/AgCl at a scan rate of 50 mv/s in N_2-saturated 0.1 M PBS without and with 4 mM H_2O_2 to evaluate the catalyst activity of the Au-MnO NPs. Choronamperometric test was applied at -0.28 V vs. Ag/AgCl. After the background current reached a steady-state, a successive addition of H_2O_2 starting from 20 nM was applied in the system to study the detection limit of the

Au-MnO NPs.

Detection of H_2O_2 releasing from cells

After growing to 80% confluency, the cells were washed by PBS and counted using hemocytometer. $0.7x10^6$, $2.4x10^6$, $2.5x10^6$ of MDA-MB-435S, M4A4 and HCT116 cells were used respectively and added into the 0.1 M PBS. The electrochemical system was deoxygenated under N2. Current-time curve was recorded at -0.28 V vs. Ag/AgCl and after a background steady state current was obtained, 8 μM fMLP was added into the system and a corresponding current change was recorded.

8.3 Results and Discussion

8.3.1 Synthesis of Au-MnO Nanocomposites

To synthesize composite Au-MnO NPs, especially core/shell Au/MnO NPs, we tested the direct coating of MnO over Au NPs by decomposition of $Mn(acac)_2$ (acac = acetylacetonate) in the presence of Au NPs, but it failed. We also attempted to prepare Au/MnO by oxidation of core/shell Au/Mn NPs. However, Mn prepared from the reduction of $Mn(acac)_2$ could not form a stable shell around the existing Au NPs. Rather, it diffused easily into Au matrix, resulting in the AuMn solid solution (Figure 8.1.2). As a result, AuMn alloy NPs were readily synthesized. In a typical synthesis, 5 nm Au NPs were prepared as reported.[11] Then in the presence of the Au NPs, $Mn(acac)_2$ was reduced by potassium triethylborohydride ($KBEt_3H$) to Mn that diffused quickly (we could not separate any product showing core/shell structure)

into the Au seeds to form a bimetallic alloy AuMn at 240 ^{o}C. The as-synthesized AuMn NPs were stabilized by oleylamine (OAm) and could be dispersed in a non-polar solvent such as hexane or toluene. The alloy NP compositions were controlled by the mass ratios of Au/Mn(acac)$_2$ and were measured by inductively coupled plasma atomic emission spectroscopy (ICP-AES). Figure 8.2.1 and 8.2.2 show the typical transmission electron microscopy (TEM) images of the as-synthesized Au, $Au_{67}Mn_{33}$, $Au_{44}Mn_{56}$ and $Au_{35}Mn_{65}$ NPs. These NPs have an average diameter of 5 ± 0.2 nm for Au, 5 ± 0.3 nm for $Au_{67}Mn_{33}$, 5.5 ± 0.2 nm for $Au_{44}Mn_{56}$ and 5.7 ± 0.3 nm for $Au_{35}Mn_{65}$.

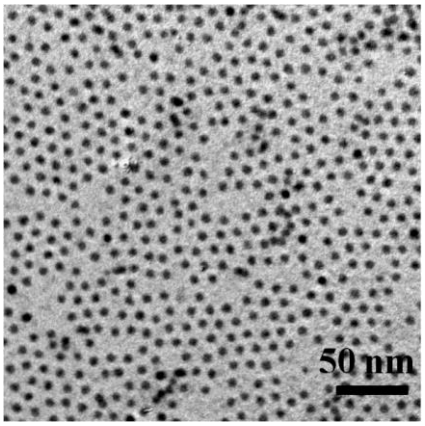

Figure 8.2.1 TEM image of the as-synthesized $Au_{67}Mn_{33}$ NPs.

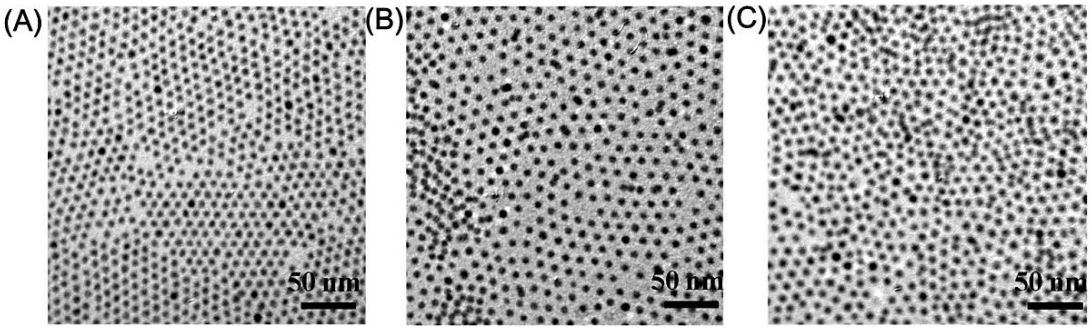

Figure 8.2.2 TEM images of the as-synthesized Au (**A**), $Au_{44}Mn_{56}$ (**B**) and $Au_{35}Mn_{65}$ (**C**) NPs.

The formation of the uniform alloy structure in the AuMn NPs was characterized by high-resolution TEM (HRTEM), high-angle annular dark field (HAADF)-scanning transmission electron microscopy (STEM) and STEM-electron energy-loss spectroscopy (STEM-EELS). As seen from the HRTEM image (Figure 8.2.3), the as-synthesized NPs display a pseudo-icosahedral shape with multi-twinned lattice fringes, which is similar to the pre-made polycrystalline Au NPs,[12] suggesting that the reaction condition used in the current synthesis does not change the crystalline nature of the NPs. The HAADF-STEM image of the $Au_{67}Mn_{33}$ NPs (Figure 8.2.4) shows that all NPs have similar imaging intensity, indicating the uniform mix of Au and Mn within each NP. This is further confirmed by the EELS line scan analysis of a typical $Au_{67}Mn_{33}$ NP (Figure 8.2.5), which shows the uniform Au/Mn distribution across the NP.

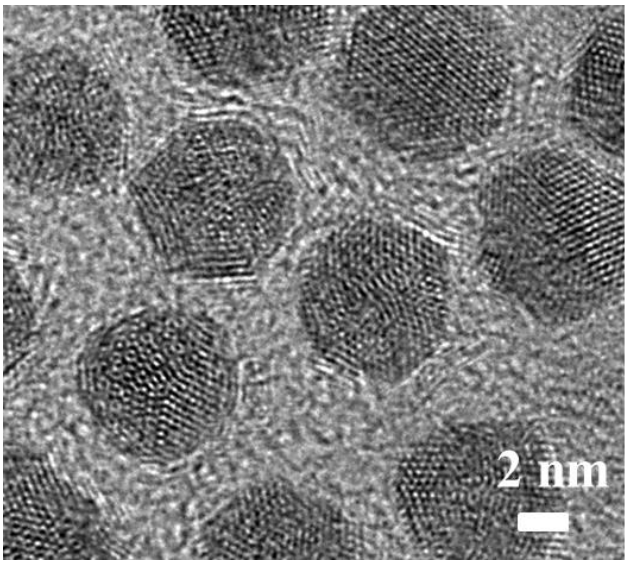

Figure 8.2.3 HRTEM image of the as-synthesized $Au_{67}Mn_{33}$ NPs.

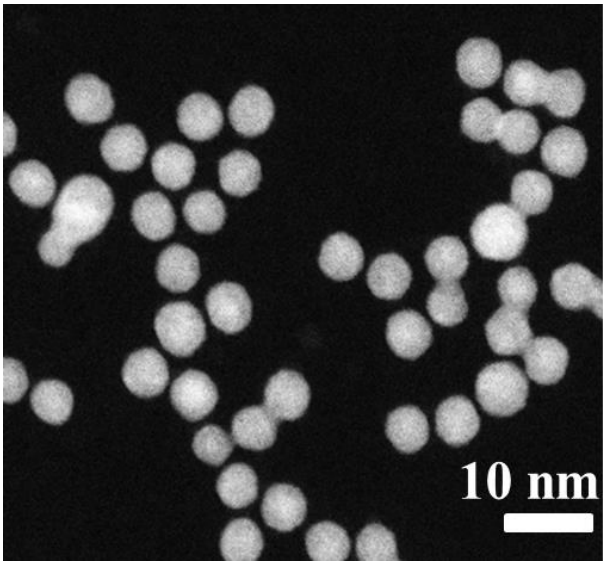

Figure 8.2.4. HAADF-STEM image of the as-synthesized $Au_{67}Mn_{33}$ NPs.

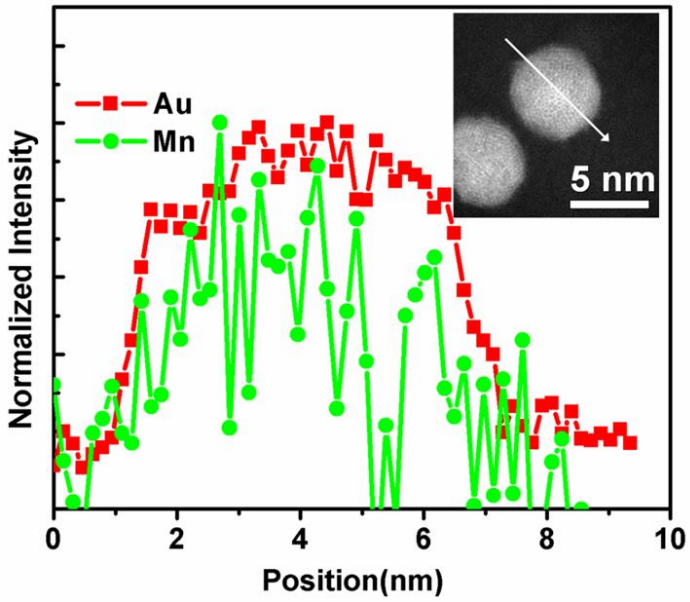

Figure 8.2.5 STEM-EELS line scan of the as-synthesized $Au_{67}Mn_{33}$ NPs.

The solid solution structure of the AuMn NPs was further characterized by X-ray diffraction (XRD) and UV-Vis spectroscopy (Figure 8.2.6A-B). From the XRD, we can see that upon alloying Mn with the face-centered cubic (fcc) Au, the (111) peak shifts slightly to a higher angle but does not change the peak width, indicating the formation of the AuMn alloy reduces the structural lattice parameter but does not lead to any obvious crystal structure change within the NPs. Furthermore, Au NPs dispersed in hexane show a plasmonic absorption at 522 nm. When Mn diffuses into the Au structure, the plasmonic absorption peak of the AuMn alloy NPs is broad and the absorption intensity drops dramatically. We can only observe the absorption at 535 nm from the Au-rich Au67Mn33 NPs. This plasmonic “quenching” in alloy NPs

has been observed previously in other Au-based alloys, such as AuNi and AuPd,[13a-b] confirming that the AuMn NPs have a fcc-type solid solution structure.

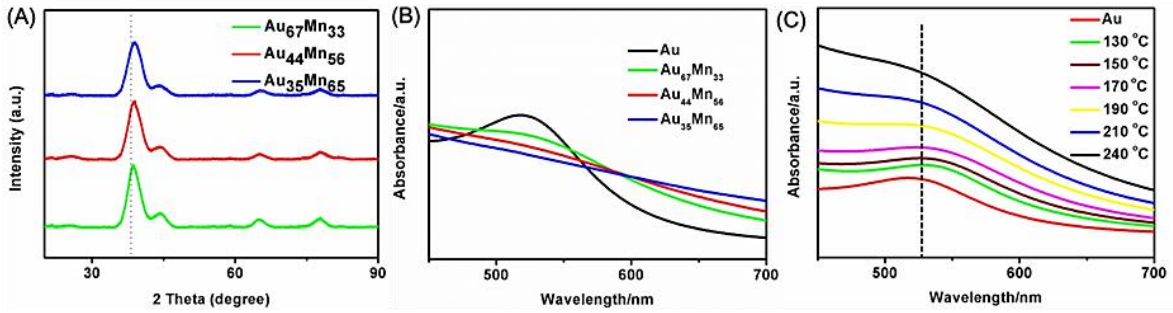

Figure 8.2.6 (A) XRD patterns of the as-synthesized AuMn NPs with different compositions (dashed line denotes standard (111) peak of the bulk Au), (B) UV-vis of Au and AuMn NPs with different compositons, (C) UV-vis of aliquots taken out at different reaction temperatures (the dashed line denotes the SPR position of Au NPs).

To track Mn diffusion into Au, we took aliquots at different reaction stages from the reaction system for characterizations. As shown in Figure 8.2.6C and Table 8.1, from 130 ^{o}C to 240 ^{o}C, Mn is gradually alloyed with Au, and along with the increase of Mn composition in the alloy structure, the plasmonic absorption peak red-shifts with much reduced intensity. The results from this controlled experiment indicate that once Mn is deposited on the Au surface, it immediately diffuses into Au lattice at the reaction temperatures, leaving no evidence of Mn-coating over the Au NPs. Therefore, using the synthetic condition described, core/shell Au/Mn or Au/MnO could not be formed.

Temperatures	Mn:Au Compositions from ICP-AES
130 ^{o}C	12:88
150 ^{o}C	18:82
170 ^{o}C	22:78
190 ^{o}C	25:75
210 ^{o}C	32:68
240 ^{o}C	33:67

Table 8.1 Composition of aliquots taken out at different reaction temperature.

To prepare Au-MnO composites, we first loaded the AuMn NPs on Ketjen carbon (denoted as C-AuMn) and annealed them in air at 170ºC to oxidize Mn. This process also helped to remove the surfactant, similar to what has been reported in activating Au NPs for electrochemical reduction reaction.[11] TEM images of the C-$Au_{67}Mn_{33}$ and C-$Au_{44}Mn_{56}$ show no obvious NP morphology changes (Figure 8.2.7, 8.2.8A), but the C-$Au_{35}Mn_{65}$ NPs look different (Figure 8.2.8B). HRTEM image of a single annealed $Au_{35}Mn_{65}$ NP (Figure 8.2.9) indicates a dumbbell-like structure as illustrated in Figure 8.1.2. HAADF-STEM 2D-mapping and line scan allow us to further characterize the structure changes during this annealing. Figure 8.2.10 and 8.2.11A-B show the elemental mapping of the annealed AuMn NPs. In all these three cases, the Mn phase segregates out onto the Au surface. Mn with stronger bonding with O_2 tends to diffuse out during the annealing process, forming Mn-oxide, similar to what have been observed in AuNi and AuCu systems.[13a, 13c] Depending on the Au/Mn composition in the alloy structure, the air annealing produced different Au-MnO composites. The $Au_{67}Mn_{33}$ is converted to Au-MnO with MnO forming the isolated

islands on Au. If more Mn is present, as in the $Au_{35}Mn_{65}$, the new MnO phase self-aggregate on the Au surface, forming a dumbbell-like structure. When the $Au_{44}Mn_{56}$ NPs are air-annealed, a quasi-core/shell structure Au/MnO is developed. The core/shell structure is further confirmed by the EELS line scan analysis (Figure 8.2.12). This MnO outer shell is uniform as confirmed by the identical EELS (Figure 8.2.13) recorded from the center and edge in the Mn L edges indicated in Figure 8.2.10.

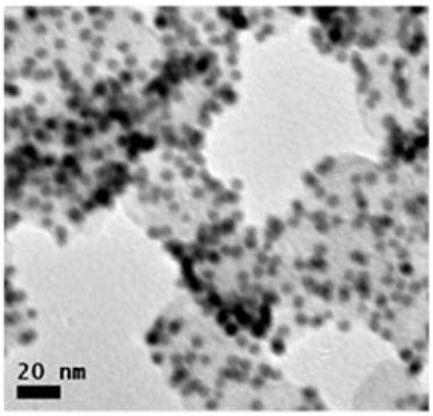

Figure 8.2.7 TEM image of C-$Au_{44}Mn_{56}$ after annealing.

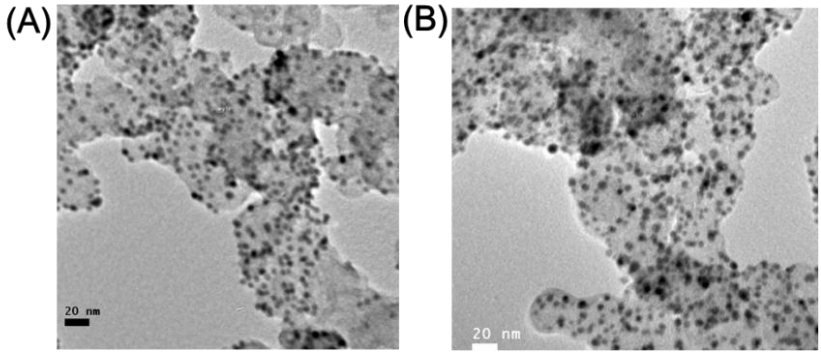

Figure 8.2.8 TEM images of $Au_{67}Mn_{33}$ (A), $Au_{35}Mn_{65}$ (B) NPs deposited on C after air annealing.

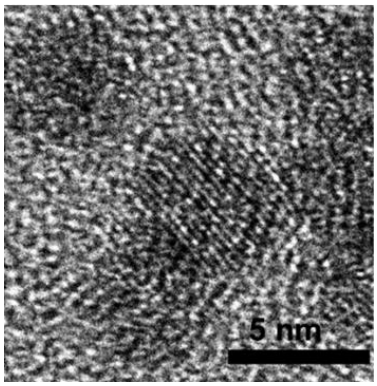

Figure 8.2.9 HRTEM image of a single $Au_{35}Mn_{65}$ NP deposited on C after air annealing.

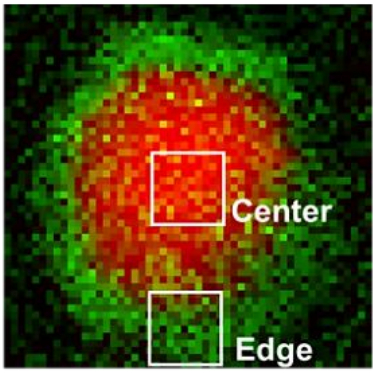

Figure 8.2.10 STEM-EELS 2D mapping of C-$Au_{44}Mn_{56}$ after annealing.

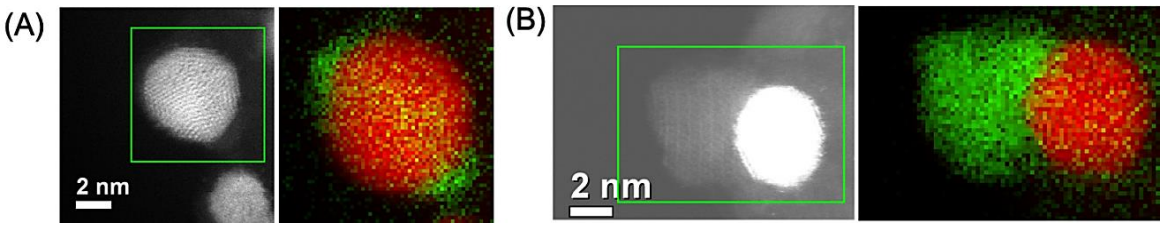

Figure 8.2.11 STEM-EELS 2D mapping of the $Au_{67}Mn_{33}$ (A) and $Au_{35}Mn_{65}$ (B) NPs after air annealing.

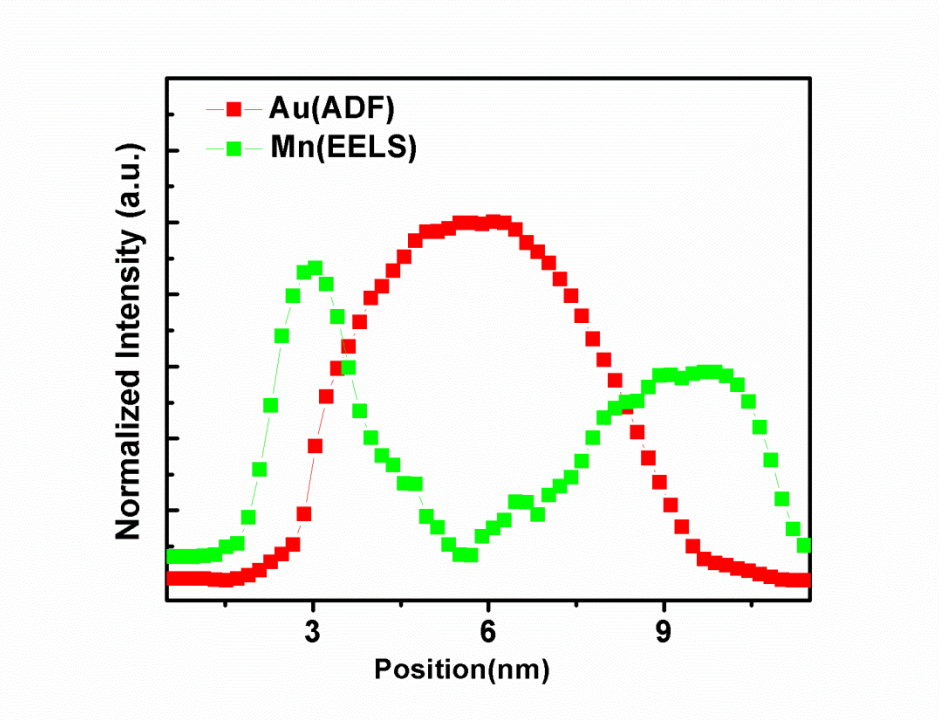

Figure 8.2.12 STEM-EELS line scan of C-$Au_{44}Mn_{56}$ after annealing.

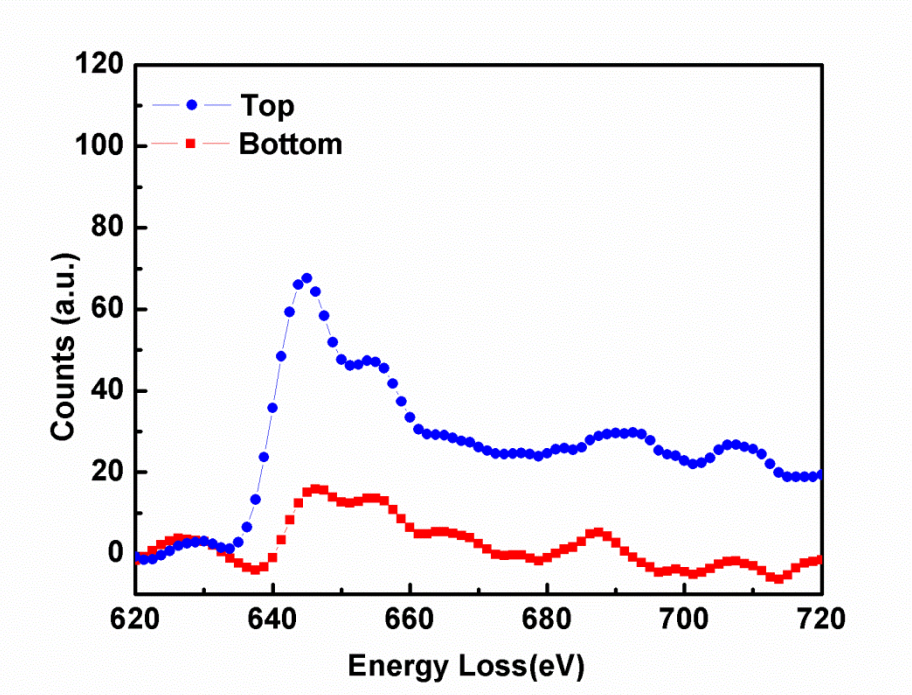

Figure 8.2.13 Mn L edges EELS spectra from the selected areas shown in Figure

8.2.10 of C-Au44Mn56 after annealing.

XRD pattern of the $Au_{44}Mn_{56}$ and Au/MnO NPs (obtained after air annealing of the $Au_{44}Mn_{56}$ NPs) show no obvious peak change, suggesting that MnO in the Au/MnO has an amorphous structure (Figure 8.2.14). X-ray photoelectron spectroscopy (XPS) (Figure 8.2.15A-B) of the Au/MnO NPs show a binding energy of 641.2 eV for Mn 2p3/2 in all the annealed NPs which can be indexed to either Mn^{2+} (640.9 eV) or Mn^{3+} (641.9 eV).[14] Additionally, the binding energy difference between Mn 2p1/2 and 2p3/2 was found to be 11.4 eV close to the reported 11.6 eV in MnO (Figure 8.2.15B).[14a] This, plus the well-known stability of MnO in Mn-oxide chemistry and the air-annealing condition we applied at 170ºC, makes us believe that MnO is the oxide form present around the Au NPs in the core/shell structure.

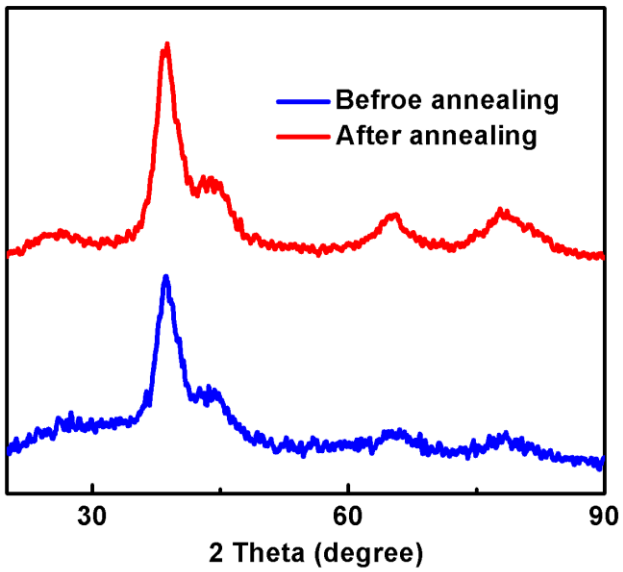

Figure 8.2.14 XRD patterns of the $Au_{44}Mn_{56}$ and Au/MnO (obtained from the annealing of the $Au_{44}Mn_{56}$ NPs).

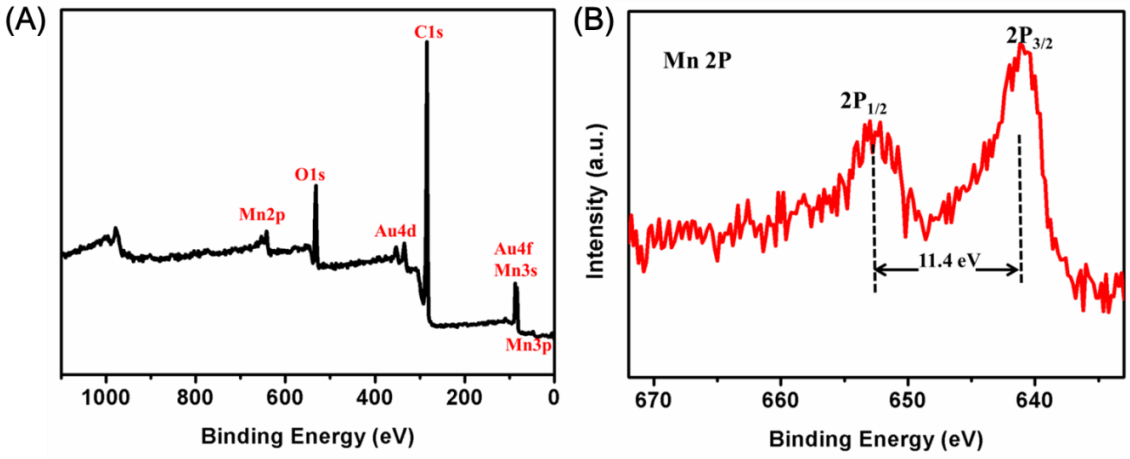

Figure 8.2.15 XPS of a wide-scan (A) and Mn 2p sepectrum (B) of the Au/MnO NPs (obtained from the annealing of the $Au_{44}Mn_{56}$ NPs).

8.3.2 Au-MnO Nanocomposites for H_2O_2 Detection

To perform the electrochemical study of H_2O_2 reduction, a catalyst ink was prepared following the reported procedure.[15] 20 µl of the catalyst ink was drop-cast on the glassy carbon electrode and dried at ambient condition. Figure 8.2.16 shows the CVs of the Au and Au/MnO NPs in N2-saturated 0.1 M phosphate buffered saline (PBS) with and without 4 mM H_2O_2. The CVs of other Au-MnO NPs are given in Figure 8.2.17 All Au-MnO NPs exhibit higher reduction peak currents compared to the pure Au NPs with the core/shell Au/MnO NPs being the most active catalyst. The

highest activity of the Au/MnO may be caused by its unique core/shell structure, where the interfacial effect of MnO and Au favors electrochemical reduction of H_2O_2 on MnO surface.

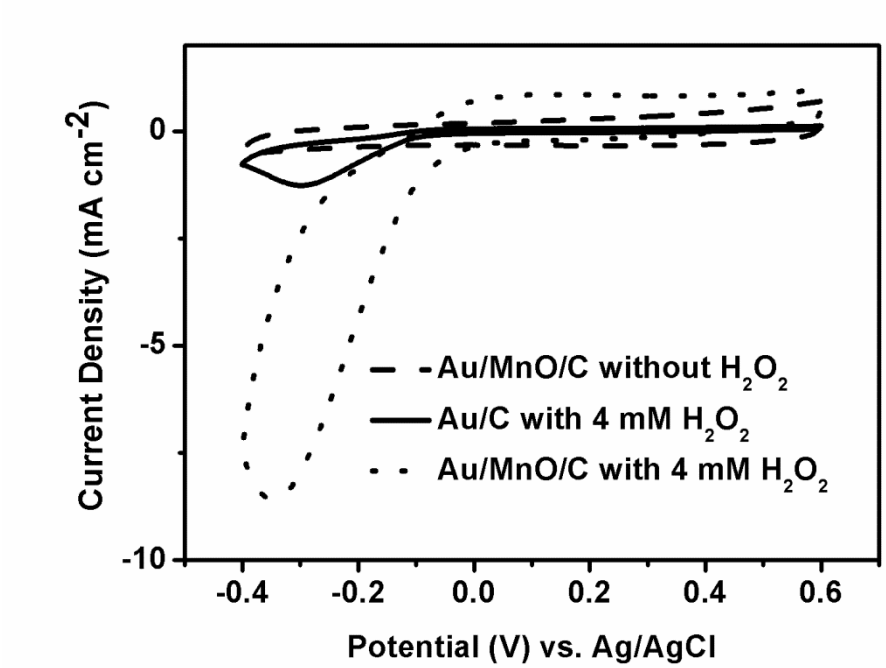

Figure 8.2.16 CVs of Au and Au/MnO NPs with or without the presence of 4 mM H_2O_2 in 0.1 M PBS.

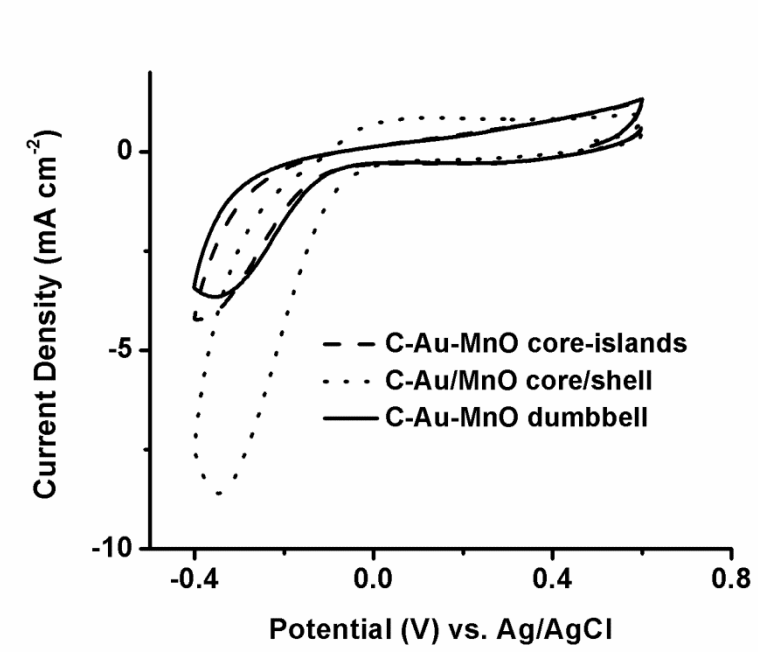

Figure 8.2.17 CVs of the C-Au-MnO NPs with different morphologies in the presence of 4 mM H_2O_2.

Chronoamperometry was applied to evaluate the sensitivity of the Au/MnO NPs for H_2O_2 detection. Figure 8.2.18 and Figure 8.2.19 present the current response of Au/MnO NP modified glassy carbon (GC) electrode upon addition of H_2O_2 at -0.28 V vs. Ag/AgCl. With the addition of 20 nM up to 15.11 mM H_2O_2, reduction current rapidly increases and reaches a steady state. Based on a signal to noise factor of 3 (S/N = 3), a detection limit can be calculated to be 8 nM for the Au/MnO NPs. The calibration curve of current vs. H_2O_2 concentration is shown in Figure 8.2.19. It exhibits three different linear relationships in the range of 20 - 100 nM (R^2 = 0.9961, sensitivity = 17850 μA/mM cm^{-2}), 100 nM – 1111.1 μM (R^2 = 0.9989, sensitivity = 208 μA/mM cm^{-2}) and 1111.1 μM - 15.11 mM (R^2 = 0.9973, sensitivity = 530

μA/mM cm^{-2}) respectively. This may be caused by different reduction kinetics at different H_2O_2 concentration ranges. H_2O_2 reduction is dominated by H_2O_2 adsorption at extremely low H_2O_2 concentration, while H_2O_2 activation becomes the rate-determining step when H_2O_2 concentration is very high. In the middle region, H_2O_2 reduction is controlled by a combat between H_2O_2 adsorption and activation.

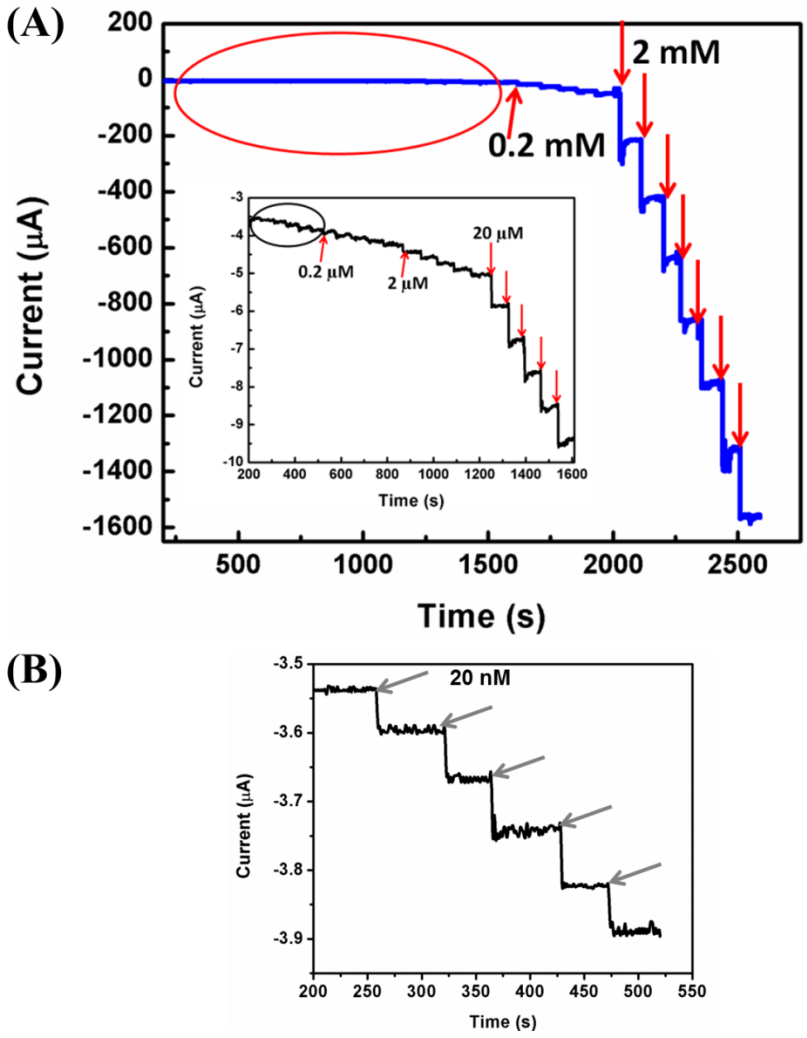

Figure 8.2.18 (A) Current-time plot of the Au/MnO NPs to the successive addition of H_2O_2 in 0.1 M PBS at -0.28V vs. Ag/AgCl. Inset is the close look of the red oval

region (20 nM to 111.1 μM). (B) Current-time plot of the Au/MnO to the successive addition of H_2O_2 from 20 nM to 100 nM in 0.1 M PBS at -0.28 V.

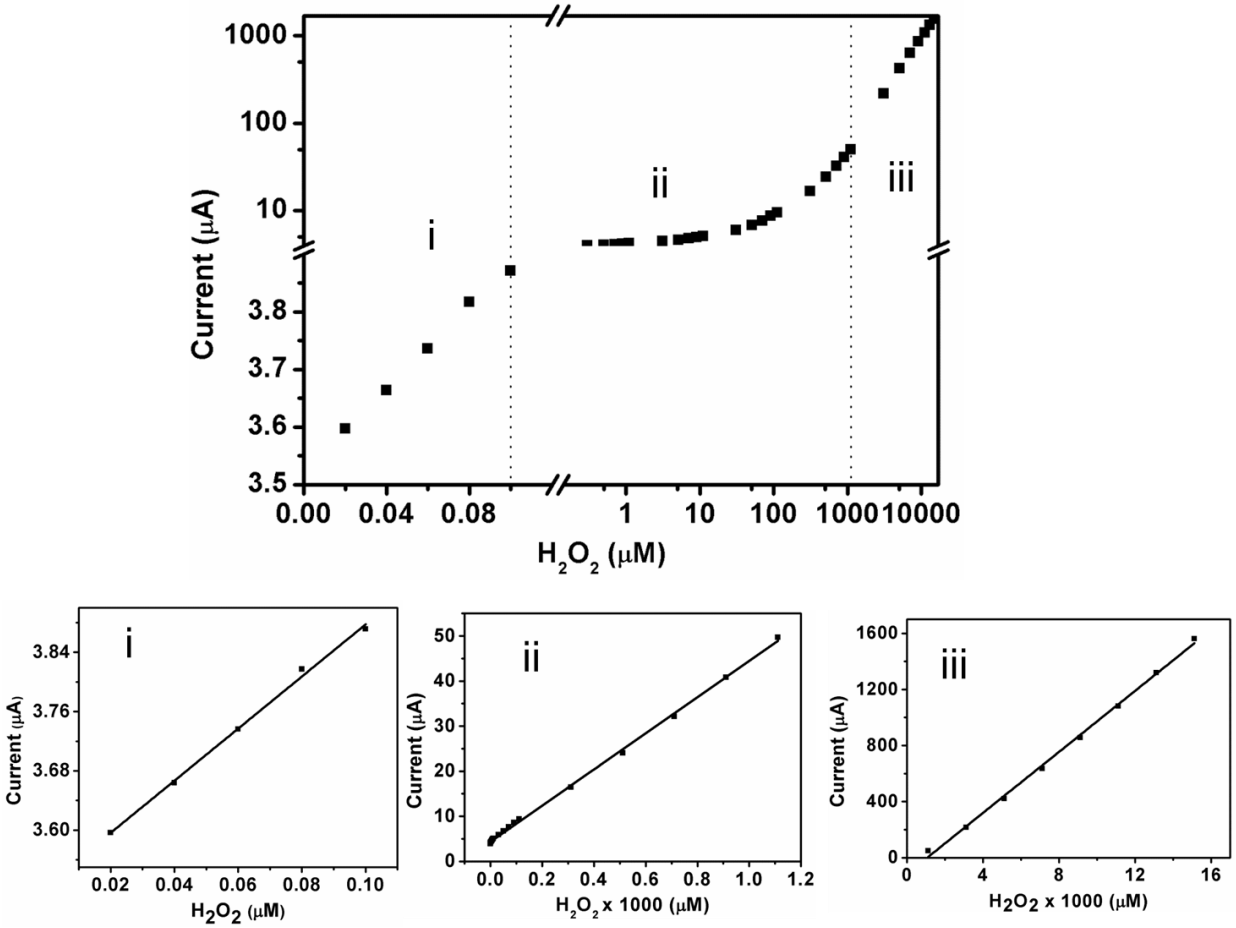

Figure 8.2.19 Calibration curve of current vs. H_2O_2 concentration. The curve is splitted into three regions, i, ii, and iii, which are plotted separately to see clearly the linear relationship between current and H_2O_2 concentration.

With high sensitivity achieved, the Au/MnO NPs can be used to detect H_2O_2 released from living cells. The H_2O_2 release was triggered by adding

N-formylmethionyl-leucyl-phenylalanine (fMLP), which can resemble the oxidative metabolism most likely to be encountered in vivo.[7b, 9] In the presence of each of the MDA-MB-435S (human breast melanoma cells), HCT116 (human colorectal carcinoma cells) or M4A4 cells (human epithelial cells), the addition of 8 µM fMLP led to an immediate current response (Figure 8.2.20). Without cells, no current response was recorded, suggesting the current change is due to H_2O_2 releasing from the living cells. We can further distinguish these cells by the current response. The current change for non-tumorigenic MDA-MB-435S cells (count: 0.7x106) is 0.3 µA that corresponds to 12 pM H_2O_2 released per cell; however, the tumorigenic HCT116 (count: 2.5x106) and M4A4 (count: 2.4x106) cells are 2.5 µA and 3.3 µA, equal to 25 pM and 33 pM H_2O_2, respectively, released per cell. This is consistent to the fact that tumorigenic cells tend to generate more H_2O_2 due to the fast oxygen metabolism. This study proves that our Au/MnO NP electrode presents a sensitive probe for extracellular H_2O_2 detection and quantification.

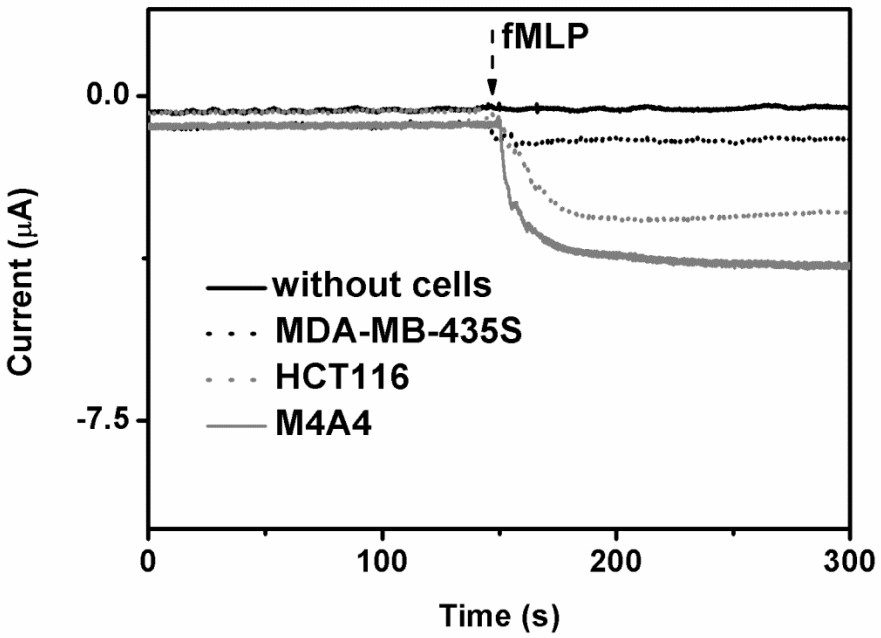

Figure 8.2.20 Amperometric response of Au/MnO modified electrode in the presence of no cells, MDA-MB-435S, HCT116, M4A4 cells for the detection of H_2O_2 releasing.

8.4 Conclusion

In summary, we have developed a new methodology to synthesize AuMn alloy NPs by a seed-mediated atomic diffusion process. The morphology and composition of the as-synthesized AuMn NPs are well controlled. When annealed in air, these AuMn NPs are converted into composite Au-MnO or core/shell Au/MnO depending on the Au/Mn composition ratios. These composite NPs, especially core/shell Au/MnO NPs, are active for electrochemical reduction of H_2O_2 with the detection limit reaching 8 nM at -0.28 V vs. Ag/AgCl. They are highly efficient in

distinguishing non-tumorigenic and tumorigenic cells by monitoring H_2O_2 levels released from these cells as illustrated in Figure 8.3.1. They may be used as a sensitive probe for cancer detection.

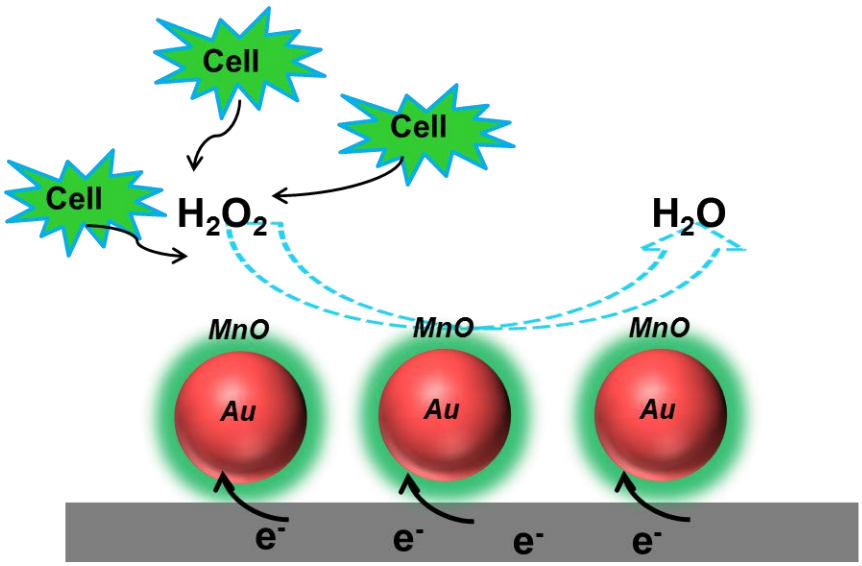

Figure 8.3.1 Schematic illustration of Au/MnO as sensitive bioprobe for detection of H_2O_2 releasing from living cells.

References

1. a) B. Halliwell, *J. Neurochem.* **1992**, *59*, 1609-1623;

b) W. Dorge, H. M. Schipper, *Aging Cell* **2007**, *6*, 361-370;

c) D. J. Rossi, C. H. M. Jamieson, I. L. Weissman, *Cell* **2008**, *132*, 681-696;

d) E. A. L. Martins, R. Meneghini, *Biochem. J.* **1994**, *299*, 137-140.

2. a) M. N. Tahir, R. Andre, J. K. Sahoo, F. D. Jochum, P. Theato, F. Natalio, R. Berger, R. Branscheid, U. Kolb, W. Tremel, *Nanoscale* **2011**, *3*, 3907-3914;

b) Y. Guo, L. Deng, J. Li, S. Guo, E. Wang, S. Dong, *ACS Nano* **2011**, *5*, 1282-1290.

3. a) P. Wu, Z. Cai, J. Chen, H. Zhang, C. Cai, *Biosens. Bioelectron*. **2011**, *26*, 4012-4017;

b) M. Ali, M. N. Tahir, Z. Siwy, R. Neumann, W. Tremel, W. Ensinger, *Anal. Chem.* **2011**, *83*, 1673-1680.

4. W. Chen, S. Cai, Q. Ren, W. Wen, Y. Zhao, *Analyst* **2012**, *137*, 49-58.

5. a) L. Wang, E. Wang, *Electrochem. Commun.* **2004**, *6*, 225-229;

b) F. Li, Y. Feng, Z. Wang, L. Yang, L. Zhou, B. Tang, *Biosens. Bioelectron*. **2010**, *25*, 2244-2248;

c) J. Zhang, M. Oyama, *Electrochimica Acta* **2004**, *50*, 85-90.

6. a) F. Meng, X. Yan, L. Liu, J. Gu, Z. Zou, *Electrochimica Acta* **2011**, *56*, 4657-4662;

b) J. Yin, X. Qi, L. Yang, G. Hao, J. Li, J. Zhong, *Electrochimica Acta* **2011**, *56*,

3884-3889.

7. a) H. Wang, X. Bo, J. Bai, L. Wang, L. Guo, *J. Electroanal. Chem.* **2011**, *662*, 281-287;

b) F. Xiao, Y. Li, X. Zan, K. Liao, R. Xu, H. Duan, *Adv. Funct. Mater*. **2012**, *22*, 2487-2494;

c) Y. Lin, X. Cui, L. Li, *Electrochem. Commun*. **2005**, *7*, 166-172;

d) Y. Bai, H. Zhang, J. Xu, H. Chen, *J. Phys. Chem. C*. **2008**, *112*, 18984-18990;

e) C. E. Langley, B. Sljukic, C. E. Banks, R. G. Compton, *Anal. Sci.* **2007**, *23*, 165-170;

f) Y. Bai, Y. Du, J. Xu, H. Chen, *Electrochem. Commun*. **2007**, *9*, 2611-2616.

8. Y. Lee, M. Garcia, N. Huls, S. Sun, *Angew. Chem. Int. Ed*. **2010**, *49*, 1271-1274.

9. X. Sun, S. Guo, Y. Liu, S. Sun, *Nano Lett.* **2012**, *12*, 4859-4863.

10. C. Xu, J. Xie, D. Ho, C. Wang, N. Kohler, E. G. Walsh, J. R. Morgan, Y. E. Chin, S. Sun, *Angew. Chem. Int. Ed.* **2008**, *47*, 173-176.

11. W. Zhu, R. Michalsky, O. Metin, H. Lv, S. Guo, C. J. Wright, X. Sun, A. A. Peterson, S. Sun, *J. Am. Chem. Soc.* **2013**, *135*, 16833-16836.

12. a) W. Chen, R. Yu, L. Li, A. Wang, Q. Peng, Y. Li, *Angew. Chem. Int. Ed.* **2010**, *49*, 2917-2921;

b) S. Peng, Y. Lee, C. Wang, H. Yin, S. Dai, S. Sun, *Nano Res.* **2008**, *1*, 229-234.

13. a) S. Zhou, H. Yin, V. Schwartz, Z. Wu, D. Mullins, B. Eichhorn, S. H. Overbury, S. Dai, *ChemPhysChem* **2008**, *9*, 2475-2479;

b) O. Metin, X. Sun, S. Sun. *Nanoscale* **2013**, *5*, 910-912;

c) N. E. Motl, J. F. Bondi, R. E. Schaak, *Chem Mater*. **2012**, *24*, 1552-1554.

14. a) G. Xu, L. Zhang, C. Guo, L. Gu, X. Wang, P. Han, K. Zhang, C. Zhang, G. Cui, *Electrochimica Acta* **2012**, *85*, 345-351;

b) H. W. Nesbitt, D. Banerjee, *American Mineralogist* **1998**, *83*, 305-315.

15. a) H. Zhu, S. Zhang, S. Guo, D. Su, S. Sun, *J. Am. Chem. Soc*. **2013**, *135*, 7130-7133;

b) H. Zhu, S. Zhang, Y. Huang, L. Wu, S. Sun, *Nano Lett*. **2013**, *13*, 2947-2951.

Chapter 9

Structure-Controlled FePtAu Nanoparticles for Formic Acid Oxidation

9.1 Background and Introduction

In the chapter 3-8, I have discussed about the rational synthesis of nnanoparticles (NPs) for oxygen reduction reaction (ORR) which happens at the cathode of the proton exchange membrane fuel cells and H_2O_2 reduction for biodetection purpose. In this chaper, we will discuss our rational synthesis and structure-control strategy to tune and optimize NP catalysis for electrooxidation reactions. Here structure-controlled FePtAu NPs and their catalytic properties for formic acid oxidation (FAOR) will be provied as an example. Considering the slow kinetics and CO-poisoning problems of single component Pt NPs in their catalysis for FAOR as shown in Chapter 1 and Figure 9.1, an ideal catalyst for FAOR should be able to efficiently catalyze the FAOR in dehydrogenation pathway without generating CO. Recent advance in nanoparticle (NP) synthetic methodology has led to the formation of various monodisperse metallic NPs with ever increased activity to catalyze oxidation of fuel (hydrogen, formic acid, or alcohol) and reduction of oxygen in polymer electrolyte membrane fuel cell conditions.[1-3] Among all the NPs studied, Pt and its alloy NPs have constantly been the catalyst choice due to their high activity for fuel oxidation and oxygen reduction reactions.[4-12] However, these Pt-based NPs have shown serious limitations in their fuel cell catalysis: they are unstable in the corrosive electrochemical environment and prone to deactivation by reaction intermediate species such as carbon monoxide (CO).[13] As a result, NP catalysts based on elemental Pt and composition-controlled Pt-alloys are far from optimized for fuel

cell applications. Very recently, core/shell type NPs with a thin (< 2 nm) uniform coating of Pt-shell were prepared and demonstrated to be a robust class of catalyst for oxygen reduction reaction.[14-16] Despite this progress, there is still no reliable approach to NP catalysts with simultaneous enhancement in both activity and durability for practical fuel oxidation reactions.

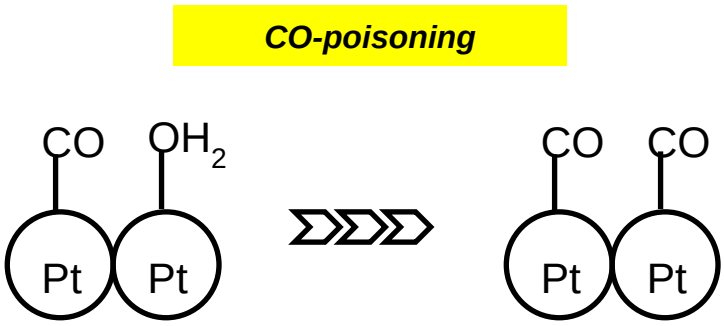

Figure 9.1 Schematic illustration of CO-poisoning on Pt surface.

This chapter will present a new structure-control strategy to tune and optimize NP catalysis for fuel oxidations. NPs, especially multimetallic NPs, can adopt different crystal structures. For example, as synthesized from a high temperature solution-phase reaction, monodisperse binary FePt NPs have the chemically disordered face centered cubic (*fcc*) structure in which Fe and Pt atoms occupy randomly the *fcc* crystal lattice.[17] When further annealed, the *fcc*-structure can be converted into chemically ordered face centered tetragonal (*fct*) structure in which Fe and Pt atoms form alternating atomic layers stacked along one specific direction.[17]

Such a structure conversion in FePt can result in drastic magnetic property change from superparamagnetism to ferromagnetism[18] and in ORR catalytic enhancement in acid solutions as we discussed in Chapter 6.[19] It is this properties in *fct*-FePt that leads to the current work to explore structure-induced NP catalysis for electrooxidation reactions with simultaneous enhancement in both activity and durability.

The catalyst studied here is monodisperse trimetallic FePtAu NPs. Au is chosed because of the presence of Au in FePtAu facilitates FePt structural transformation from *fcc* to *fct* with Au segregating on the *fct*-FePt surface as shown in Figure 9.1.2. This structure change further promotes formic acid oxidation reaction (FAOR) - the anode reaction that is used to power direct formic acid fuel cells.[20]

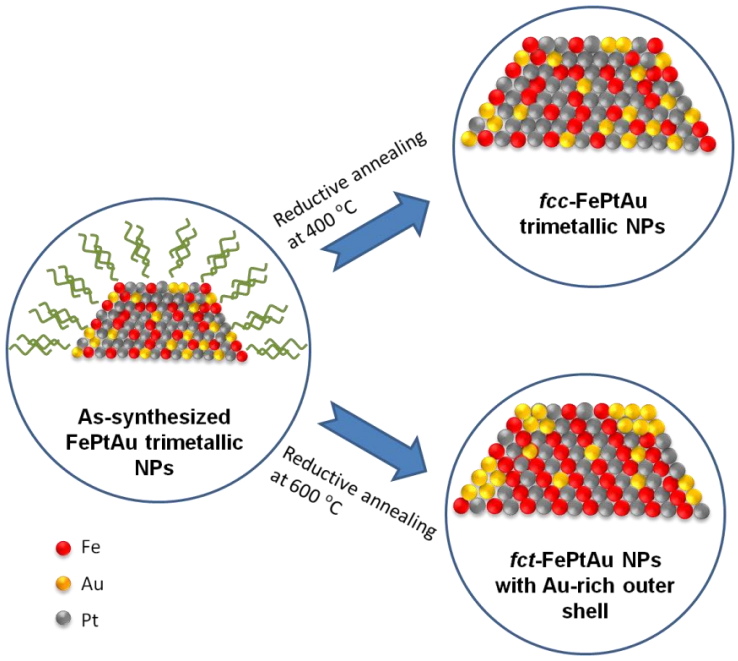

Figure 9.1.2 Schematic illustration of the structural change of the FePtAu NPs upon

annealing. When annealed at 400 ^{o}C, the FePtAu NPs are fcc structured, but at 600 ^{o}C, the fct-FePtAu structure is formed with Au-segregating on the NP surface.

9.2 Experimental

Characterization

The ICP-AES measurements were carried on a JY2000 Ultrace ICP Atomic Emission Spectrometer equipped with a JY AS 421 autosampler and 2400g/mm holographic grating. XRD characterizations were carried out on a Bruker AXS D8-Advanced diffractometer with Cu Kα radiation (λ =1.5418 Å). Samples for TEM analysis were prepared by depositing a single drop of diluted NP dispersion in hexane on amorphous carbon coated copper grids. TEM images were obtained using a Philips CM 20 (200 kV). HRTEM images were obtained using a FEI Titan 80-300 (300 kV) with an aberration (image) corrector and STEM analyses were carried out using a Hitachi HD2700C (200kV) with a probe aberration-corrector, in the Center for Functional Nanomaterials at Brookhaven National Lab. The 2D EELS mapping were collected using a high resolution Gatan-Enfina ER with a probe size of 1.3Å and the EDX line-scan was obtained by a Bruker-AXS X-Flash 5030 silicon drift detector with an electron probe of ~2 Å. A power law function was used for EELS background subtraction.

Synthesis of FePtAu NPs

Under a gentle flow of N_2, 73 mg of platinum acetylacetonate ($Pt(acac)_2$, 0.188

mmol, Aldrich, 98%) and 22 mg of chloroauric acid hydrate ($HAuCl_4.xH_2O$, 0.063 mmol, 99.9%, Strem Chemicals) were mixed in 20 mL of octadecene (ODE, Aldrich, 90%) in the presence of 0.68 mL of oleylamine (OAm, 2 mmol, Aldrich, 70%) and 140 mg of tetradecylphosphonic acid (TDPA, 1 mmol, Alfa Aesar, 98%). The mixture was magnetically stirred and heated to 100 ºC to generate a light yellow transparent solution. Under a N_2 blanket, 0.10 mL of iron pentacarbonyl ($Fe(CO)_5$, 0.75 mmol, Aldrich, 99.9+%) was added into the solution, inducing an immediate color change to black in the solution. The solution was heated to 250 ºC at a rate of about 20 °C /min and kept at this temperature for 10 min before it was cooled to room temperature. The NPs were separated by adding isopropanol (50 mL), followed by centrifugation (8500 rpm, 8 min). The NPs were further purified by dispersing into hexane (20 mL) and centrifugation (5000 rpm, 8 min) to remove any un-dispersed precipitates. The product was precipitated out by adding ethanol (50 mL) and centrifugation (8500 rpm, 8 min) and re-dispersed in hexane. The synthesis yielded $Fe_{42}Pt_{44}Au_{14}$ NPs.

In the same reaction condition, 61 mg of $Pt(acac)_2$ (0.156 mmol) and 32 mg of $HAuCl_4$ (0. 094 mmol) led to the formation of $Fe_{43}Pt_{37}Au_{20}$ NPs. 49 mg of $Pt(acac)_2$ (0.125 mmol) and 43 mg of $HAuCl_4$ (0. 125 mmol) yielded $Fe_{34}Pt_{34}Au_{32}$ NPs and 98 mg of $Pt(acac)_2$ (0.25 mmol), and no addition of $HAuCl_4$ gave $Fe_{55}Pt_{45}$ NPs.

Catalyts Preparation

An equal amount (20 mg each) of NPs and Ketjen carbon support were mixed in 50 mL of hexane/acetone (v/v 1/1) and sonicated with a Fischer Scientific FS 110 for

1 h. The catalyst was separated by centrifugation and washed with hexane twice. The C/NPs were dried under ambient conditions and annealed at different temperatures for 1 h in a gas flow of Ar + 5% H_2. The commercial C/Pt (20% mass loading, 2.5-3.5 nm in diameter) catalysts were obtained from Fuel Cell Store.

Electrochemical measurements

The electrochemical measurements were performed on a Pine Electrochemical Analyzer, Model AFCBP1 with a three-electrode system consisting of a glassy carbon (GC) working electrode (5-mm in diameter), an Ag/AgCl reference electrode (10% KNO_3), and a platinum wire counter electrode. To prepare C/NP-modified GC working electrodes, C/NP NPs were dispersed in a mixture of water/2-propanol/5% Nafion (v/v/v = 1/4/0.025) under sonication to form a 4 mg/mL (for commercial C/Pt or C/Pd catalyst) or 2 mg/mL (for all the other catalysts) catalyst ink[26]. 20 μL of this ink was dropped onto the surface of the GC electrode, and then dried under ambient conditions. The N_2-saturated 0.5 M H_2SO_4 was used as the test solution. In the CV measurements, the electrode potential was scanned in the range from -0.2 to 0.9 V (*vs.* Ag/AgCl). Chronoamperometry was carried out at the constant potential of 0.2 V in an electrolyte solution containing 0.5 M H_2SO_4 and 0.5 M HCOOH. All the catalyst electrodes were cleaned before data collection with a steady-state CV in the range from -0.25 to 1.0 V (*vs* Ag/AgCl) at a scan rate of 50 mV/s.

9.3 Results and Discussion

9.3.1 Synthesis of Structure-Controlled FePtAu NPs

FePtAu NPs were synthesized by co-reduction of platinum acetylacetonate, $Pt(acac)_2$, and chloroauric acid hydrate, $HAuCl_4 \bullet xH_2O$, and thermal decomposition of iron pentacarbonyl, $Fe(CO)_5$ (see **Experimental**). In the synthesis, the excess of $Fe(CO)_5$ was added to function both as a reducing agent and as a Fe precursor for its alloying with Pt and Au. Oleylamine and tetradecylphosphonic acid were used to stabilize the NPs. FePtAu compositions were controlled by varying the molar ratios of $Pt(acac)_2$, $HAuCl_4 \bullet xH_2O$, and $Fe(CO)_5$ and were analyzed by inductively coupled plasma-atomic emission spectroscopy (ICP-AES) (Table 9.1). 4 nm $Fe_{55}Pt_{45}$ NPs were also synthesized similarly without the presence of Au salt. Transmission electron microscopy (TEM) images show that the as-synthesized FePt and FePtAu NPs have an average size of 4 nm ± 0.2 nm for $Fe_{55}Pt_{45}$ (Figure 9.2.1), 4 nm ± 0.2 nm for $Fe_{42}Pt_{44}Au_{14}$ (Figure 9.2.2A), 4 nm ± 0.2 nm for $Fe_{43}Pt_{37}Au_{20}$ (Figure 9.2.3A) and 4 nm ± 0.3 nm for $Fe_{34}Pt_{34}Au_{32}$ NPs (Figure 9.2.2B).

Sample	$Pt(acac)_2/HAuCl_4$ molar ratio	As-synthesized NPs
A	3:1	$Fe_{42}Pt_{44}Au_{14}$
B	3:2	$Fe_{43}Pt_{37}Au_{20}$
C	3:3	$Fe_{34}Pt_{34}Au_{32}$

Table 9.1 The composition control of as-synthesized FePtAu NPs by varying the molar ratios of $Pt(acac)_2/HAuCl_4$.

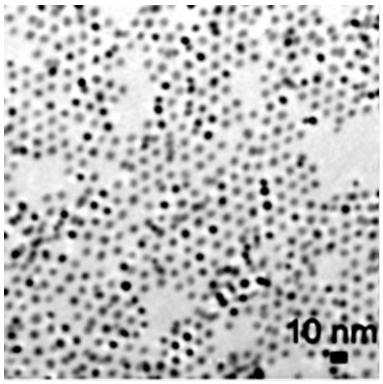

Figure 9.2.1 TEM images of the 4 nm $Fe_{55}Pt_{45}$ NPs.

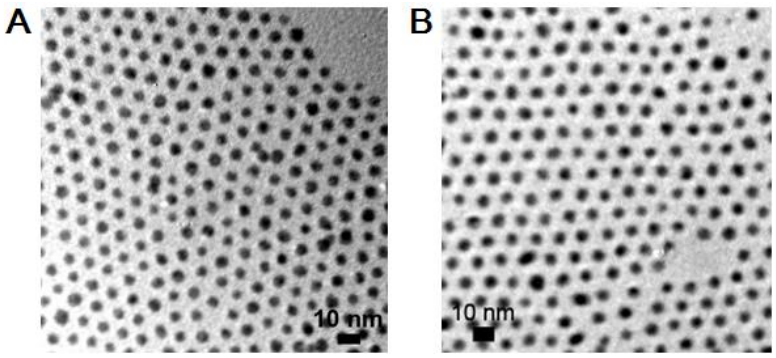

Figure 9.2.2 TEM images of (**A**) the 4 nm $Fe_{42}Pt_{44}Au_{14}$ and (**B**) the 4 nm $Fe_{34}Pt_{34}Au_{32}$ NPs.

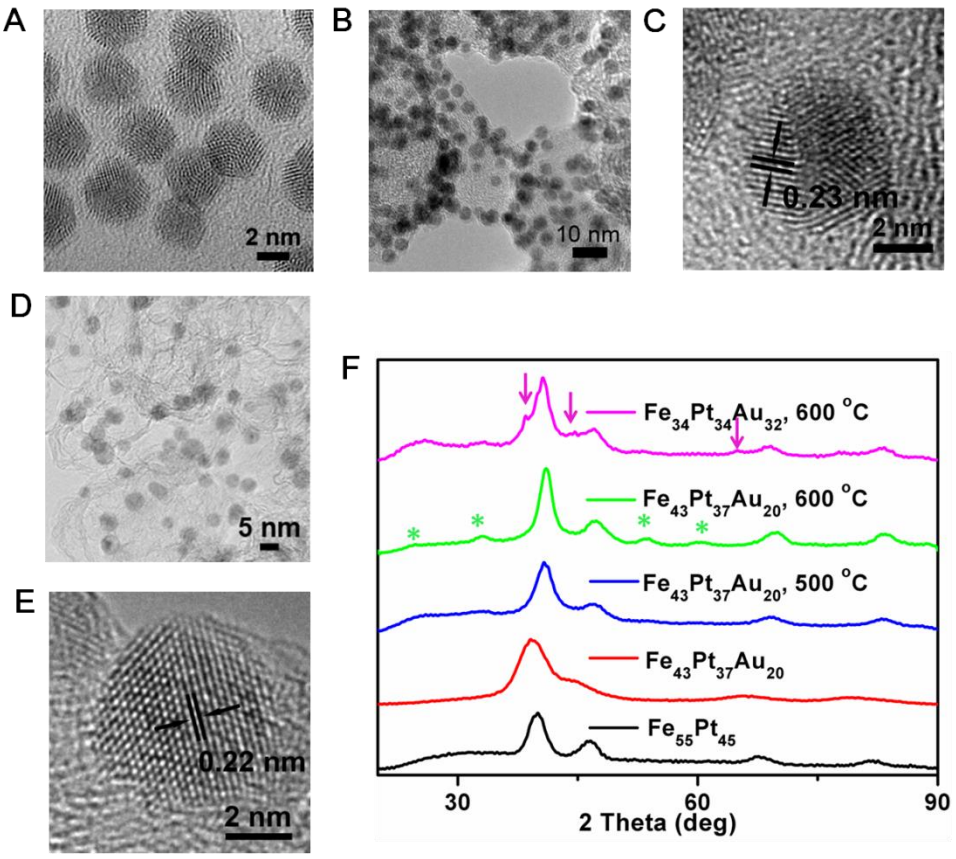

Figure 9.2.3 TEM images of (A) the as-synthesized 4 nm $Fe_{43}Pt_{37}Au_{20}$ NPs, (B) the *fcc*-$Fe_{43}Pt_{37}Au_{20}$/C NPs, (C) a representative *fcc*-$Fe_{43}Pt_{37}Au_{20}$/C NP, (D) the *fct*-$Fe_{43}Pt_{37}Au_{20}$/C NPs and (E) a representative *fct*-$Fe_{43}Pt_{37}Au_{20}$/C NP. The as-synthesized NPs were deposited on the amorphous carbon coated Cu grid and the other NPs were deposited on the Ketjen carbon support and annealed under 95% Ar + 5% H_2 at 400 °C (B, C) and 600 ºC (D, E) for 1 h. (F) XRD patterns of the as-synthesized $Fe_{55}Pt_{45}$ NPs, $Fe_{43}Pt_{37}Au_{20}$ NPs, and the $Fe_{43}Pt_{37}Au_{20}$ NPs annealed at 500 ºC, 600 ºC (stars denote the *fct*-FePt peaks) as well as the $Fe_{34}Pt_{34}Au_{32}$ NPs annealed at 600 ºC (arrows denote the Au peaks). The NPs were deposited on the

Ketjen carbon support and annealed under forming gas (95% Ar + 5% H_2) for 1 h.

FePt NPs are often synthesized by reduction of $Pt(acac)_2$ and thermal decomposition of $Fe(CO)_5$ in the presence of oleic acid and oleylamine as demonstrated in Chapter 6.[17] We found this same recipe does not work for the current synthesis of FePtAu NPs with the desired size and Fe/Pt/Au composition controls. Alternatively, when tetradecylphosphonic acid is used instead of oleic acid , co-reduction of $Pt(acac)_2$ and $HAuCl_4$ and decomposition of $Fe(CO)_5$ yields monodisperse 4 nm FePtAu NPs with Fe/Pt/Au compositions readily controlled by the metal precursor ratios. In this work, the Fe/Pt ratio is kept at near 1/1 to facilitate *fcc-fct* phase transformation,[17] while Au is made to have three different percentages so that Au composition-dependent *fcc-fct* transition and Au-dependent FAOR catalysis can be studied.

To remove the surfactants around NPs and to convert the *fcc*-FePtAu to *fct*-FePtAu, high temperature annealing was applied. To prevent NPs from aggregation under these annealing conditions and to facilitate the catalytic studies, the as-synthesized NPs were deposited on Ketjen carbon (C) support before the annealing (see Experimental). Figure 9.2.3B, C show the typical TEM (B) and HRTEM (C) images of the *fcc*-$Fe_{43}Pt_{37}Au_{20}$ NPs annealed under 95% Ar + 5% H_2 at 400 °C for 1 h. The *fcc*-$Fe_{43}Pt_{37}Au_{20}$ NPs have the average size of 4 ± 0.2 nm and (111) lattice fringe distance at 0.23 nm. Upon annealing at 600 °C for 1 h, the *fcc*-$Fe_{43}Pt_{37}Au_{20}$ NPs are

converted to *fct*-$Fe_{43}Pt_{37}Au_{20}$ NPs, as shown in the TEM image (Figure 9.2.3D) and high resolution TEM (HRTEM) image (Figure 9.2.3E) of the NPs. The NP morphology integrity observed in these TEM images indicate that the FePtAu NPs deposited on the carbon support are well-protected against aggregation/sintering during the high temperature annealing treatments.

X-rady diffraction patterns (XRD) were used to monitor the structure transition of the FePt and FePtAu NPs deposited on C (Figure 9.2.3F). The as-synthesized $Fe_{43}Pt_{37}Au_{20}$ NPs show a typical *fcc* pattern with broadened and small angle-shifted peaks compared to the 4 nm *fcc*-$Fe_{55}Pt_{45}$ NPs, suggesting that Au-doping in FePt induces the reduction of crystal coherence length and increase of crystal lattice spacing. When annealed at 400 ºC and 500 ºC for 1 h, the $Fe_{43}Pt_{37}Au_{20}$ NPs remain to be *fcc*, but at 600 ºC for 1 h, the *fcc*-$Fe_{43}Pt_{37}Au_{20}$ is converted to partially ordered *fct*-$Fe_{43}Pt_{37}Au_{20}$. Associated with this structure change, the 4 nm *fct*-$Fe_{43}Pt_{37}Au_{20}$ NPs become ferromagnetic and show a coercivity of ~1000 Oe at room temperature while the 4 nm $Fe_{55}Pt_{45}$ NPs annealed under the same condition have a coercivity of only ~300 Oe (Figure 9.2.4). We should note that since these NPs are not magnetically saturated, the coercivity values measured from the hysteresis loops are the low-end numbers and are used only to demonstrate the FePt structure conversion. The coervivity values should be larger than the reported once these NPs are magnetically saturated under a stronger magnetic field. These indicate that Au segregation from the FePtAu structure helps to create lattice vacancies within the 4 nm FePtAu structure,

promoting Fe, Pt rearrangement. This supports what has been proposed in Au doping effect on FePt structure transformation.[21] We should note that to achieve a complete fcc-fct transition within 4 nm FePtAu NPs is difficult as the small NP size tends to restrict the Fe and Pt mobility unless even higher annealing temperate and longer annealing time are applied, which can cause carbon support degradation and FePtAu NP aggregation/sintering. Our studies further show that the *fct*-structure formation within FePtAu is Au composition-dependent with Au in 20% (by atomic percentage) range forming better chemical order within the FePt structure. Adding more Au to the FePtAu structure seems to have no benefit for *fcc-fct* transition as the $Fe_{34}Pt_{34}Au_{32}$ NPs annealed at 600 ºC exhibit weaker/broader *fct* peaks than the $Fe_{43}Pt_{37}Au_{20}$ NPs (Figure 9.2.3F).

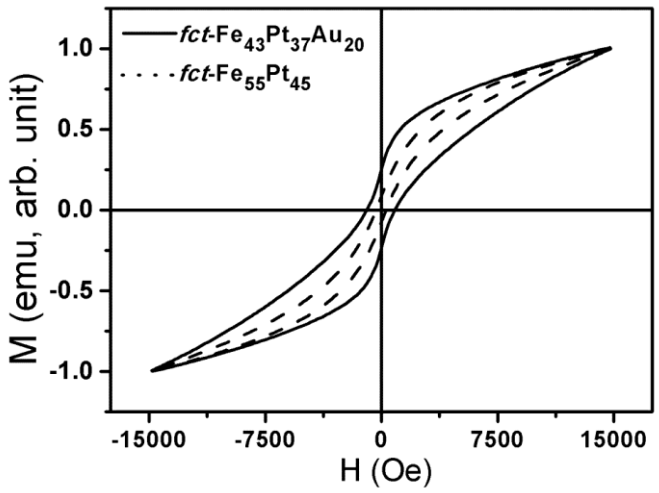

Figure 9.2.4 Room temperature hysteresis loops of the 4 nm *fct*-$Fe_{55}Pt_{45}$ NPs (dot curve) and *fct*-$Fe_{43}Pt_{37}Au_{20}$ NPs (solid curve).

The carbon-supported $Fe_{43}Pt_{37}Au_{20}$ NPs annealed at 400 °C and 600 °C respectively were further characterized by atomically resolved aberration-corrected scanning transmission electron microscopy (STEM), STEM-electron energy-loss spectroscopy (STEM-EELS) and STEM-energy dispersive X-ray spectroscopy (STEM-EDS). Figure 9.2.5A is the high-angle annular dark field (HAADF) image of a representative *fcc*-$Fe_{43}Pt_{37}Au_{20}$ NP and Figure 9.2.5B-D are the corresponding Fe elemental mapping of this NP using STEM-EELS method. These analyses indicate that Fe in the *fcc*-structure is uniformly distributed. In contrast, HAADF image and the corresponding Fe elemental mapping of the *fct*-$Fe_{43}Pt_{37}Au_{20}$ NP (Figure 9.2.5E-H) show that Fe is concentrated in the core region and Au/Pt are rich in the shell structure. The STEM-EDS line scans confirm that Au alloys uniformly with Fe and Pt in the *fcc*-$Fe_{43}Pt_{37}Au_{20}$ NPs (Figure 9.2.6) but in the *fct*-$Fe_{43}Pt_{37}Au_{20}$ structure, it diffuses out and concentrates around the shell (Figure 9.2.7). Based on the STEM-EELS and STEM-EDS analyses, the annealing-induced structure change of FePtAu can be illustrated in Figure 9.1.2. When annealed at 400 °C, the *fcc* structure is better formed in FePtAu NPs. At 600 °C, the *fcc*-FePtAu is converted to *fct*-FePtAu with Au-segregating on the FePt NP surface.[22] Such a unique structure pattern is essential for *fct*-FePtAu NPs to show the enhanced activity and durability for FAOR.

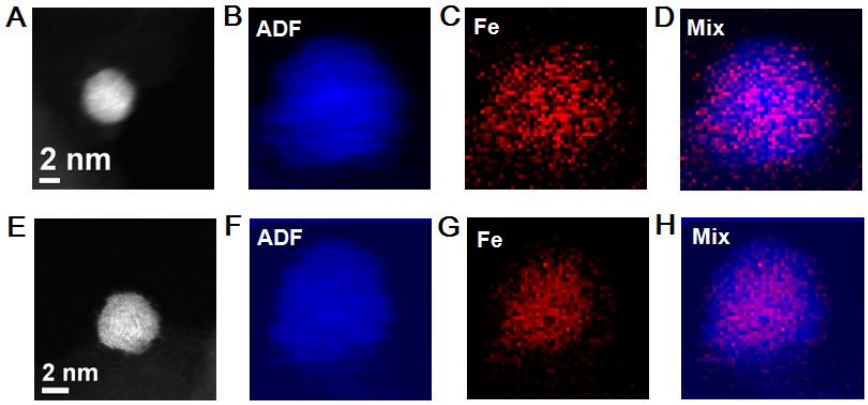

Figure 9.2.5 (A) STEM imaging and (B)-(D) simultaneous 2D STEM-EELS mapping from a representative *fcc*-$Fe_{43}Pt_{37}Au_{20}$ NP. (E) STEM imaging and (F)-(H) simultaneous 2D STEM-EELS mapping from a representative *fct*-$Fe_{43}Pt_{37}Au_{20}$ NP.

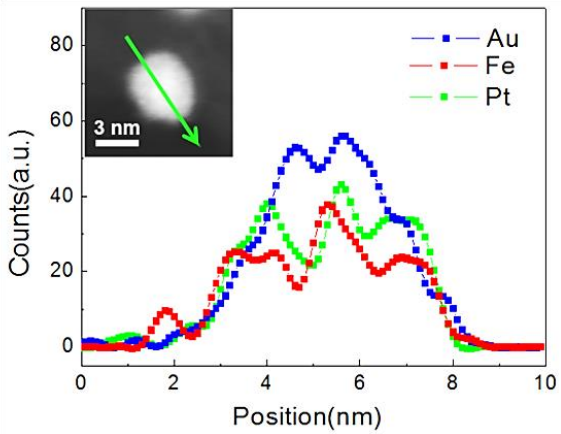

Figure 9.2.6 STEM-EDS line scans crossing *fcc*-$Fe_{43}Pt_{37}Au_{20}$.

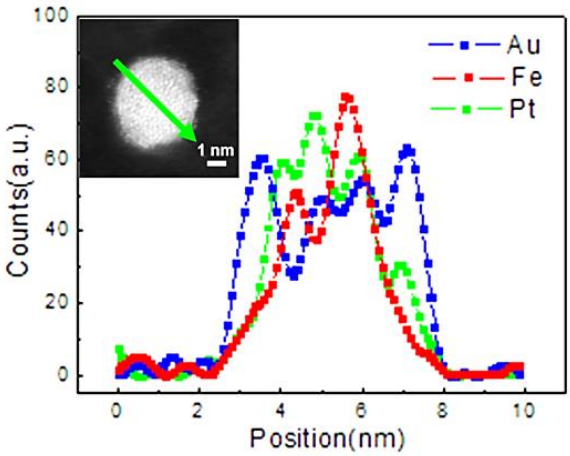

Figure 9.2.7 STEM-EDS line scans crossing *fct*-$Fe_{43}Pt_{37}Au_{20}$.

9.3.2 FePtAu NPs for FAOR

The Au composition effect of the 4 nm *fct*-FePtAu NPs on FAOR was first studied to obtain the optimum Au composition for further catalytic studies. Figure 9.2.8A and Figure 9.2.9A show the cyclic voltammograms (CVs) of three different kinds of *fct*-FePtAu NPs in the N_2-saturated 0.5 M H_2SO_4 solution. The peaks appearing in the range of -0.25 to 0.15 V are attributed to hydrogen underpotential formation/stripping (H_{UPD}) and are used to estimate the electrochemical active surface area of the NPs (Figure 9.2.9A).[23] The peaks in 0.3-0.9 V are from metal oxidation/reduction - more Au content in the NP structure leads to stronger Au reduction peaks at 0.80 V (Figure 9.2.8A). The electro-oxidation activity of these *fct*-FePtAu NPs in 0.5 M H_2SO_4 and 0.5 M HCOOH is normalized against NP surface area and is plotted as curves of the current density (*j*) *vs.* the applied potentials (*V*) (Figure 9.2.8B). For the *fct*-$Fe_{42}Pt_{44}Au_{14}$ NPs, the first current maximum at 0.47 V in the forward scan is due

to the direct oxidation of HCOOH to CO_2 (dehydrogenation reaction), while the second current maximum at 0.71 V corresponds to oxidation of CO generated from the dehydration reaction of HCOOH.[11] The stability of these *fct*-FePtAu NPs was tested by chronoamperometry (CA) as shown in the *j* change of FAOR over time (*t*) at 0.2 V (Figure 9.2.9B).[24] Among three different kinds of *fct*-FePAu NPs studied, the *fct*-$Fe_{43}Pt_{37}Au_{20}$ NPs have the best long-term stability.

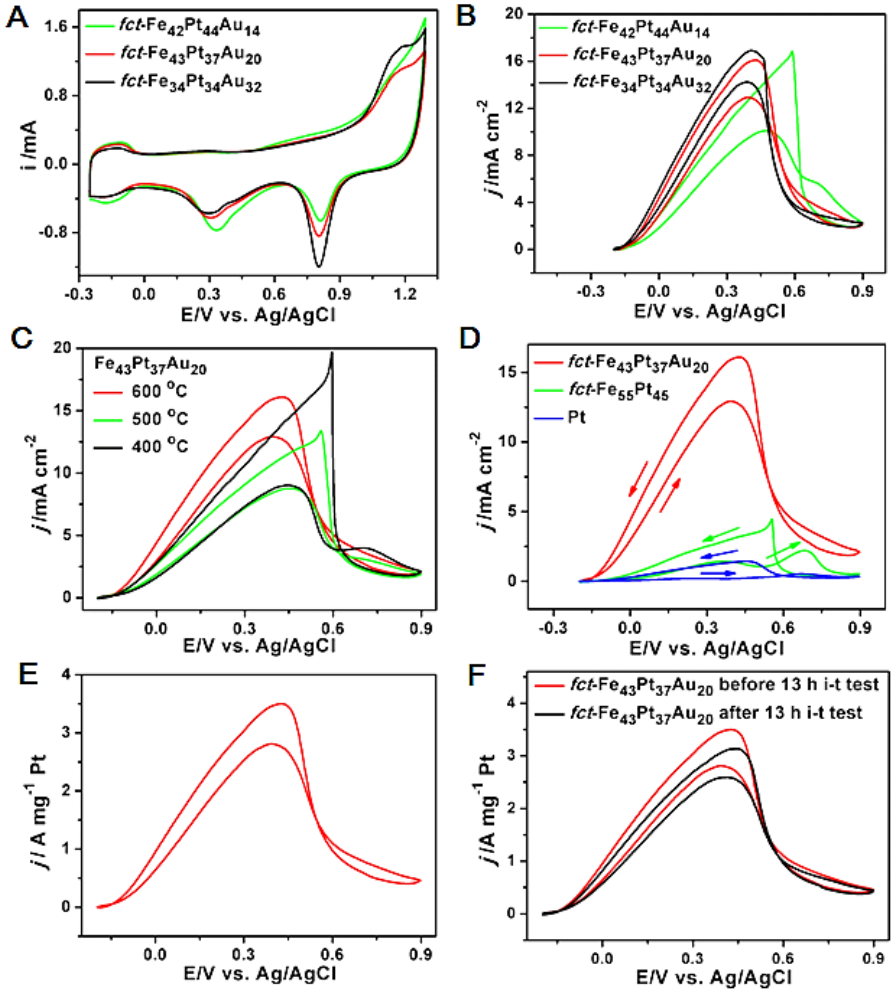

Figure 9.2.8 (**A**) CVs and (**B**) *j*-*V* curves of the *fct*-FePtAu NPs with different

compositions; (**C**) *j*-*V* curves of the $Fe_{43}Pt_{37}Au_{20}$ NPs annealed at different temperatures; (**D**) *j*-*V* curves of the specific activity of the *fct*-$Fe_{43}Pt_{37}Au_{20}$, *fct*-$Fe_{55}Pt_{45}$ and commercial Pt catalysts; (**E**) *j*-*V* curves of the mass activity of the *fct*-$Fe_{43}Pt_{37}Au_{20}$ NPs; and (**F**) *j*-*V* curves of the *fct*-$Fe_{43}Pt_{37}Au_{20}$ NPs before and after 13 h *i*-*t* stability test. The studies were performed in the N_2-saturated 0.5 M H_2SO_4 (for CV curves) and 0.5 M H_2SO_4 + 0.5 M HCOOH solutions (for *j*-*V* curves).

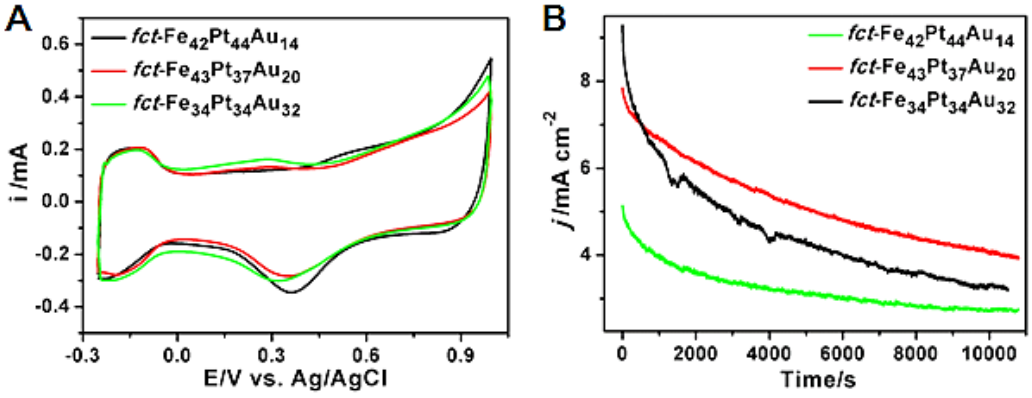

Figure 9.2.9 (A) CVs of the *fct*-FePtAu NPs with different compositions in the N_2-saturated 0.5 M H_2SO_4 solution and (B) the *j*-*t* curves of the *fct*-FePtAu NPs reflecting the specific activity change over time.

The structure effect of the $Fe_{43}Pt_{37}Au_{20}$ NPs on FAOR catalysis was investigated. Figure 9.2.10 shows the CVs of the $Fe_{43}Pt_{37}Au_{20}$ NPs annealed at different temperatures. With the increase in annealing temperatures from 400 to 600 ºC, the

Pt-based reduction peak potentials shift negatively, indicating the better Fe-alloy effect to Pt in *fct*-FePt than in *fcc*-FePt structure. The FAOR catalyzed by the $Fe_{43}Pt_{37}Au_{20}$ NPs annealed at different temperatures are shown in Figure 9.2.8C. The *fcc*-$Fe_{43}Pt_{37}Au_{20}$ NPs obtained from 400 ºC annealing display an obvious CO-oxidation peak at 0.7 V. Increasing the annealing temperature to 500 ºC results in the intensity drop of this oxidation peak. The NPs annealed at 600 ºC for 1 h show no CO-oxidation peak, suggesting that the segregation of Au on the surface of the *fct*-$Fe_{43}Pt_{37}Au_{20}$ NPs helps CO removal. The FAOR stability of the $Fe_{43}Pt_{37}Au_{20}$ NPs annealed at different temperatures are shown in Figure 9.2.11. The $Fe_{43}Pt_{37}Au_{20}$ NPs annealed at 600 ºC are more stable for FAOR than any of the other two kinds of NPs treated at 400 and 500 ºC, indicating once again that the *fct* structure favors the durability enhancement of FePtAu NPs for FAOR.

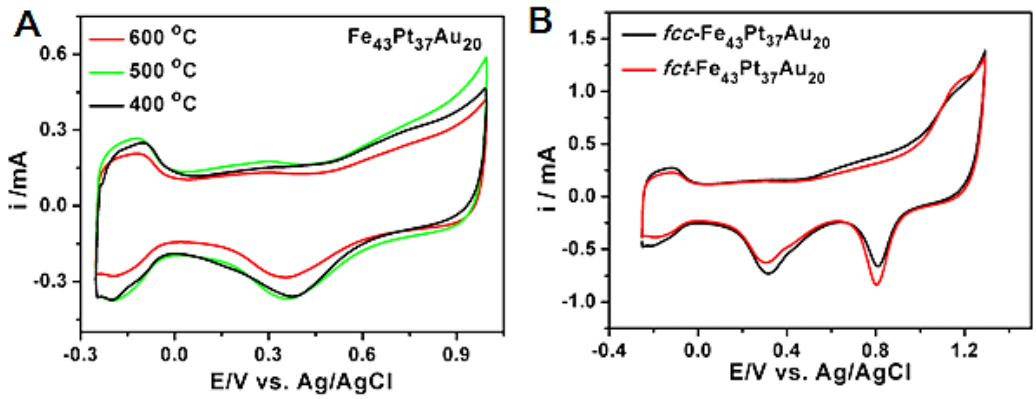

Figure 9.2.10 CVs of the $Fe_{43}Pt_{37}Au_{20}$ NPs annealed at different temperatures with the potentials scanned from -0.25 to 1.0 V (A) and -0.25 to 1.30 V (B) in the N_2-saturated 0.5 M H_2SO_4 solution.

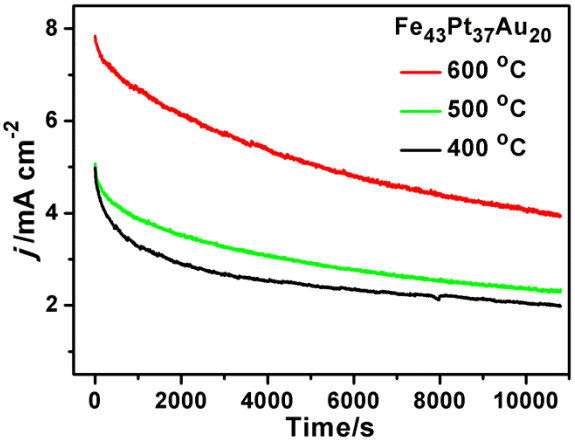

Figure 9.2.11 The *j-t* curves of the $Fe_{43}Pt_{37}Au_{20}$ NPs annealed at different temperatures.

The *fct*-$Fe_{43}Pt_{37}Au_{20}$ NPs are much more active and durable catalyst for FAOR than the *fct*-$Fe_{55}Pt_{45}$ NPs and the commercial Pt NPs. Figure 9.2.12 and Figure 9.2.8D show the comparison of CVs and *j-V* curves respectively for these NPs. As expected, the Pt catalyst has a very strong CO-oxidation peak at 0.67 V whereas the *fct*-$Fe_{55}Pt_{45}$ shows a relatively weak peak at 0.69 V, and the *fct*-$Fe_{43}Pt_{37}Au_{20}$ NPs have no CO-oxidation peak. Without the CO-poisoning effect, the *fct*-$Fe_{43}Pt_{37}Au_{20}$ NPs have an onset FAOR potential at -0.2 V, which is 0.12 V lower than that of the commercial Pt (-0.08 V). The mass activity of the 4 nm *fct*-$Fe_{43}Pt_{37}Au_{20}$ NPs reaches 2809.9 mA/mg Pt (Figure 9.2.8E), which is the highest among all NP catalysts ever reported. Furthermore, the *fct*-$Fe_{43}Pt_{37}Au_{20}$ NPs are also the most stable NP catalysts for FOAR – their specific activity, drops about 50% at the end of 3 h *j-t* test (Figure 9.2.13).

Even after 13 h *j-t* test, their mass activity is still at 2600 mA/mg Pt (92.5% of the original value of 2809.9 mA/mg Pt) (Figure 9.2.8E). As a comparison, under the same measurement conditions, the state-of-art PtBi NPs have the mass activity of about 1720 mA/mg Pt and can keep only about 11% of their initial activity at the end of 3 h *j-t* test.[11]

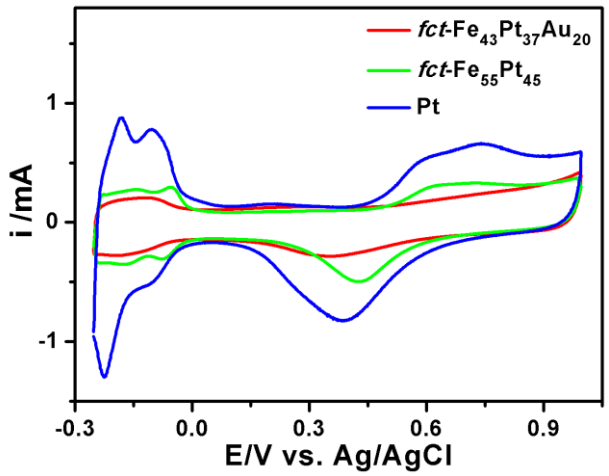

Figure 9.2.12 CVs of the *fct*-$Fe_{43}Pt_{37}Au_{20}$, *fct*-$Fe_{55}Pt_{45}$, and commercial Pt NPs in the N_2-saturated 0.5 M H_2SO_4 solution.

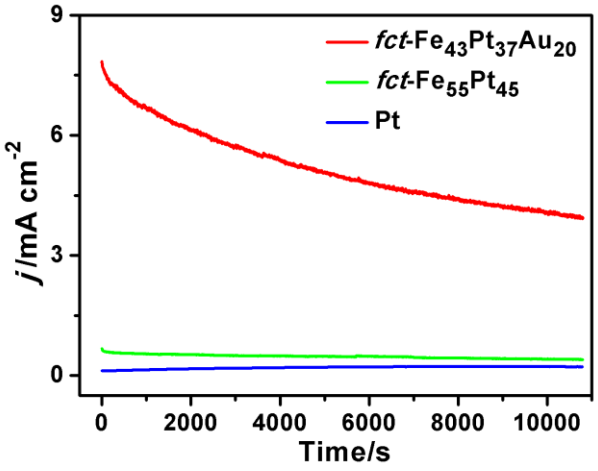

Figure 9.2.13 The *j-t* curves of the *fct*-$Fe_{43}Pt_{37}Au_{20}$, *fct*-$Fe_{55}Pt_{45}$, and commercial Pt catalysts.

The *fct*-FePtAu structure with Au segregating on the FePt surface is essential for the NPs to show the enhanced activity and durability for FAOR. With the increase of the Au amount to 20% and 32% in the *fct*-$Fe_{43}Pt_{37}Au_{20}$ and *fct*-$Fe_{34}Pt_{34}Au_{32}$ NPs, the CO-related peak in FAOR disappears, indicating that Au on the NP surface promotes the dehydrogenation reaction of HCOOH and inhibits the dehydration reaction that leads to the formation of CO. It seems that Au helps to boost the formation of $HCOO_{ads}$ and its spillover to Pt to facilitate dehydrogenation pathway.[25] The enhanced stability comes likely from the formation of *fct* structure within *fct*-FePtAu NPs promoted by Au doping and segregation. Without the presence of Au and the formation of *fct*-structure, NPs such as Pt, FePt or *fcc*-FePtAu NPs, are all subject to easy CO poisoning and acid dissolution, exhibiting much lower activity and stability for FAOR than the *fct*-FePtAu NPs.

9.4 Conclusion

In summary, this Chapter presents a new structure-control strategy to tune and optimize FePtAu NP catalysis for FAOR. These NPs are synthesized by a facile solution-phase process with their compositions controlled by the molar ratios of the metal precursors. The presence of Au in FePt facilitates the FePt structure

transformation from *fcc* to *fct* and further promotes the FAOR in the H_2SO_4 solution. Among all Pt, FePt and FePtAu NPs tested, the 4 nm *fct*-$Fe_{43}Pt_{37}Au_{20}$ NPs are the most active and durable catalyst - they have the mass activity of 2809.9 mA/mg Pt and retain 92.5% of this activity after 13 h stability test. The high CO-resistant activity of the *fct*-$Fe_{43}Pt_{37}Au_{20}$ NPs is attributed to surface segregation of Au from the *fct*-FePt, while the high durability is the result of the formation of the *fct* structure promoted by Au-segregation within the FePtAu NPs. Our preliminary tests show that the *fct*-$Fe_{43}Pt_{37}Au_{20}$ NPs are also active for catalyzing methanol oxidation reaction with a high CO-tolerance activity (Figure 9.3). The work demonstrates the great potentials of *fct*-FePtAu NPs as highly efficient catalysts for electro-oxidation reactions of organic molecules. More importantly, the structure-control strategy is not limited to FePtAu NPs, but can be extended to other M-doped FePtM (M = Cu, Ag, Sb for example),[18] or Pt- and Pd-based multi-metallic NPs, providing a general approach to advanced NP catalysts with simultaneous enhancement in both activity and durability for practical applications.

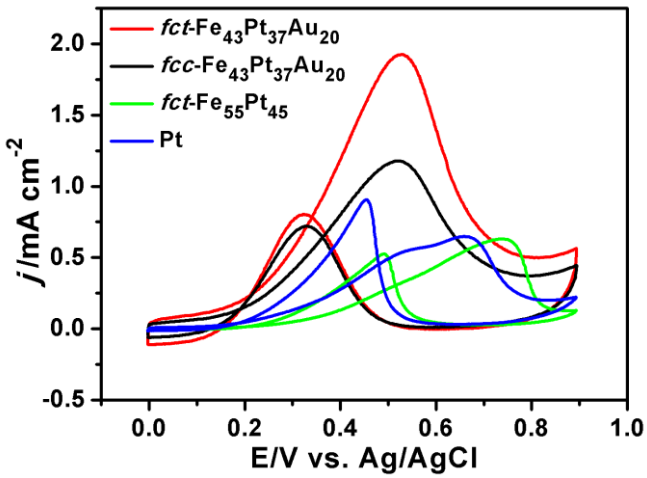

Figure 9.3 CVs of the *fct*-$Fe_{43}Pt_{37}Au_{20}$, *fcc*-$Fe_{43}Pt_{37}Au_{20}$, *fct*-$Fe_{55}Pt_{45}$ and commercial Pt NPs in the N_2-saturated 0.5 M H_2SO_4 and 0.5 M methanol solution. In the methanol oxidation reaction, two oxidation peaks are usually observed. The stronger peak in the forward scan is related to the direct methanol oxidation. The smaller peak in the backward scan is likely associated the oxidation of the carbonaceous species formed on the catalyst surface in the forward scan. The ratio of the forward peak current (I_f) to the backward peak current (I_b), I_f/I_b, is often used as an index to measure the catalyst tolerance to the poisoning species (like CO). A higher ratio indicates more effective removal of the poisoning species on the catalyst surface. The CV from the *fct*-$Fe_{43}Pt_{37}Au_{20}$ NPs has an I_f/I_b value of 2.8, while for the *fcc*-$Fe_{43}Pt_{37}Au_{20}$, *fct*-$Fe_{55}Pt_{45}$ and commercial Pt NP catalysts, the values drop to 1.62, 1.20, and 0.71 respectively.

References

1. N. Tian, Z.-Y. Zhou, S.-G. Sun, Y. Ding, Z. L. Wang, *Science* **2007**, *316*, 732-735.
2. B. Lim, M. Jiang, P. H. C. Camargo, E. C. Cho, J. Tao, X. Lu, Y. Zhu, Y. Xia, *Science* **2009**, *324*, 1302-1305.
3. K. Gong, D.Su, R. R. Adzic, *J. Am. Chem. Soc.* **2010**, *132*, 14364-14366.
4. C. Wang, H. Daimon, T. Onodera, T. Koda, S. Sun, *Angew. Chem. Int. Ed.* **2008**, *47*, 3588-3591.
5. Y. Kang, C. B. Murray, *J. Am. Chem. Soc.* **2010**, *132*, 7568-7569.
6. Y.-C. Lu, Z. Xu, H. A. Gasteiger, S. Chen, K. Hamad-Schifferli, S.-H. Yang, *J. Am. Chem. Soc.* **2010**, *132*, 12170-12171.
7. A.-X. Yin, X.-Q. Min, Y.-W. Zhang, C.-H. Yan, *J. Am. Chem. Soc.* **2011**, *133*, 3816-3819.
8. H. Zhang, M. Jin, J. Wang, W. Li, P. H. C. Camargo, M. J. Kim, D. Yang, Z. Xie, Y. Xia, *J. Am. Chem. Soc.* **2011**, *133*, 6078-6089.
9. J. Zhang, H. Yang, J. Fang, S. Zou, *Nano Lett.* **2010**, *10*, 638-644.
10. J. Wu, A. Gross, H. Yang, *Nano Lett.* **2011**, *11*, 798-802.
11. X. Ji, K. T. Lee, R. Holden, L. Zhang, J. Zhang, G. A. Botton, M. Couillard, L. F. Nazar, *Nature Chem.* **2010**, *2*, 286-293.
12. Y. Bing, H. Liu, L. Zhang, D. Ghosh, J. Zhang, *Chem. Soc. Rev.* **2010**, *39*, 2184-2202.

13. A. Cheng, P. Holt-Hindle, *Chem. Rev.* **2010**, *110*, 3767-3804.

14. V. Mazumder, M. Chi, K. L. More, S. Sun, *J. Am. Chem. Soc.* **2010**, *132*, 7848-7849.

15. K. Sasaki, H. Naohara, Y. Cai, Y. M. Choi, P. Liu, M. B. Vukmirovic, J. X. Wang, R. R. Adzic, *Angew. Chem. Int. Ed.* **2010**, *49*, 8602-8607.

16. C. Wang, D. V. D. Vliet, K. L. More, N. J. Zaluzec, S. Peng, S. Sun, H. Daimon, G. Wang, J. Greeley, J. Pearson, A. P. Paulikas, G. Karapetrov, D. Strmcnik, N. M. Markovic, V. R. Stamenkovic, *Nano Lett.* 2011, *11*, 919-926.

17. S. H. Sun, C. B. Murray, D. Weller, L. Folks, A. Moser, *Science* **2000**, *287*, 1989-1992.

18. S. H. Sun, *Adv. Mater.* **2006**, *18*, 393-403.

19. J. Kim, Y. Lee, S. Sun, *J. Am. Chem. Soc* **2010**, *132*, 4996-4997.

20. X. Yu, P. G. Pickup, *J. Power Sources* **2008**, *182*, 124-132.

21. S. Kinge, T. Gang, W. J. M. Naber, H. Boschker, G. Rijnders, D. N. Reinhoudt, W. G. van der Wiel, *Nano Lett.* **2009**, *9*, 3220-3224.

22. S. Kang, A. Jia, D. E. Nikles, J. W. Harrell, *IEEE Trans. Magn.* **2003**, *39*, 2753-2757.

23. J. Snyder, T. Fujita, M.W. Chen, J. Erlebacher, *Nat. Mater.* **2010**, *9*, 904-907.

24. S. Guo, S. Zhang, X. Sun, S. Sun, *J. Am. Chem. Soc.* **2011**, *39*, 15354-15357.

25. S. Zhang, Y. Shao, G. Yin, Y. Lin, *Angew. Chem. Int. Ed.* **2010**, *49*, 2211-2214.